Doctoral thesis

NMR studies of insulating phase adjacent to superconducting phase in quasi-two-dimensional organic conductors (擬二次元有機伝導体の超伝導隣接絶縁相のNMRによる研究)

Yohei Saito
Department of Condensed Matter Physics
Graduate School of Science, Hokkaido University

March 2018

Contents

Chapter 1

Introduction

1.1 Character of organic conductors

Organic conductors are organic materials which show good conductivity[1]. A lot of organic materials are insulators because of a large energy gap between HOMO (highest occupied molecular orbitals) and LUMO (lowest unoccupied molecular orbitals). This property was first overcome by combining planar organic molecules with non-organic anions which serve as acceptors or donors filling partly conduction or valence bands. Such materials are called charge transfer salts. The most famous charge transfer salt is TTF-TCNQ which is formed by the combination of tetrathiafulvalene (TTF) as a donor and tetracyanoquinodimethane (TCNQ) as an acceptor molecule in Fig.1.1. TTF-TCNQ shows metallic electrical conductance through the overlap of the π-orbital due to the charge transfer of δ from TTF to TCNQ. In the research of the charge transfer salts of tetramethyltetraselenafulvalence (TMTSF) with an inorganic anion shown in Fig.1.1, $(TMTSF)_2PF_6$ shows superconductivity with a transition temperature of $T_c = 1.1$ K under a pressure of 6.5 kbar[2].

Organic conductors show variety of electronic phases such as the charge density wave (CDW), spin density wave (SDW), antiferromagnetic (AF), and superconducting (SC) phases. The origin of the variation is the mutual interplay among the low dimensionality, the electron correlations, the electron-phonon interaction, the transfer integral, and the topology of the Fermi surface. Because on-site Coulomb energy U competes against bandwidth W in the organic conductors, the organic conductors are regarded as

a strongly correlated electron system and the physical properties can be controlled by applying the physical pressure or, the substitution of counter inorganic anions. In addition, due to the π-orbital which is perpendicular to the molecular plane, the orbital overlap between molecules is highly anisotropic shown in Fig.1.2.

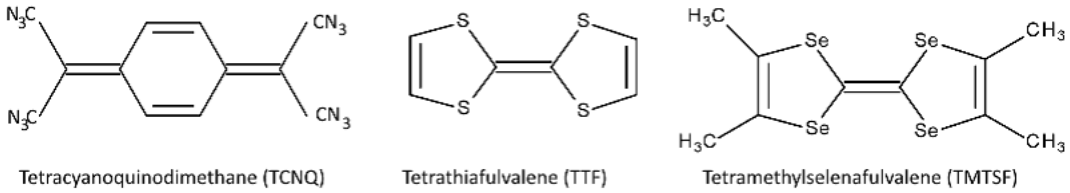

Figure 1.1: Molecular structure of TCNQ, TTF, and TMTSF.

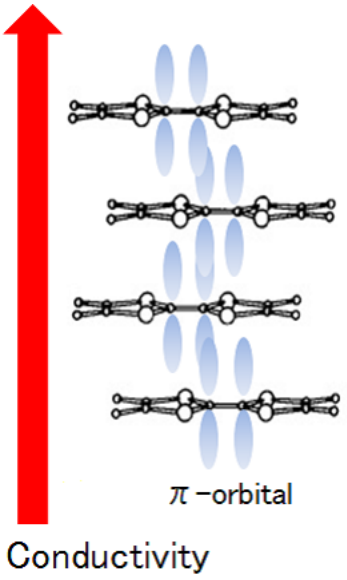

Figure 1.2: Conductivity in an organic conductor.

1.2 Organic conductor κ-$(ET)_2X$ and $Cu_2(CN)_3$ salt

Organic conductors based on ET (ET: bis(ethylenedithio)tetrathiafulvalene) molecules which are electron donors shown in Fig.3.1(a) have layered structures consisting of conducting ET sheets and insulating anion sheets in Fig.3.1(c). Therefore, κ-$(ET)_2X$ is a quasi-two-dimensional system. The organic conductors show various physical properties which depend on the packing in the donor sheet shown in Fig.1.4. In κ-$(ET)_2X$, two ET molecules form a dimer in the conduction layer. Table1.1 shows the crystallographic data of the typical κ-$(ET)_2X$ salts. Since X^- is a monovalent anion, the formal charge of ET is +0.5. Although that case is regarded as a quarter-filled system, the electronic system in κ-$(ET)_2X$ is believe to be half-filled due to the dimerization of ET molecules as shown in Fig.1.5 where there is a carrier per a ET dimer. In this picture, the effective value of the Coulomb repulsion on a dimer is given by

$$
\begin{aligned}
U_{eff} &= \frac{U_{\mathrm{ET}}}{2}\left\{1-\sqrt{1+\left(\frac{4t_{\mathrm{dimer}}}{U_{\mathrm{ET}}}\right)^2}\right\}+2t_{\mathrm{dimer}} && (1.1)\\
&\approx \frac{U_{\mathrm{ET}}}{2}\left\{1-\left(1+\frac{1}{2}\left(\frac{4t_{\mathrm{dimer}}}{U_{\mathrm{ET}}}\right)^2\right)\right\}+2t_{\mathrm{dimer}} && (1.2)\\
&= 2t_{\mathrm{dimer}}-\frac{4t_{\mathrm{dimer}}^2}{U_{\mathrm{ET}}}, && (1.3)
\end{aligned}
$$

where U_{ET} is the on-site Coulomb repulsion of a ET molecule and t_{dimer} is a intradimer transfer integral. In the limit of $U_{ET} \gg t_{\mathrm{dimer}}$, the formula is approximated as $U_{eff} \approx 2t_{\mathrm{dimer}}$. As U_{eff} is comparable to the band width W and these values depend on the intermolecular configuration, we can control the physical property by the variety of anion X^- or by applying pressure as shown in Fig.1.6[4]. Thus, κ-$(ET)_2X$ is regarded as one of the highly correlated systems like the high-T_c cuprates..

The detailed investigations for κ-$(ET)_2X$ were performed mainly on X=Cu[N(CN)$_2$]Cl, Cu[N(CN)$_2$]Br, Cu(NCS)$_2$, and $Cu_2(CN)_3$ salts (hereafter abbreviated as Cl, Br, NCS, and $(CN)_3$, respectively). The Br and NCS salts show superconductivity at low temperature, whereas the Cl salt

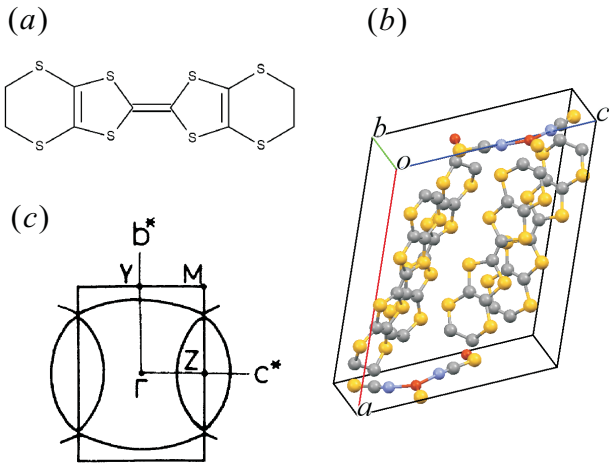

Figure 1.3: (a) Molecular structure of ET. (b) Crystal structure of NCS salt. (c) Fermi surface of NCS salt.[3]

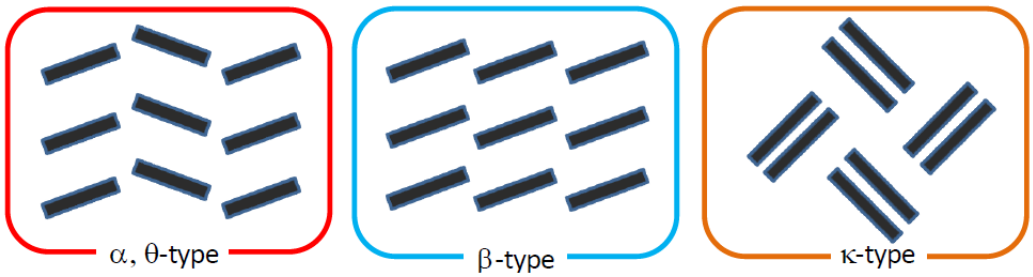

Figure 1.4: Arrangements of ET molecule in conducting sheet.

Table 1.1: Crystallographic data of κ-$(ET)_2X$.

X	$Cu(NCS)_2$	$Cu[N(CN)_2]Br$	$Cu[N(CN)_2]Cl$	$Cu_2(CN)_3$
Space group	$P2_1$	P_{nma}	P_{nma}	$P2_1/c$
a (Å)	16.248(5)	12.942(2)	12.977(3)	16.117(5)
b (Å)	8.440(2)	30.016(4)	29.979(4)	8.5858(9)
c (Å)	13.124(5)	8.539(3)	8.480(2)	13.397(3)
β (°)	110.30(3)	90	90	113.42(2)
V (Å^3)	1668.0(9)	3299(1)	3317(7)	1701.11

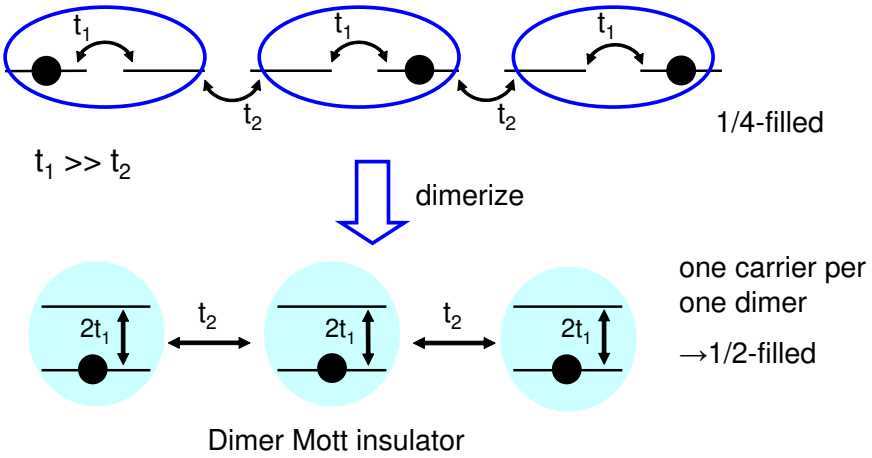

Figure 1.5: Dimer-Mott insulating picture.

shows an antiferromagnetism at ambient pressure and superconductivity under pressure as shown in Fig.1.7[5]. Moreover, it has been suggested that the κ-NCS salt show Fulde-Ferrell-Larkin-Ovchinnikov (FFLO) superconductivity, in which the order of superconductivity oscillates spatially [6]. The $(CN)_3$ salt also shows superconductivity under pressure as shown in Fig.1.8 whereas the semi-conductive behavior was observed under ambient pressures[7].

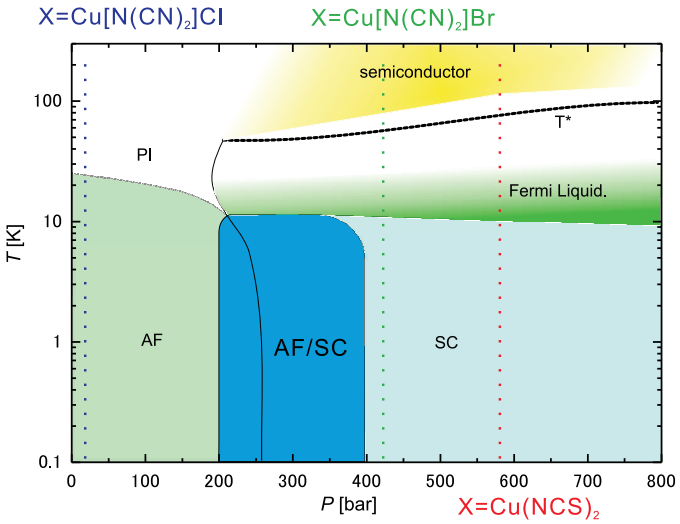

Figure 1.6: P-T phase diagram of κ-$(\mathrm{ET})_2X$.[4]

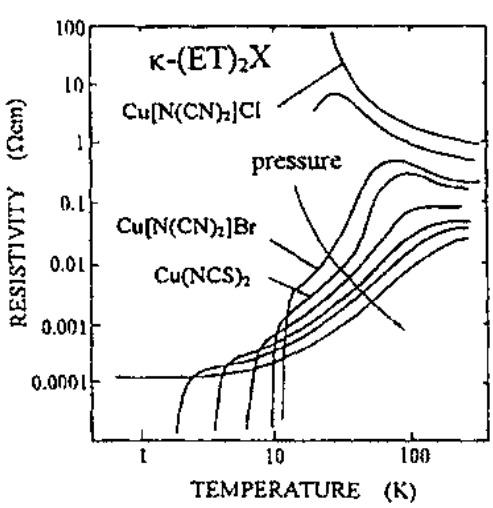

Figure 1.7: Temperature dependence of resistivity of κ-$(\mathrm{ET})_2X$ (X=Cu[N(CN)$_2$]Cl, Cu[N(CN)$_2$]Br, Cu(NCS)$_2$).[5]

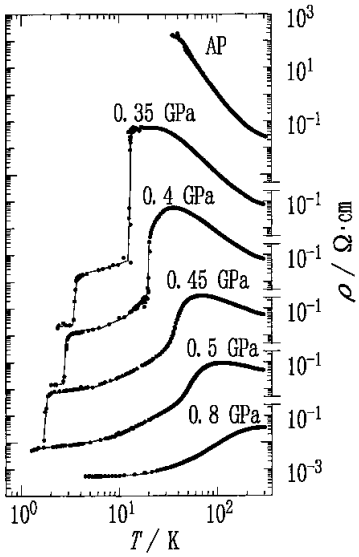

Figure 1.8: Temperature dependence of resistivity of κ-$(\mathrm{ET})_2\mathrm{Cu}_2(\mathrm{CN})_3$ at various pressures.[7]

1.3 Pressure dependence of Korringa factor and the effective cyclotron mass

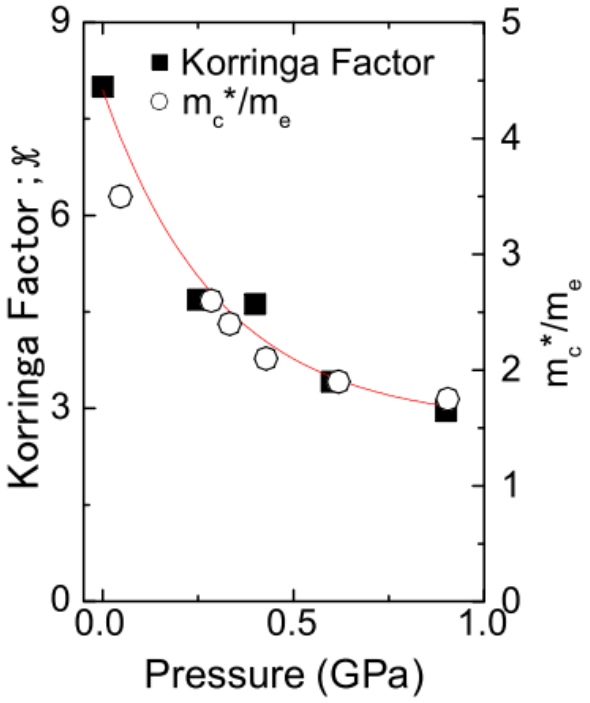

Figure 1.9: Pressure dependence of Korringa factor [8] and the effective cyclotron mass [9]

Figure 1.9 shows pressure dependence of Korringa factor and the effective cyclotron mass. The pressure dependence of cyclotron mass m_c^* and superconducting transition point T_c suggested a correlation between m_c^* and T_c [9] as shown in Fig.5.3. Antiferromagnetic electron correlation may therefore play an important role in the superconductivity of κ-salts. The Korringa factor $\mathcal{K}(\alpha)$ describing electron correlations is satisfied:

$$T_1 T K_s^2 = F\mathcal{K}(\alpha)^{-1} \frac{\hbar}{4\pi k_B} \left(\frac{\gamma_e}{\gamma_n}\right)^2$$

where F is a form factor due to the anisotropic hyperfine coupling constant (see the analytical expressions of ^{13}C NMR for κ-$(ET)_2X$ [10]), and γ_e

and γ_n are gyromagnetic ratios of electrons and ^{13}C nuclei, respectively. If $\mathcal{K}(\alpha) = 1$, the system is regarded as a simple metal. $\mathcal{K}(\alpha) < 1$ is regarded as indicative of ferromagnetic correlations, whereas $\mathcal{K}(\alpha) > 1$ is indicative of anti-ferromagnetic correlations. The pressure dependence of the Korringa factor in κ-NCS [8] is shown in Fig.5.3. Increasing pressure from ambient pressure to 0.25 GPa reduces the Korringa factor by 50 %, whereas additional pressure cause a further slow decrease. This behavior is similar to the pressure dependence of m_c^*. The behavior of $\mathcal{K}(\alpha) > 1$ suggests additional antiferromagnetic contributions.

1.4 Geometrical frustration of spin

The ground state of the $(CN)_3$ salt is expected to be AF because U/W of the $(CN)_3$ salt is larger than of the Cl salt as shown in Table.1.2[7]. Figure.1.10 shows the temperature dependence of magnetic susceptibility of the $(CN)_3$ and Cl salts[11]. Contrary to the expectation, the $(CN)_3$ salt exhibits no magnetic ordering. Figure.1.11 shows temperature dependence of ^{1}H NMR spectra of the $(CN)_3$ and Cl salts[11]. The solid and dotted lines in Fig.1.10 represent the fitting results of the series expansion of $S = 1/2$ triangular lattice Heisenberg model using [6/6] and [7/7] Padé approximants with $J = 250$ K where $[m/n]$ represented degrees of the approximants, respectively. The Cl salt exhibits AF ordering at 27 K with the spectrum splitting due to the commensurate internal field, whereas the $(CN)_3$ salt exhibits no AF ordering down to 32 mK. One of the possibilities for no AF ordering in $(CN)_3$ salt is explained by the contribution of the geometrical frustration of spins. Figure1.12 shows the view of ET dimers in the conduction plane and the interdimer transfer integrals are labeled by t and t'. In the $(CN)_3$ salt, the ratio of the transfer integrals $t'/t = 1.06$ was calculated from the extended Hückel approximation[12]. As the exchange interaction, J, is expressed by $-2t^2/U$, the ratio of J is also close to unity, suggesting a $S = 1/2$ nearly isotropic triangular lattice. When the first two spins align anti-parallel as shown in Fig.1.13, the third one is frustrated since its two possible orientations, up and down, give the same energy. In this case, AF ordering could be suppressed by the frustration. Characteristic feature is the finite susceptibility remaining at zero temperature. Thus, the $(CN)_3$ salt is one of the candidates for the quantum spin liquid materials.

Table 1.2: Physical parameters of κ-$(ET)_2X$

X	t'/t	U/W
$Cu(NCS)_2$	0.86	3.49
$Cu[N(CN)_2]Br$	0.68	3.57
$Cu[N(CN)_2]Cl$	0.75	3.79
$Cu_2(CN)_3$	1.06	4.09

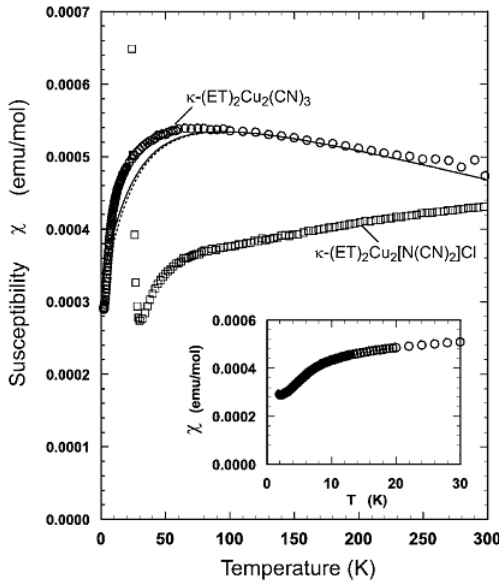

Figure 1.10: Magnetic susceptibility of κ-$(ET)_2X$ (X=$Cu_2(CN)_3$ and $Cu[N(CN)_2]Cl$).[11]

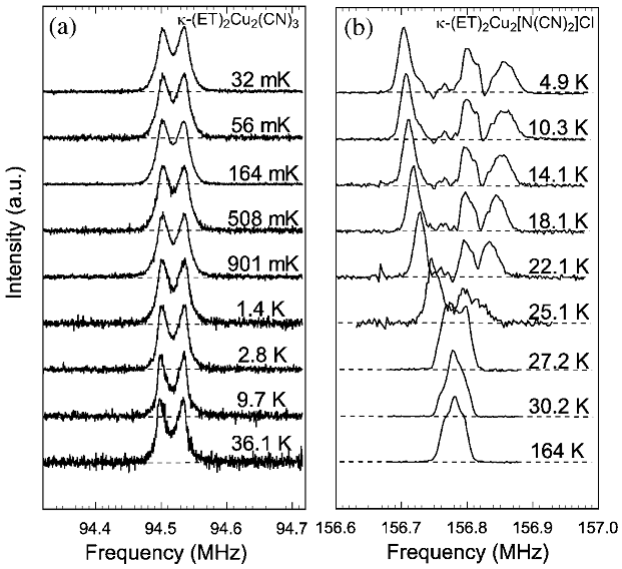

Figure 1.11: ^{1}H NMR spectra of κ-$(\mathrm{ET})_2X$ (X=$\mathrm{Cu_2(CN)_3}$ and $\mathrm{Cu[N(CN)_2]Cl}$).[11]

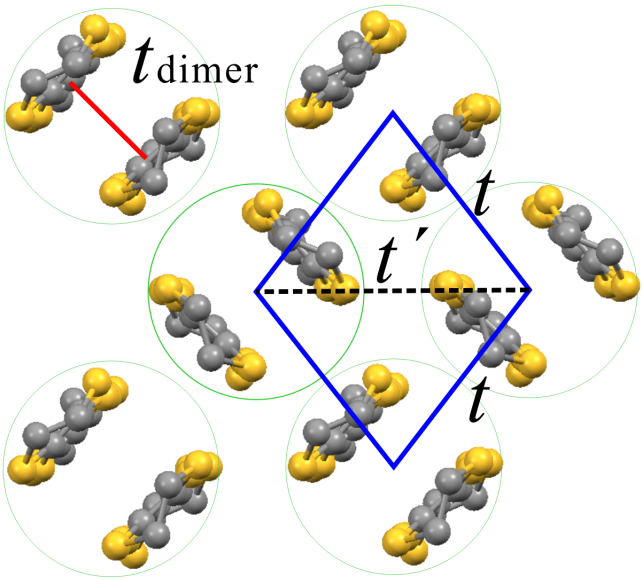

Figure 1.12: View of ET dimers in the bc plane. The interdimer transfer integrals are labeled by t and t', while the intradimer transfer integral is labeled by t_{dimer}.

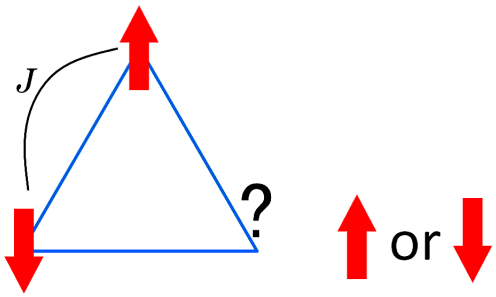

Figure 1.13: Antiferromagnetically interacting spins in a triangular lattice.

1.5 Optical and dielectric properties of insulating κ-$(ET)_2X$ salts

Figure.1.14 shows the optical conductivity of the Cl and $(CN)_3$ salts for the two in-plane polarizations[13]. In the Cl salt, the optical gap increases on decreasing temperature and arrives at $\Delta_\rho \sim 500$ cm^{-1} for $T = 20$ K. However, the optical conductivity of the $(CN)_3$ salt exhibits opposite temperature dependence. Moreover, it is difficult to identify a clear-cut energy gap at all temperatures in the $(CN)_3$ salt. This observation in the $(CN)_3$ salt is inconsistent with the Mott insulator picture with the finite energy gap due to Coulomb interaction. They suggested spin and charge fluctuations might play an important role in optical excitation.

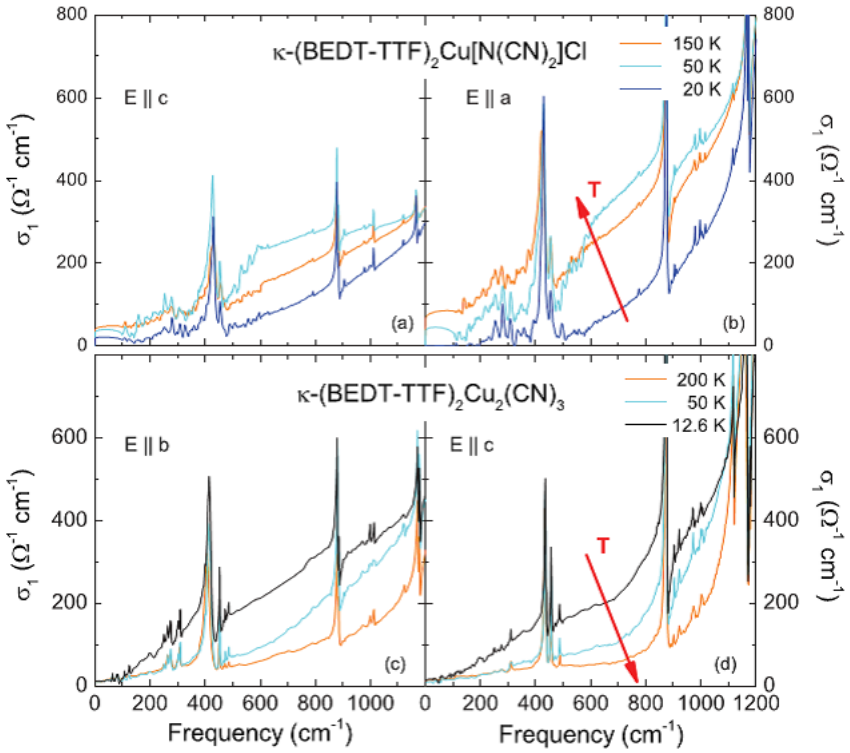

Figure 1.14: Optical conductivity of (a) and (b) κ-$(ET)_2X$ (X=Cu[N(CN)$_2$]Cl and (c) and (d) $Cu_2(CN)_3$) for the two in-plane polarizations.[13]

Figure 1.15 shows temperature dependence of the dielectric constant of the $(CN)_3$ salt measured at various frequencies[14]. Dielectric anomaly like relaxor ferroelectrics was observed in dimer Mott insulator which has no charge degrees of freedom. This result indicates the existence of interacting dielectric dipoles. They claimed that this electric dipole is ascribed to the charge disproportionation within the ET dimers driven by the inter molecular Coulomb interaction. They also evaluated the charge disproportionation to be $0.1e$ from the temperature dependence of the dielectric constant.

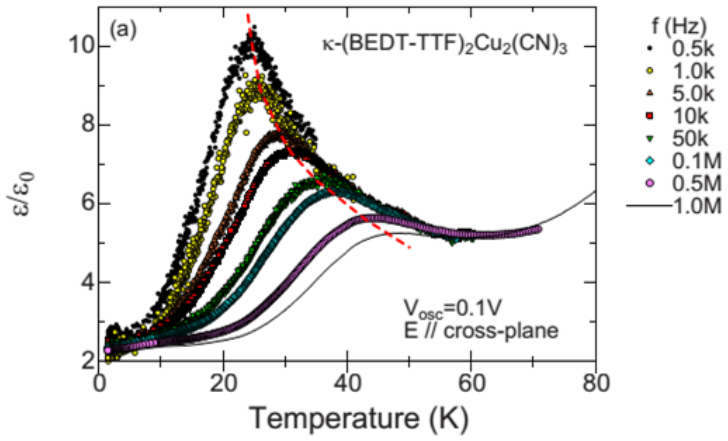

Figure 1.15: Temperature dependence of the dielectric constant with respect to various frequencies of κ-$(ET)_2Cu_2(CN)_3$.[14]

1.6 Inhomogeneity of electrons

Figure.1.16 shows temperature dependence of FWHM of ^{13}C NMR spectra of the aligned single crystals[15]. Broadening of the FWHM was observed upon cooling. The FWHM of a site which has larger hyperfine coupling constant is broader below 60 K. The ratio of the FWHM at the lowest temperature is almost the same as that of hyperfine coupling constant, indicating that inhomogeneity of the electron density on molecular sites develops. However, the ratio of the FWHM depends on temperature above 10 K because of the misalignment of aligned single crystals. Hence, more precise works of a single crystal have been desired.

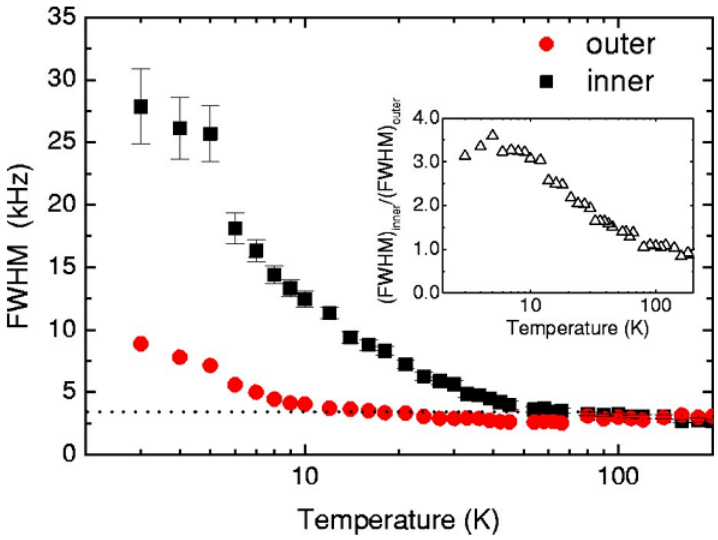

Figure 1.16: Temperature dependence of FWHM of ^{13}C NMR spectra of κ-$(ET)_2Cu_2(CN)_3$.[15]

K. Yakushi performed Raman spectroscopy to analyze the electronic state of the $(CN)_3$ salt. Figure.1.17 shows temperature dependence of FWHM of ν_2 which is a charge sensitive mode[16]. The author claimed the difference between case A and B was a slight difference of the transfer integrals. 0.07-0.1e was obtained for the amplitude of valence fluctuation from analysis of FWHM of ν_2 by two-state-jump model. The author suggested a wide size distribution of dipole cluster.

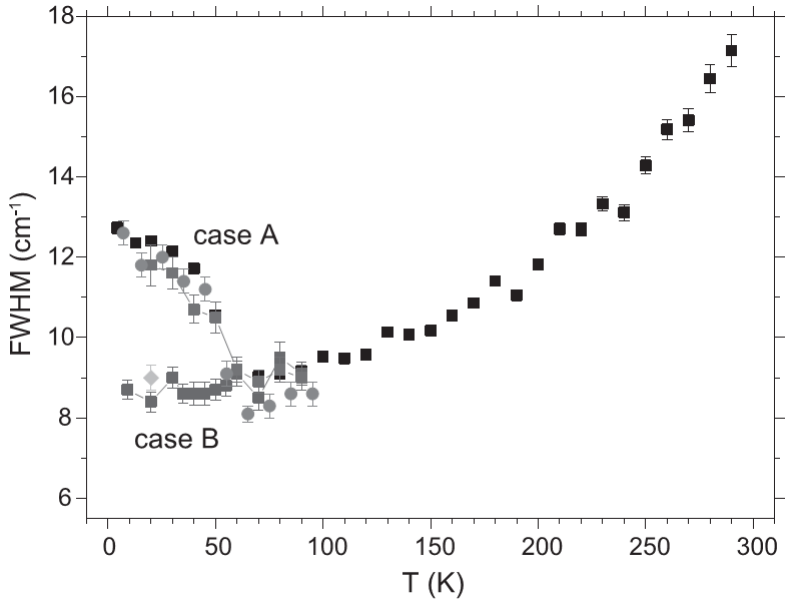

Figure 1.17: Temperature dependence of FWHM of ν_2.[16]

M. Pinteić *et al.* characterized the anisotropic charge response by dc conductivity, Hall effect, and dielectric spectroscopy[17]. They analyzed the data by variable range hopping (VRH) model which is based on the disordered system. They suggested that the conductivity should increase as disorder increases. Sample dependence of the T_0, which is a VRH parameter, indicates the presence of a different degree of the structural disorder in the anion subsystem. They claimed that the disorder in the CN^- groups acts on the ET layers via the hydrogen bonds, where it alters the charge distribution and causes domain boundaries as shown in Fig.1.19-1.20 and the localization in the $(CN)_3$ salt has two distinct origins: in addition to the Mott localization due to strong electron-electron interaction, the inherent disorder provides another mechanism through the Anderson process.

By considering the Anderson localization picture pointed out by A. Kawamoto *et al.*[15, 18] and M. Pinteić *et al.*[17], no charge gap in the optical and DC conductivity measurements can be naturally explained as a disordered metal. Theoretical approaches of correlated electron system with disorder [19, 20, 21] may be suitable to describe physics in the $(CN)_3$ salt.

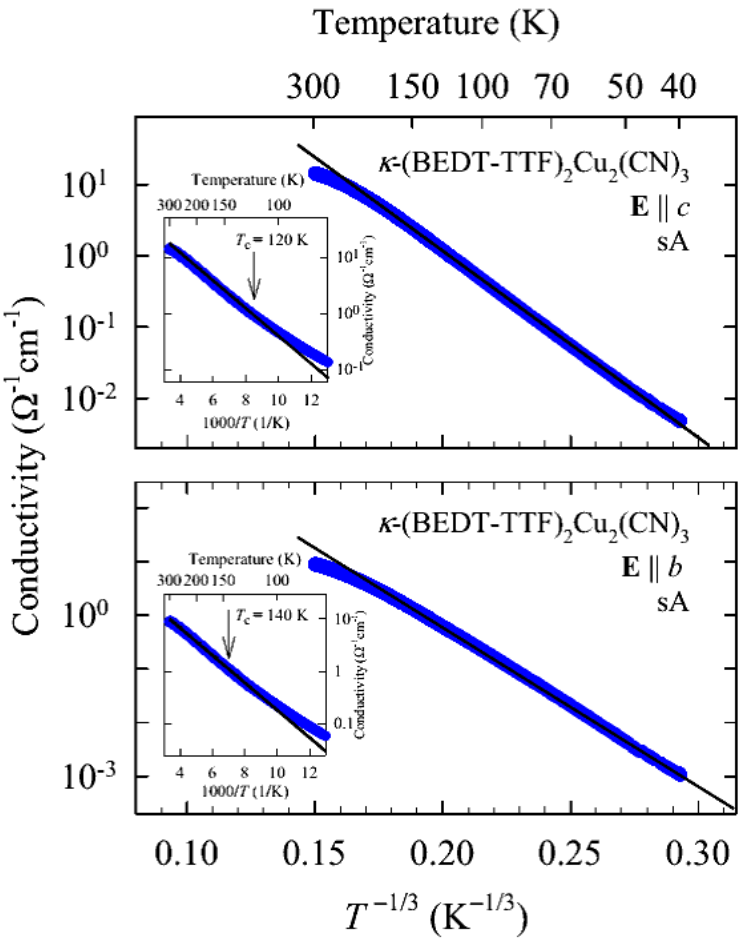

Figure 1.18: The dc conductivity as a function of $T^{-1/3}$ of κ-$(ET)_2Cu_2(CN)_3$. Upper panel: $E \parallel c$. Lower panel: $E \parallel b$. The conductivity follows a simple activation above cross over temperature T_c (full line in the inset) indicating nearest-neighbor hopping. Below T_c, the observed behavior corresponds to the regime of variable-range hopping in two dimensions $\sigma(T) = \exp[-(T_0/T)^{1/3}]$[17]

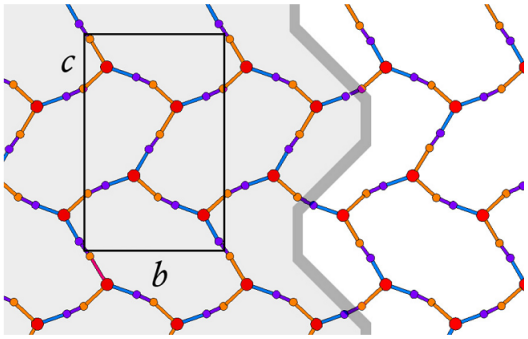

Figure 1.19: View of the anion network in the *bc* plane. Gray thick line denotes the domain boundary.[17]

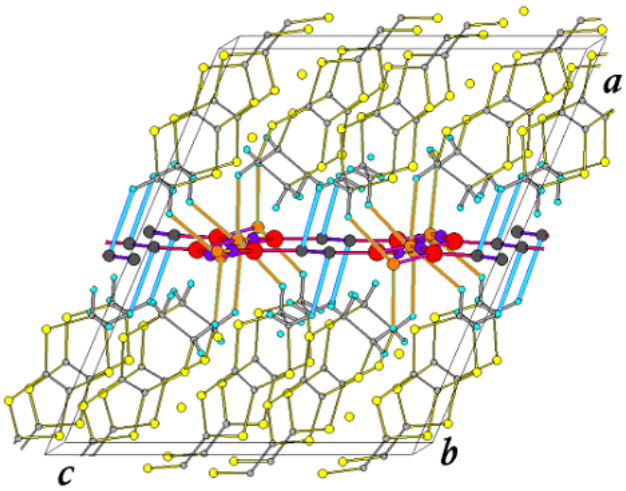

Figure 1.20: Possible hydrogen bonds between CH_2 groups of the ET molecules and CN^- groups of the anion network are indicated by orange and cyan full lines.[17]

1.7 Disorder effect

In order to investigate the disorder effects of the κ-$(ET)_2X$ salts, X-ray irradiation experiments were performed. Figure1.21 shows temperature dependence of the in-plane resistivity in the Cl and $(CN)_3$ salts at several irradiation dose[22]. Both salts exhibits an activation type behavior before irradiation. With increasing the irradiation dose, the resistivity decreases. In the Cl salt, metal-like behavior was observed with small irradiation dose. Although it took a lot of irradiation dose in $(CN)_3$ salt, metal-like behavior was observed only in the narrow temperature region above about 230 K in inset of Fig.1.21.

Figure 1.22 shows infrared optical reflectivity and conductivity of the Cl salt before and after X-ray irradiation[22]. Broad absorption peaks at 2250 cm^{-1} and 3350 cm^{-1} corresponds to interband transitions in the Mott-Hubbard bands and dimer bands, respectively. In addition, an optical gap attributed to a Hubbard gap appears, approximately below 1000 cm^{-1} in non-irradiated sample. The spectral weight (SW) in the mid-infrared region shifts to the far-infrared region with irradiation. This result indicates that randomness by X-ray irradiation filled the Mott gap by the SW transfer from the interband transition. However, no-Drude response and high dc resistivity suggested that the system remains still in the insulating state. Hence, the author claimed that disorder introduced by X-ray irradiation changed the Mott insulating state of the Cl salt to a soft Hubbard gapped insulating state as shown in Fig.1.24(d).

Figure 1.23 shows ^1H NMR spectra of the Cl salt before and after 500-hour X-ray irradiation [23]. Nonirradiated κ-Cl salt exhibits peak splitting below 27 K due to commensurate AF transiton, whereas X-ray irradiated κ-Cl salt does not exhibit peak splitting and line broadening, indicating that X-ray irradiation suppressed magnetic ordering.

Disorder or randomness is the source of the localization in strongly correlated electron systems. In this case, an electron localizes by the impurity scattering, so called Anderson insulator in Fig.1.24(b). Contrary to the Mott insulator, there exists no gap in Fermi surface in Fig.1.24. H. Shinaoka *et al.* predicted that soft Hubbard gap whose density of state was zero only at E_F emerged by introducing disorder to the strongly correlated electron system[21]. Due to a competition between the electron correlation and randomness, Mott-Anderson transition in Fig.1.24(c) is expected. Therefore, it is interesting to investigate the relation between physical properties and

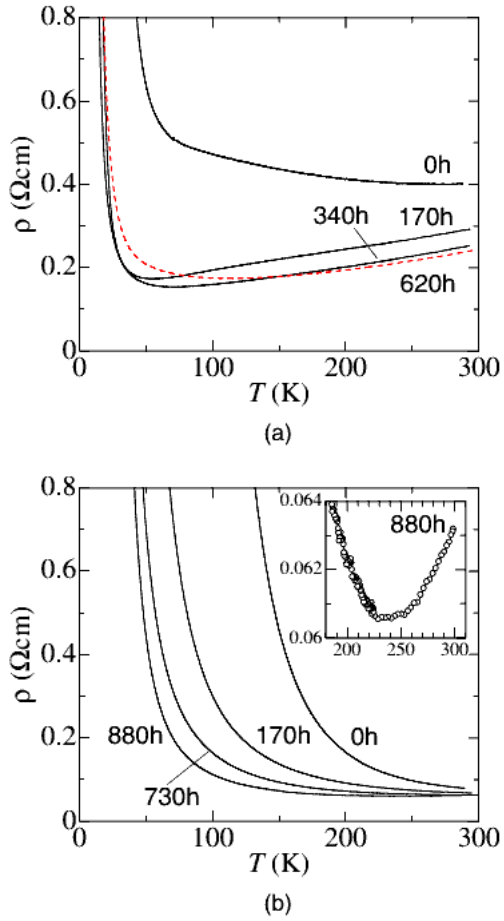

Figure 1.21: Temperature dependence of in-plane resistivity in (a) κ-$(ET)_2Cu[N(CN)_2]Cl$ and (b) κ-$(ET)_2Cu_2(CN)_3$. The time indicated at each curve is the total irradiation time. The inset is the enlarged view of the data in high temperature region after total 880 h irradiation.[22]

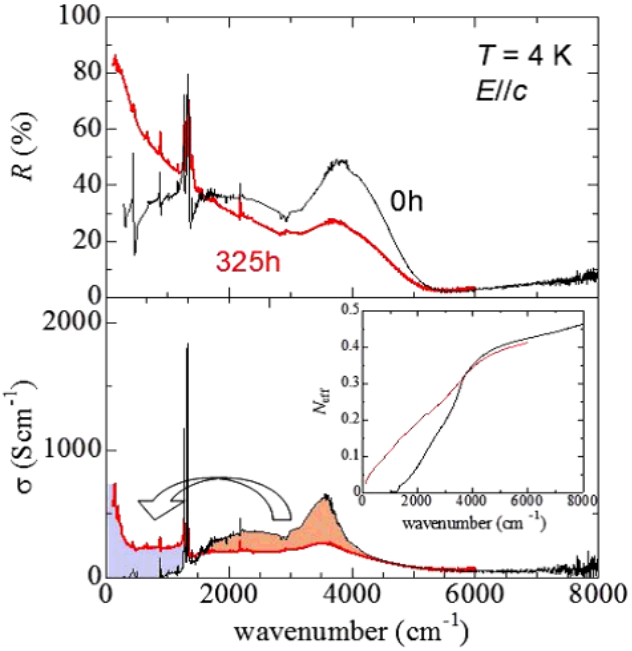

Figure 1.22: Infrared optical reflectivity and conductivity of κ-$(ET)_2Cu[N(CN)_2]Cl$ before and after X-ray irradiation. The inset of the lower panel indicates the effective number of carries N_{eff}.[22]

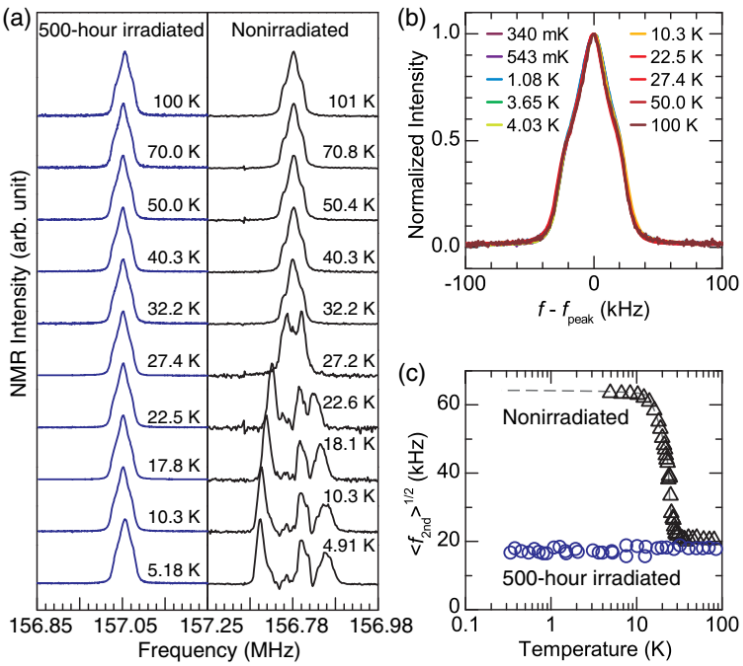

Figure 1.23: Disappearance of antiferromagnetic order in the κ-Cl crystal after 500-h x-ray irradiation. (a) The temperature dependence of ^{1}H NMR spectra of the 500-h x-rayirradiated and nonirradiated κ-Cl crystals. (b) ^{1}H NMR spectra of the 500-h x-ray-irradiated κ-Cl crystal normalized to the maximum values at temperatures between 340 mK and 100 K. $f_{\rm peak}$ is the frequency at which the spectra have the maximum intensity. (c) The temperature dependence of the square root of the second moment of NMR spectra, $\langle f_{\rm 2nd}\rangle^{1/2}$, for the 500-h x-ray-irradiated crystal (blue circles) and the nonirradiated crystal (black triangles). The dashed line guides the eye. The slight difference in the line shape and $\langle f_{\rm 2nd}\rangle^{1/2}$ above 30 K between the two measurements is most likely due to a slight difference in the field geometry against the crystal axes, to which the line shape is sensitive. [23]

disorder in the $(CN)_3$ salt.

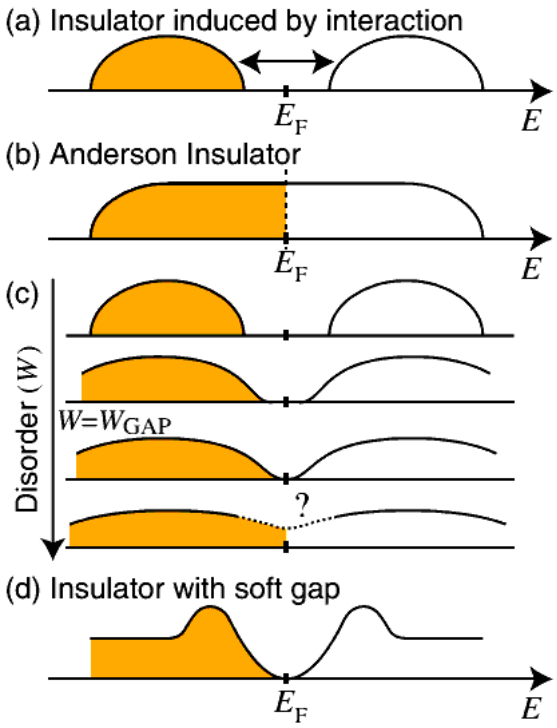

Figure 1.24: Schematic of insulators with different types of gaps in the single-particle density of states: (a) insulator induced by interaction, (b) Anderson insulator, (c) disorder dependence of a single particle gap, and (d) insulator with soft gap.[21]

1.8 Impurity substitution in conducting layer

It should be noted that X-ray irradiation affects mainy on the surface of crystals because of the absorption and produces free radicals on the surface. Therefore, it is difficult to investigate magnetic properties on X-ray irradiated samples. Moreover, it is unclear whether X-ray irradiation introduces disorder to conduction plane. One alternative method is the impurity substitution with donor molecules which can directly introduce disorder in the conduction layer. Thus, the impurity substitution is appropriate for the study of disorder, however few studies were performed because of the following reasons. (i) The sample preparation of the electrochemical oxidation works as a purification process so that the impurity is rarely included. (ii) In cuprates or heavy fermion materials, it is easy to evaluate substitution value and uniformity using the elemental analysis. Contrastly, in organic conductors, it is difficult to utilize the elemental analysis because the impurity molecule often consists of the same C, H, S atoms.

Recently, we focused on a STF (STF: bis(ethylenedithio)diselenadithiafulvalene) molecule in which one side of S in the central ring of the TTF skeleton are replaced with Se atoms in Fig.1.25. The advantages of the substitution of STF for ET molecules are (i) structural distortion is minimized because ET and STF have almost the same molecular structure, (ii) wide spreaded Se $4d$ orbital makes sufficient disorder into the intermolecular transfer integrals, (iii) evaluation of substitution value and uniformity by elemental analysis can be possible utilizing the Se atoms which exist only on impurity sites. Thus, the STF substitution is one of the candidates for the study of the disorder.

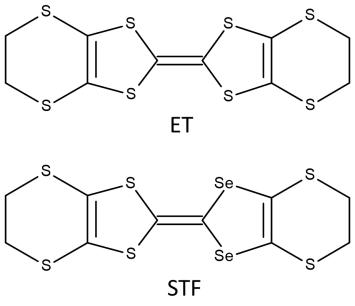

Figure 1.25: Molecular structure of ET and STF.

Transfer integrals around STF are modified by the orbital of Se on STF, distorting the triangular lattice locally by the impurity substitution. As a result, the geometrical frustration is suppressed. If the behavior of the absence of magnetic order in the $(CN)_3$ salt is due to the geometrically frustrated spins, the short-range magnetic order might emerge by suppressing the frustration. Therefore, we performed ^{13}C NMR in order to elucidate magnetic properties in the $(CN)_3$ salt, with the STF substitution.

1.9 Organic conductor λ-D_2MX_4

Organic conductor λ-D_2MX_4 is also quasi-two dimensional organic conductor like κ-type salts. λ-D_2MX_4 consist of donor molecules D with the tetrahedral anions MX_4 (M=Ga, Fe ; X=Cl, Br) and form charge-transfer salts with two-dimensional layered structures as shown in Figs. 1.26(a)-(c). The band structure and Fermi surface of λ-type salts are shown in Figs.1.26(d). Lattice parameters are shown in Table 1.3. With the charge transfer of one electron per two donor molecules, these compounds shows quasi-two dimensional electronic systems forming a dimer in the conducting layer [24]. Among these salts, λ-$(BETS)_2MCl_4$ (M=Ga, Fe) salts have attracted much attention because they show novel superconductivity. The λ-$(BETS)_2GaCl_4$ shows superconductivity around 5 K at ambient pressure [25] and the d-wave SC gap structure was reported by a specific heat measurement [26]. Moreover, the superconducting state persists under higher magnetic field applied just parallel to the conducting layers, suggesting the possible FFLO state appears in the vicinity of critical filed H_{c2} [27]. The salt of λ-$(BETS)_2FeCl_4$, which is isostructural with λ-$(BETS)_2GaCl_4$ is an insulator in zero magnetic field. However, when a strong magnetic filed is applied parallel to the conducting layers, superconductivity emerges, which is called the field induced (FISC) state [28, 29]. The possible FFLO state was also suggested at the phase boundary of FISC phase. Therefore, λ-type salts provide rich physical properties and have attracted considerable attention.

1.10 Resistivity for λ-D_2GaCl_4

Figure 1.27 shows pressure dependence of resistivity forλ-D_2GaCl_4. The resistivities of both ET and STF salts show insulating behavior, and BETS

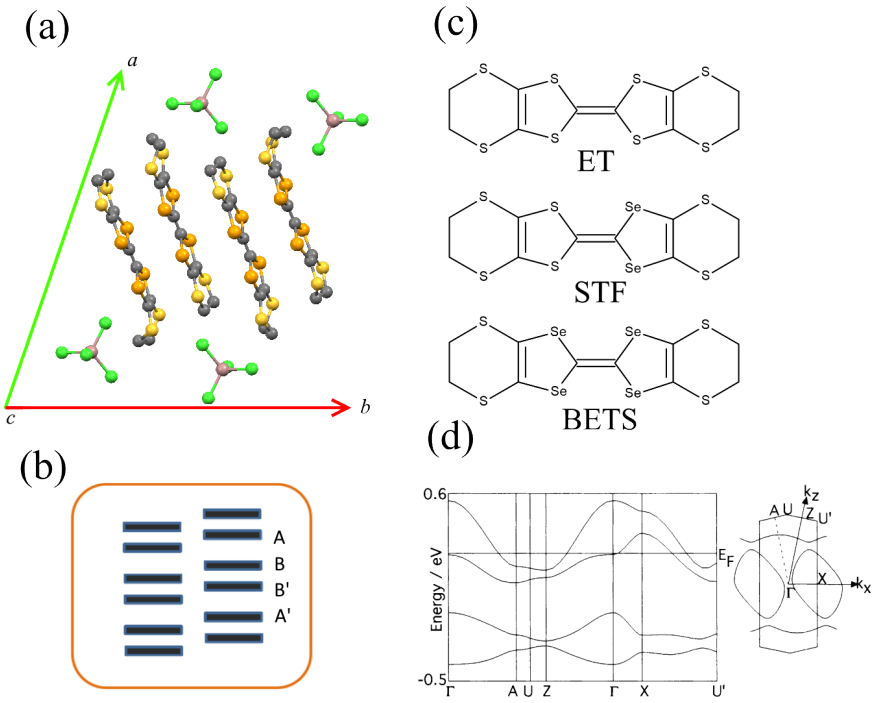

Figure 1.26: (a) Crystal structure of λ salts. (b) Dimer arrangement of λ salts. There are two crystallographically independent molecules A and B. The molecule with ' indicates the molecule derived by the inversion symmetry. (c) Molecular structure of ET, STF, and BETS. (d) Band structure and Fermi surface of λ-$(ET)_2GaCl_4$.

Table 1.3: Crystallographic data of λ-D_2GaCl_4.

D	ET	STF	BETS
Space group	$P\bar{1}$	$P\bar{1}$	$P\bar{1}$
a (Å)	16.246(5)	16.203(8)	16.172(3)
b (Å)	18.027(5)	18.316(9)	18.616(2)
c (Å)	6.533(7)	6.573(2)	6.607(2)
α (Å)	98.20(5)	98.41(4)	98.38(2)
β (Å)	97.48(6)	97.03(3)	96.75(3)
γ (Å)	112.29(2)	112.42(4)	112.56(2)
V (Å^3)	1716(2)	1750(15)	1784.2(8)

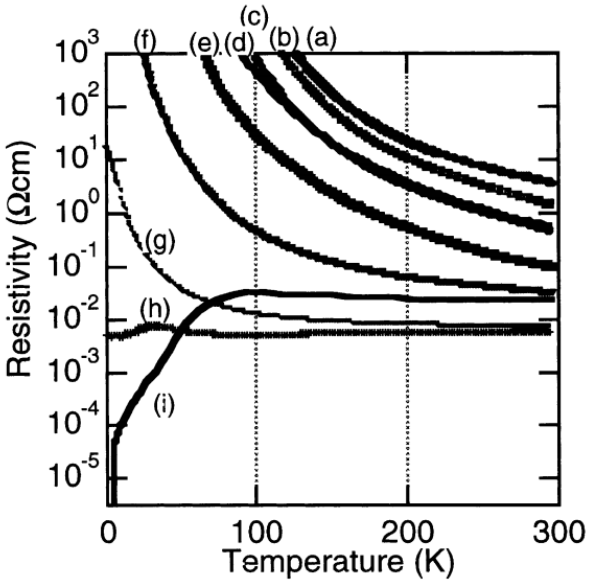

Figure 1.27: Pressure dependence of resistivity for λ-D_2GaCl_4 [30]. (a) 1 bar, (b) 4.5 kbar, and (c) 16.5 kbar for ET salt. (d) 1 bar, (e) 4.5 kbar, (f) 13.5 kbar, (g) 17.3 kabar, and (h) 18 kbar for STF salt. (i) 1 bar for BETS salt.

salt shows superconductivity (i). With increasing pressure, the resistivity decreases. The resistivity of λ-$(ET)_2GaCl_4$ at 16.5 kbar (c) corresponds to that of λ-$(STF)_2GaCl_4$ at ambient pressure (d). Figure 1.28 shows detailed resistivity of λ-$(STF)_2GaCl_4$ under pressure. λ-$(STF)_2GaCl_4$ shows superconductivity above 1.22 GPa. Therefore, subsitution of the donor molecules is understood in terms of chemical pressure effect.

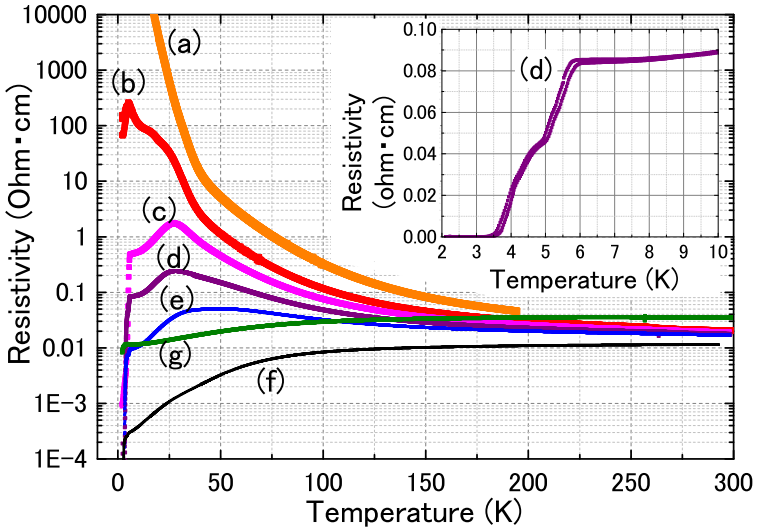

Figure 1.28: Temperature dependence of the electrical resistivity of λ-$(STF)_2GaCl_4$ at various pressures: (a) 1.10, (b) 1.22, (c) 1.27, (d) 1.31, (e) 1.35, (f) 1.60, and (g) 1.90 GPa.

1.11 Magnetic property for λ-D_2GaCl_4

Figure 1.29 shows results of electron pin resonance (ESR) measurements for λ-$(ET)_2GaCl_4$. The linewidth gradually decreases with decreasing temperaure and shows upturn around 13 K. The intensity is almost constant above 20 K and suddenly drops below 13 K. Since ESR intensity corresponds to spin susceptiblity, these results suggest possibility of AF transition.

Figure 1.30 shows magnetic susceptibility for λ-$(STF)_2GaCl_4$ and the magnetic susceptibility is fitted by $S = 1/2$ Heisenberg AF model in a triangular lattice with an exchange coupling constant $J = 165$ K. The magnetic

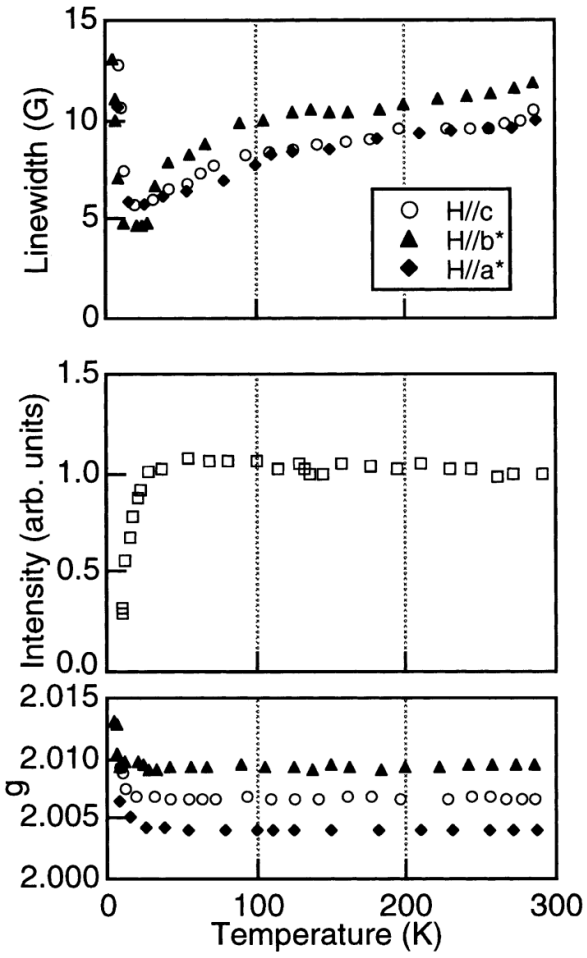

Figure 1.29: ESR measurements of linewidth, intensity, and g value for λ-$(ET)_2GaCl_4$[30].

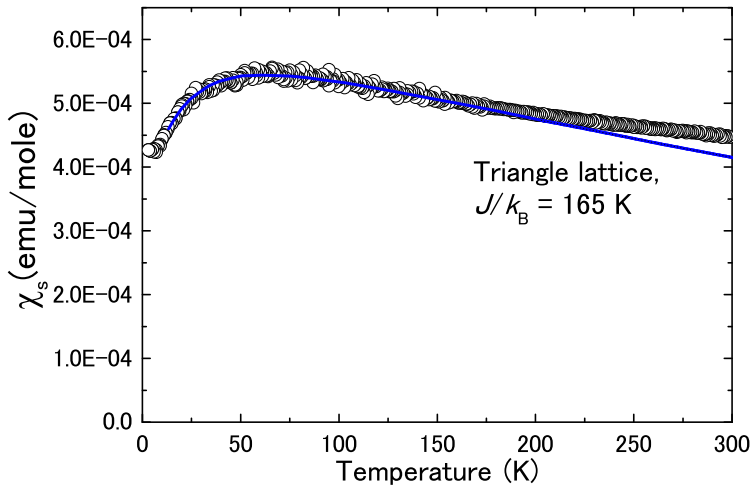

Figure 1.30: Temperature dependence of the static spin susceptibility in λ-$(STF)_2GaCl_4$ measured on a powdered sample of 10.8 mg. Open circles represent the measurements. Core diamagnetisms was -3.80$\times 10^{-4}$ emu/mol and Curie-Weiss components were subtracted from the original data. Solid line is the susceptibility curve calculated for the $S = 1/2$ Heisenberg AF model in a triangular lattice with an exchange coupling constant $J = 165$ K.

susceptibility increases gradually and has broad maximum around 70 K. Below 70 K, The magnetic susceptibility decreases and has finite value at low temperature. Therefore, no magnetic ordering was obeserved down to 2 K.

1.12 Phase diagram of λ-D_2GaCl$_4$

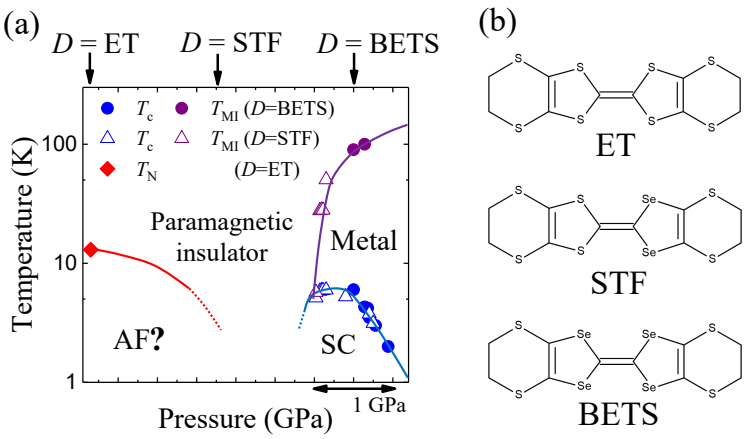

Figure 1.31: (a) Pressure-temperature phase diagram of λ-D_2GaCl$_4$ (D = ET, STF, and BETS). T_c, T_{MI}, and T_N represent the superconducting transition temperature, metal–insulator transition temperature, and Néel temperature, respectively. The data are cited from Refs. [31, 30, 32]. (b) Molecular structure of ET, STF, and BETS.

Figures 1.31(a) and 1.31(b) show $P-T$ phase diagram of λ-D_2GaCl$_4$ and structure of donor molecules, respectively. Previous results demonstrate that λ-(ET)$_2$GaCl$_4$ and λ-(us-STF)$_2$GaCl$_4$ are located in the insulating phase adjacent to the SC phase. Note that the SC state of λ-(ET)$_2$GaCl$_4$ is not confirmed because of a lack of high pressure experiments. Unlike κ salts, no clear magnetic ordering was reported in the insulating phase.

Chapter 2

Purpose

The pairing mechanism of the unconventional superconductivity is closely related to the nature of the adjacent insulating phase. In the case of organic superconductors, various mechanisms of superconductivity are suggested[33, 34]. The superconducting (SC) phase in κ-type ET (ET) [bis(ethylenedithio)tetrathiafulvalene] system is located near an antiferromagnetic (AF) Mott insulating phase, and AF spin fluctuation plays a crucial role for the emergence of the superconductivity [5]. Therefore, the magnetic nature of the insulating phase is of significant research interest.

In this theis, I chose two typcal organic donductors, κ and λ salts to investigate the relation among the magnetism, the superconductivity, and the frustration.

2.1 Determination of the hyperfine tensor in κ-$(ET)_2X$ (X=Cu[N(CN)$_2$]Br, Cu(NCS)$_2$) on central ^{13}C sites

Detailed NMR studies of κ-$(ET)_2X$, including evaluations of electron correlation and the possibility of FFLO, require precise hyperfine coupling tensors. The hyperfine coupling tensor of ET salts may be expected not to depend significantly on their crystal structure because the hyperfine field is mainly due to the on-site p_z orbitals [10]. However, angle dependences of NMR spectra at 15, 60, and 200 K in charge ordering salt α'-$(ET)_2IBr_2$ suggested that the off-site dimer contribution be considered [35].

Most ^{13}C-NMR studies of ET salts have been performed on molecules in which both carbon sites of the central C=C bond were enriched [36, 37, 10]. In these molecules, the dipole coupling between ^{13}C=^{13}C splits a single peak into doublet peaks and modulates the sinusoidal angle dependence of each peak (the Pake doublet problem [38]). These multi-peak spectra make it difficult to determine the hyperfine coupling tensor from measurements by angle rotation. Although a few hyperfine coupling tensors of the κ-Br salt have been reported [37], none of the κ-NCS salts has been determined.

2.2 Site-specific ^{13}C NMR study on locally distorted triangular lattice of organic conductor κ-$(ET)_2Cu_2(CN)_3$

Experimental observations in $(CN)_3$ salt have been explained through triangular-lattice or disordered-state models. Therefore, experimental verification is required to determine whether the observed behavior is due to the the geometrical frustration of the spins in the triangular lattice or to a disordered state. One approach is to artificially distort triangular lattices.

It is expected that local impurities induce staggered moments at the center of disorder in the vicinity of antiferromagnetic compounds. However, few NMR studies of impurity sites exist. To address this void, we substitute ^{13}C enriched STF for non-enriched ET molecules so that ^{13}C-NMR targets the impurity sites.

2.3 ^{13}C NMR study of insulating phase in λ-D_2GaCl_4 (D= ET and STF)

λ-$(ET)_2GaCl_4$ and λ-(us-STF)$_2GaCl_4$ are located in the insulating phase adjacent to the SC phase as shown in the general phase diagram in Fig. 1.31(a). At present, only an ESR measurement in λ-$(ET)_2GaCl_4$ suggested the possibility of AF transition [30]. Therefore, the magnetic nature of the insulating phase is still not clear and it is of significant research interest if AF spin fluctuation exists in the insulating phase.

Chapter 3

Experimental

3.1 κ-$(ET)_2X$ (X=Cu[N(CN)$_2$]Br, Cu(NCS)$_2$

Single crystals were prepared by the electrochemical oxidation of ET in 1, 1, 2-trichloroethane in the presence of CuBr and $(C_6H_5)_4P[N(CN)_2]$ for κ-$(ET)_2Cu[N(CN)_2]Br$ and in the presence of CuSCN, KSCN, and 18-rown-6 ether for κ-$(ET)_2Cu(NCS)_2$ [39, 40]. Crystal orientation was determined by X-ray diffraction. Crystal shapes and their corresponding axes are shown in Fig.3.2. NMR experiments was performed at 7 T on a lab-made heterodyne spectrometer with Oxford superconducting solenoidal magnet system. The angle dependences of the spectra of κ-NCS were measured in the a^*b, bc, and a^*c planes at 150 K, whereas those of the κ-Br salt were measured in the ab, bc, and ac planes at 175 K to avoid line broadening caused by the development of incommensurability [37].

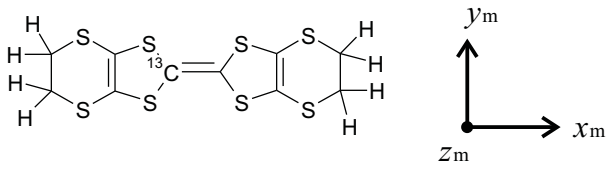

Figure 3.1: Molecular structure of single site enriched ET with the definition of its molecular coordinates.

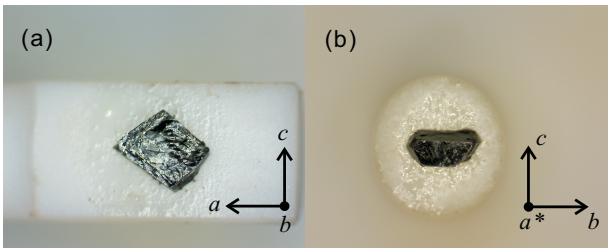

Figure 3.2: Shapes and orientations of the single crystals used for the experiment. (a) κ-Br. (b) κ-NCS.

3.2 κ-$[(ET)_{1-x}(STF)_x]_2Cu_2(CN)_3$

Single crystals of κ-$[(ET)_{1-x}(STF)_x]_2Cu_2(CN)_3$ of various stoichiometry ($x = 0$, 0.05, and 0.06) were prepared by the electrochemical oxidation of ET and STF in 1, 1, 2-trichloroethane containing 10 % ethanol in the presence of CuCN, KCN, and 18-crown-6 ether. [41]. Using energy-dispersive x-ray spectroscopy with κ-$(STF)_2Cu_2(CN)_3$ as a reference, the impurity fraction x was determined by comparing the intensity of S atoms to that of Se atoms. Samples with x=0 and 0.05 consisted of ^{13}C-enriched ET and non-enriched STF, and a sample with $x = 0.06$ consisted of ^{13}C-enriched STF and non-enriched ET. DC conductivity was measured along the c axis from room temperature down to 40 K for the pure and $x = 0.05$ samples by the standard four-point probe technique. DC magnetization was measured for polycrystalline samples as a function of temperature from 300 to 2 K in a 2 T magnetic field using a magnetometer that is based on a superconducting quantum interference device. NMR experiments were performed for each single crystal in a 7 T magnetic field applied perpendicular to conduction plane.

3.3 λ-D_2GaCl_4

Single crystals were prepared by the electrochemical oxidation of donor molecules in 1, 1, 2-trichloroethane for λ-$(ET)_2GaCl_4$ and chlorobenzene for λ-$(STF)_2GaCl_4$ in the presence of tetra-n-butylammonium (TBA) $GaCl_4$ [42].

The magnetic susceptibility was measured using powder samples for λ-$(ET)_2GaCl_4$ as a function of temperature from 300 K to 2 K in a magnetic field of 1 T. NMR experiments were performed in a magnetic field of 7 T applied to [110] direction (almost parallel to long axis of ET). Crystal orientation was determined by X-ray diffraction.

3.4 ^{13}C enriched samples and NMR configuration

One side of the central C=C bond in donor molecules was enriched with ^{13}C isotope to avoid the Pake doublet problem [38] by a cross-coupling method[43], as shown in Fig. 3.3. NMR spectra were obtained by the fast

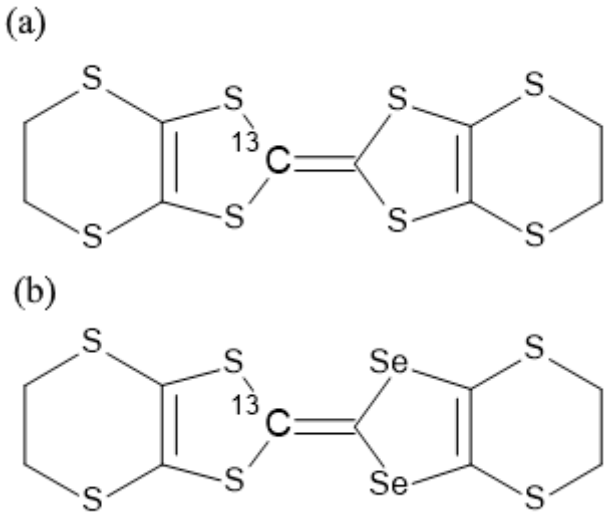

Figure 3.3: Molecular structure of single site enriched (a) ET and (b) STF.

Fourier transformation of the spin echo signal with a $\pi/2-\pi$ pulse sequence. The NMR shifts are given in MHz or ppm which is relative to tetramethylsilane (TMS). The spin-lattice relaxation rate, T^{-1}, was measured using the conventional saturation-recovery method. The linewidths were evaluated by fitting peaks to the Lorentz function and the spin-spin relaxation rate, T_2^{-1}, was defined as the rate corresponding to Lorentz decay.

Chapter 4

Results

4.1 κ-$(ET)_2X$ (X=Cu[N(CN)$_2$Br, Cu(NCS)$_2$)

4.1.1 Crystal structures of κ-salts and their expected NMR spectra

ET molecules form dimers in κ-$(ET)_2X$. As shown in Fig.4.1 (a)-(b), the manners of overlap, which are off the long axes of ET molecules, were almost the same among these salts. The space group of κ-Br is P_{nma}, with dimers located on the inversion center [44]. This results in two crystallographically independent ^{13}C sites, shown as the inner and outer sites in Fig.4.1 (c). In contrast, the space group of κ-NCS salt is $P2_1$, a non-centrosymmetric system [45], and there are four crystallographically independent ^{13}C sites, represented as two inner and two outer sites. The κ-Br salt has a double layer structure along the a axis, containing four crystallographic equivalent dimers represented as A, B, C and D per unit cell (Fig.4.2). When a magnetic field is applied, these four dimmers become magnetically non-equivalent, and $2 \times 4 = 8$ resonance lines are expected. The κ-NCS salt has a single layer structure along the c axis, containing two crystallographic equivalent dimers, A and B, representing two crystallographically independent molecules per unit cell (Fig.4.3), and 4×2=8 resonance lines are expected in an arbitrary field.

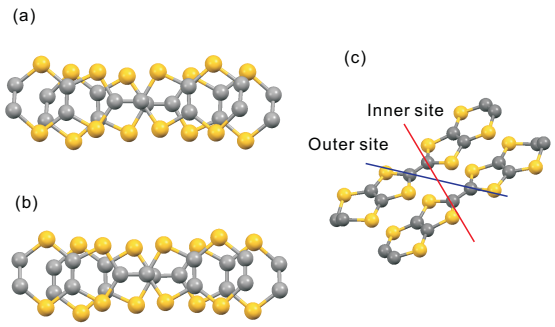

Figure 4.1: Overlaps of ET dimers. (a) κ-Br (b) κ-NCS (c) inner and outer sites of a dimer.

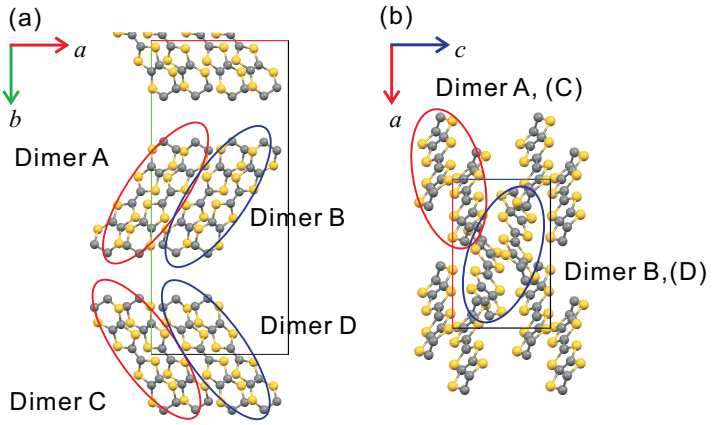

Figure 4.2: Composite diagram of κ-Br. Views along the (a) c and (b) b axes. The circles represent dimers.

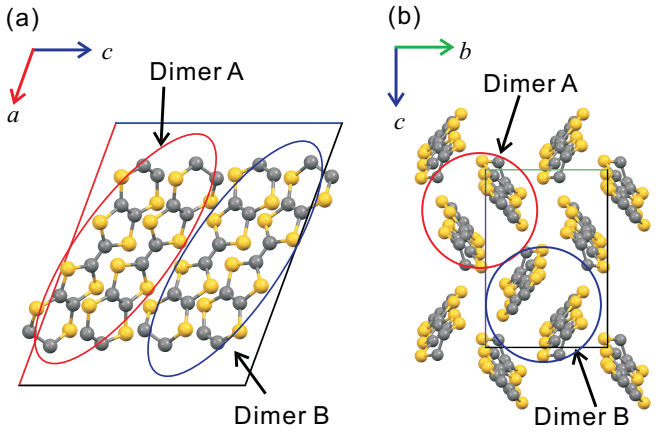

Figure 4.3: Composite diagram of κ-NCS. Views along the (a) b and (b) a axes. The circles represent dimers.

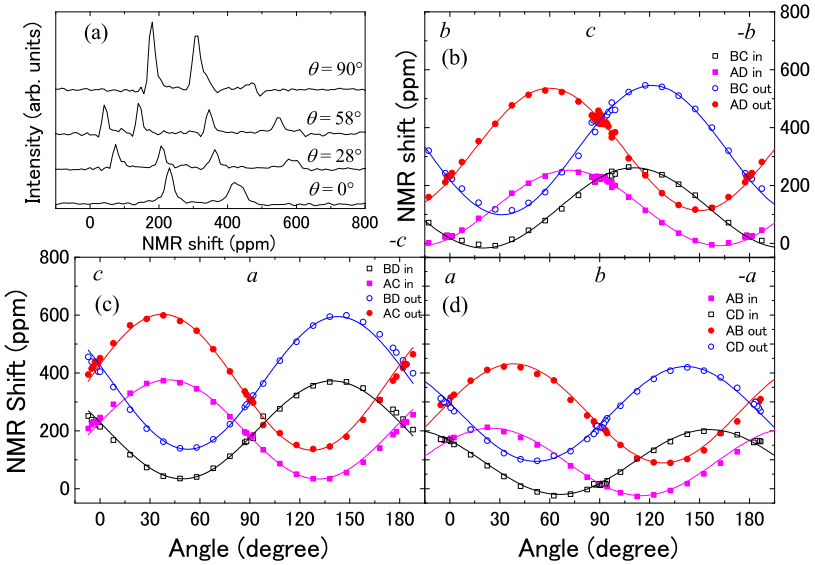

Figure 4.4: (a) Angle dependences of NMR spectra of κ-Br in the conduction plane. θ is the angle relative to the a axis. (b-d) Angle dependences of the NMR Shift rotated about the (b) a, (c) b, and (d) c-axes.

4.1.2 κ-$(ET)_2Cu[N(CN)_2]Br$

Figure 4.4 (a) shows the angle dependences of NMR spectra in the conduction plane for κ-Br. Two peaks were observed from the inner and outer sites for the magnetic field parallel to the crystal axis (θ=0, 90° correspond to $H \parallel c$, a, respectively), whereas four peaks were observed for an arbitrary field direction in the ac plane, in which two dimers became magnetically non-equivalent. Figure 4.4 (b)-(c) shows the angle dependence of the NMR shift for the field rotated about each crystal axis. A clear sinusoidal angle dependence was observed without additional modulations. Peaks could be assigned by comparing the directions of the p_z orbital of these dimers. The outer and inner sites on the each dimer should show the same angle dependence, as the directions of the p_z orbitals of these two sites are almost parallel to each other. For the rotation in the conduction plane (the rotation about the b axis), pairs of open and closed symbols were assigned to the signals from the same respective dimers. The crystal structures indicate that the dimers of A and C and the dimers of B and D are magnetically equivalent in this rotation. Rotation of the magnetic field from the c to the a axis (Fig. 4.2 (b)) is expected to maximize the NMR shift of dimer A, (C), in which the magnetic field is parallel to p_z on the dimer, as well as to minimize the shift of dimer B, (D), in which the magnetic field is perpendicular to p_z on the dimer. Thus, the closed symbols should be assigned to dimers of A and C and the open symbols to dimers of B and D. Other rotations can be assigned in the same way. For rotations about the a axis, the closed symbols corresponded to the dimers of A and D and the open symbols to the dimers of B and C; whereas, for the rotations about the c axis, the closed symbols corresponded to the dimers of A and B and the open symbols to the dimers of C and D. Consistent with previous findings [46], the peaks of the inner sites were lower than those of the outer sites, with the circles representing the outer sites and the squares representing the inner sites. These assignments can be used to determine the NMR shift tensor, $\overleftrightarrow{\delta}$, in the crystal coordinate

system for dimer A as:

$$\begin{aligned}
\overleftrightarrow{\delta}_{A_{in}} &= \begin{pmatrix} \delta_{aa} & \delta_{ab} & \delta_{ac} \\ \delta_{ab} & \delta_{bb} & \delta_{bc} \\ \delta_{ac} & \delta_{bc} & \delta_{cc} \end{pmatrix} \\
&= \begin{pmatrix} 166(31) & 87(34) & 166(49) \\ 87(34) & 17(21) & 84(34) \\ 166(49) & 84(34) & 227(41) \end{pmatrix} \text{(ppm)} \\
\overleftrightarrow{\delta}_{A_{out}} &= \begin{pmatrix} 297(54) & 163(60) & 221(85) \\ 163(60) & 220(36) & 191(60) \\ 221(85) & 191(60) & 427(41) \end{pmatrix} \text{(ppm)}
\end{aligned}$$

The tensors for the other dimers can be obtained using the unitary operations:

$$\overleftrightarrow{\delta}_i = \overleftrightarrow{U}_i \overleftrightarrow{\delta}_A \overleftrightarrow{U}_i^{-1}$$

$$\overleftrightarrow{U}_B = \begin{pmatrix} 1 & 0 & 0 \\ 0 & 1 & 0 \\ 0 & 0 & -1 \end{pmatrix}$$

$$\overleftrightarrow{U}_C = \begin{pmatrix} 1 & 0 & 0 \\ 0 & -1 & 0 \\ 0 & 0 & 1 \end{pmatrix}$$

$$\overleftrightarrow{U}_D = \begin{pmatrix} -1 & 0 & 0 \\ 0 & 1 & 0 \\ 0 & 0 & 1 \end{pmatrix}$$

4.1.3 κ-$(ET)_2Cu(NCS)_2$

Figure 4.5 (a) shows the angle dependence of NMR spectra of κ-NCS in a magnetic field parallel to the conduction plane. Four peaks were evident when the magnetic field was parallel to the crystal axis (θ=0, 90° correspond to $H \parallel c, -b$, respectively), whereas eight peaks were observed for an arbitrary field direction in the bc plane because the dimers became magnetically non-equivalent. When the magnetic field was parallel to c axis ($\theta = 0°$), the two lower frequency peaks were almost in the same position, making the intensity of the lowest frequency peak about twice that of the other peaks. Figure 4.5 (b)-(c) shows the angle dependence of the NMR shift for the field rotated about each orthogonalized crystal axis, a^*, b, and c.

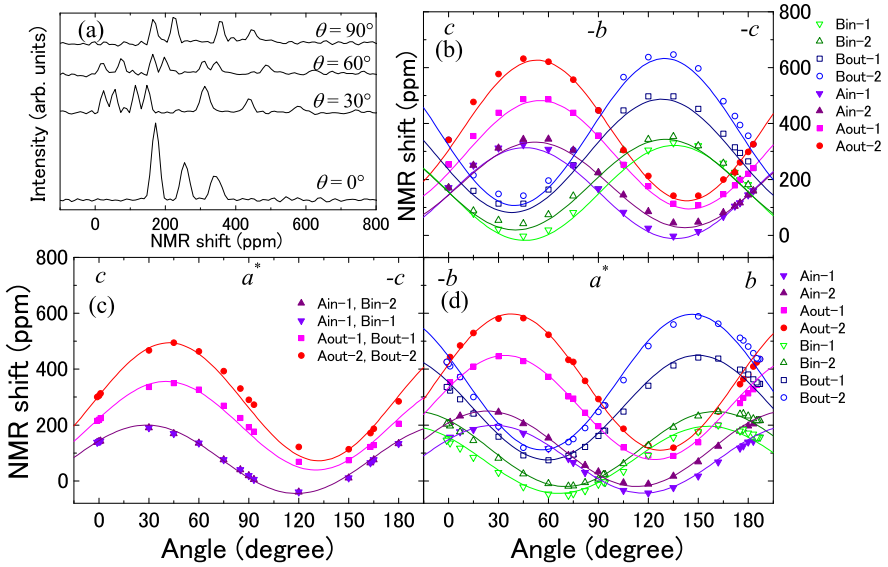

Figure 4.5: (a) Angle dependences of NMR spectra of κ-NCS in the conduction plane. θ is the angle measured relative to the c axis. (b-d) Angle dependences of NMR Shifts rotated about the (b) a^*, (c) b, and (d) c axes.

We also observed a clear sinusoidal angle dependence without additional modulations in the same way as for κ-Br. There were two dimers of A and B in a unit cell shown in Fig.4.3. When the magnetic field was rotated from c to $-b$ about the a^* axis, the NMR shifts of dimer A are expected to reach a maximum, while the shifts of dimer B are expected to reach a minimum (Fig.4.3 (b)). Thus, the closed symbols should be assigned to dimer A and the open symbols to dimer B. Similarly, for the rotation about the c axis, closed symbols should be assigned to dimer B and open symbols to dimer A. The two lower frequency peaks represent inner sites and the two higher frequency peaks represent outer sites in the same way as for κ-Br. For rotation about the b axis, there were three peaks with almost the same angle dependence as in Fig.4.5 (c), because the directions of the p_z orbital of all dimers were almost the same. Peaks can be assigned by comparing the shifts at $\theta = 0°$ and 90° in Fig.4.5 (c) with the shifts at $\theta = 0°$ in Fig.4.5 (b) and $\theta = 90°$ in Fig.4.5 (d), respectively. These assignments can be used to obtain NMR

shift tensors in the crystal coordinate system for dimer A.

$$
\begin{aligned}
\overleftrightarrow{\delta}_{A\,in-1} &= \begin{pmatrix} \delta_{a^*a^*} & \delta_{a^*b} & \delta_{a^*c} \\ \delta_{a^*b} & \delta_{bb} & \delta_{bc} \\ \delta_{a^*c} & \delta_{bc} & \delta_{cc} \end{pmatrix} \\
&= \begin{pmatrix} 1(20) & -94(28) & 105(33) \\ -94(28) & 152(21) & -166(40) \\ 105(33) & -166(40) & 151(21) \end{pmatrix} \text{(ppm)} \\
\overleftrightarrow{\delta}_{A\,in-2} &= \begin{pmatrix} 16(21) & -92(30) & 102(36) \\ -92(30) & 213(23) & -154(40) \\ 102(36) & -154(40) & 149(23) \end{pmatrix} \text{(ppm)} \\
\overleftrightarrow{\delta}_{A\,out-1} &= \begin{pmatrix} 182(32) & -168(45) & 155(53) \\ -168(45) & 343(34) & -189(60) \\ 155(53) & -189(60) & 229(34) \end{pmatrix} \text{(ppm)} \\
\overleftrightarrow{\delta}_{A\,out-2} &= \begin{pmatrix} 276(42) & -230(59) & 208(69) \\ -230(59) & 432(44) & -250(77) \\ 208(60) & -250(77) & 313(45) \end{pmatrix} \text{(ppm)}
\end{aligned}
$$

Ain-1 (Aout-1) is one of the inner (outer) sites in dimer A and Ain-2 (Aout-2) is the other inner (outer) site in dimer A. The tensor of dimer B can be obtained using a unitary operation:

$$
\begin{aligned}
\overleftrightarrow{\delta}_B &= \overleftrightarrow{U}_B \overleftrightarrow{\delta}_A \overleftrightarrow{U}_B^{-1} \\
\overleftrightarrow{U}_B &= \begin{pmatrix} 1 & 0 & 0 \\ 0 & -1 & 0 \\ 0 & 0 & 1 \end{pmatrix}
\end{aligned}
$$

4.2 κ-$(ET)_2Cu_2(CN)_3$

4.2.1 Conductivity

Fig.4.6 shows temperature dependence of resistivity for $E \parallel b$ of both samples. In the pure sample, the behavior was in good agreement with previous reports[17], whereas upturn near the room temperature was suppressed in x=0.05 sample. The conductivities of both samples were fitted by following the nearest neighbor hopping (NNH) and variable-rage hopping (VRH)

Table 4.1: Transport parameters

	Pure sample	x=0.05 sample
Δ (K)	620	276
T_0 (eV)	18.3	0.68
T_c (K)	135	185
d	2	1

equations[17].

$$\sigma(T) \propto \exp(-\Delta/T), \tag{4.1}$$

$$\sigma(T) \propto \exp[(-T_0/T)^{1/(d+1)}], \tag{4.2}$$

where Δ is the activation energy for the NNH model, T_0 is the corresponding activation energy for the VRH model, the d is the dimension of the VRH model, and T_c is the crossover temperature from the NNH model in high temperature region to the VRH model in low temperature region. For the pure sample, the model of $d = 2$ was suitable as shown in Fig.4.7 where the dashed line represents the fitting result by the VRH model and the fitting parameters shown in Table.4.1 were consistent with that in the previous report[15, 17]. For x=0.05 sample, the model of $d = 1$ was suitable rather than that of $d = 2$ as shown in Fig.4.8. Significant difference between the pure and x=0.05 samples was found in the parameter of Δ in the NNH region. Δ of x=0.05 sample is about half of the value of the pure sample, indicating the impurity substitution enhanced conducting behavior and crossover temperature T_c higher than of the pure sample. The VRH fitting in both samples suggested that no intrinsic gap open and the substitution effect was confirmed for transport properties of x=0.05 sample.

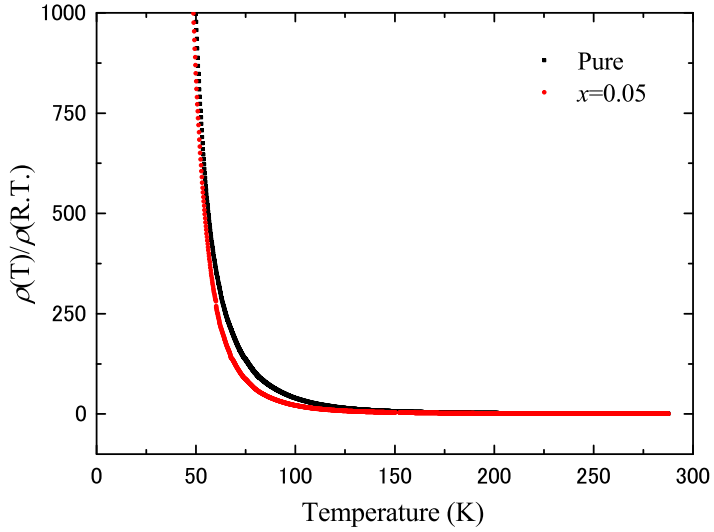

Figure 4.6: Temperature dependence of conductivity normalized with respect to R.T.

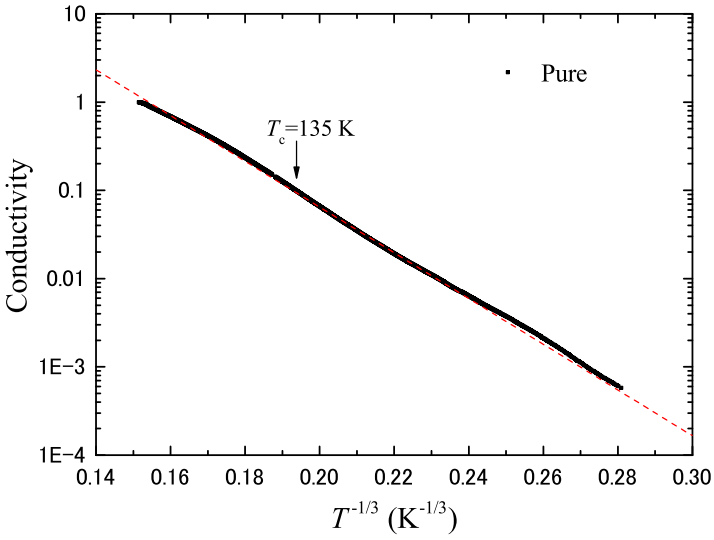

Figure 4.7: Temperature dependence of conductivity normalized with respect to R.T. (pure sample)

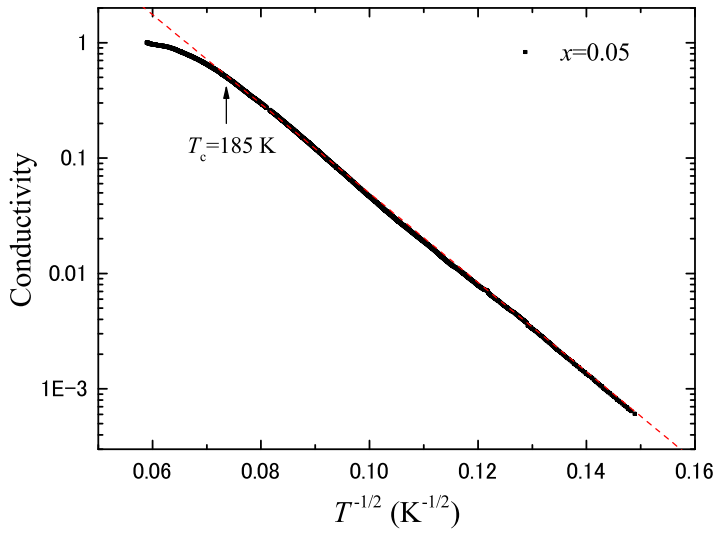

Figure 4.8: Temperature dependence of conductivity normalized with respect to R.T. (x=0.05 sample)

4.2.2 Magnetic susceptibility

Temperature dependence of the static susceptibility of the pure and x=0.05 samples are shown in Fig.4.23 with the results of previous works[11, 15], where the core diamagnetic contribution of -4.37×10^{-4} emu/mol f.u. was already subtracted. The pure sample reproduced the data in previous works[11, 15]. The temperature dependence of x=0.05 sample is quantitatively similar to that of the pure sample with hump structure at around 60 K and rapidly decreases below 20 K. The value of $\chi = 5 \times 10^{-4}$ emu/mol f.u. is lager than $\chi = 4.5 \times 10^{-4}$ emu/mol f.u. of other κ salts. The static susceptibility did not change significantly by the impurity substitution as opposed to the transport measurements.

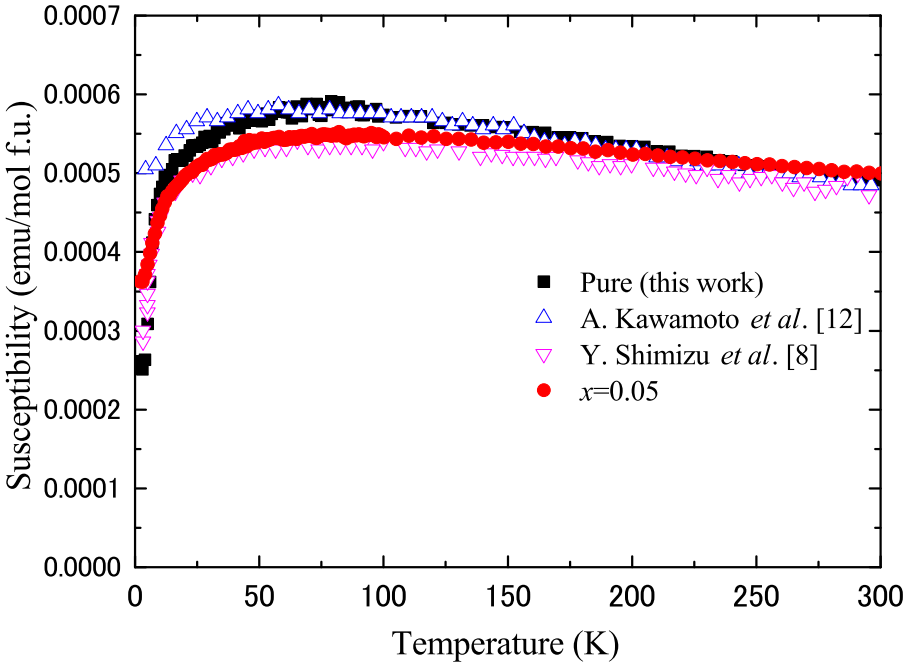

Figure 4.9: Temperature dependence of susceptibility.

4.2.3 NMR Spectra and shift

The NMR is a distinctive microscopic probe for the static and dynamical properties of the electron spins. It enables us to obtain the local spin susceptibility from the Knight shift K, and the magnetic fluctuation from the spin-lattice relaxation rate, T_1^{-1}.

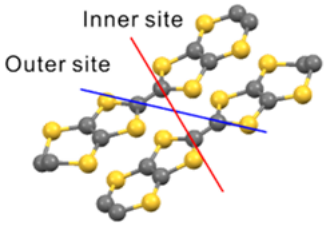

Figure 4.10: Inner and outer sites of ET dimer

The space group of the $(CN)_3$ salt is $P2_1/c$ and a dimer locates on an inversion center. Hence there are two crystallographically independent ^{13}C sites represented as inner and outer sites shown in Fig.4.10. The $(CN)_3$ salt has a single layer structure along c axis, containing two crystallographic equivalent dimers of two crystallographic equivalent molecules in a unit cell as shown in Fig.3.1. Therefore, 2×2=4 resonance lines are expected with an arbitrary orientation of the external field. When the magnetic field is applied perpendicular to the conduction plane, two dimers become magnetically equivalent, two peaks from the inner and outer sites are expected.

Figure4.11 shows the NMR spectra at several temperatures for the magnetic field perpendicular to conduction plane. Left panel shows that of the pure sample and right panel shows that of x=0.05 sample. As mentioned the resonance lines above, two peaks from the inner and outer sites were observed in both samples. In both samples, linewidth broadening was observed at low temperature and no AF ordering was observed as well as in the previous reports for the pure sample[15, 47]. The linewidth broadening of the x=0.05 sample was larger than that of the pure sample.

Figure4.12 shows temperature dependence of the NMR shift. Due to linewidth broadening, we fitted the NMR shift as one peak below 10 K. Both samples showed similar behavior which was proportional to the spin susceptibility. Hence we obtained hyperfine coupling constants from δ-χ plot

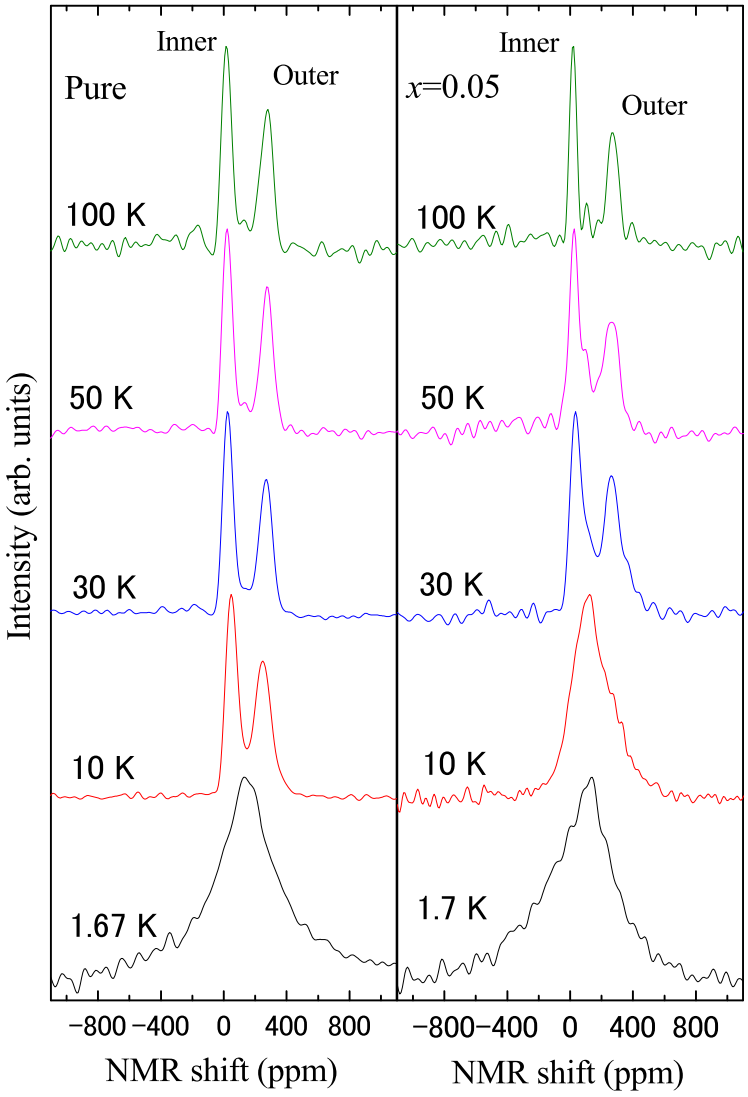

Figure 4.11: Temperature dependence of NMR spectra. Left: the pure sample. Right: x=0.05 sample.

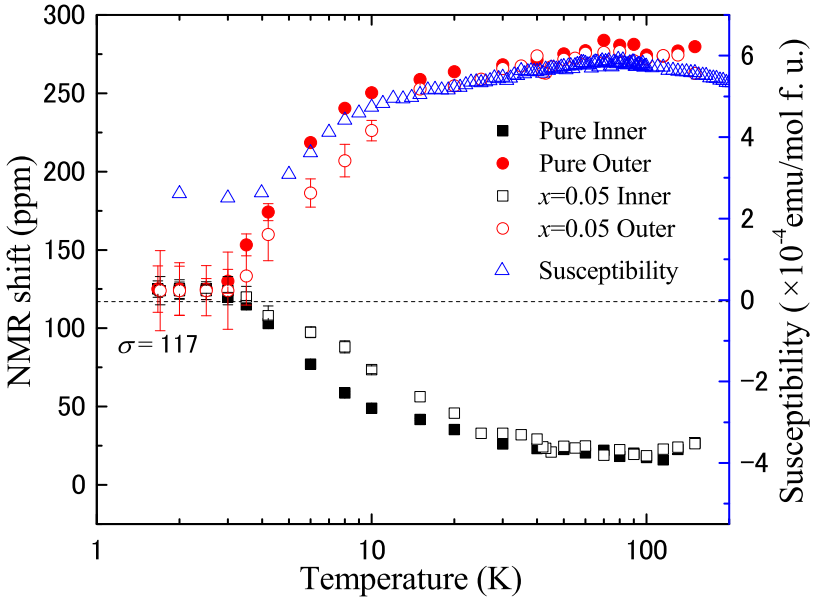

Figure 4.12: Temperature dependence of NMR shift.

shown in Fig.4.13. The hyperfine coupling constants in Table4.2 are almost the same in both samples. The hyperfine coupling constant of inner site is negative and that of outer site is positive as well as other κ salts. With decreasing temperature, the NMR shift gets close to chemical shift of $(ET)^{+0.5}$ which was evaluated from the previous α-$(ET)_2I_3$ work[48]. In the magnetic susceptibility measurement, it is unclear whether finite susceptibility remains at low temperature because of paramagnetic impurities. The NMR shift in this work suggests the local spin susceptibility should vanish at 0 K.

Table 4.2: Hyperfine coupling constants.

	value (kOe/μ_B)
$A_{\parallel a*,\text{pure in}}$	-0.97
$A_{\parallel a*,\text{pure out}}$	1.59
$A_{\parallel a*,\text{x=0.05 in}}$	-0.93
$A_{\parallel a*,\text{x=0.05 out}}$	1.56

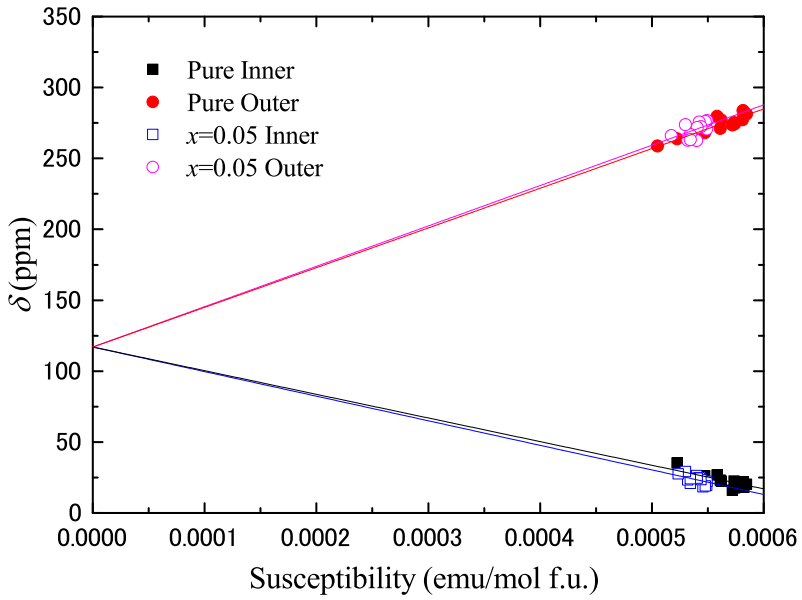

Figure 4.13: δ-χ plot. The chemical shift was evaluated from the previous α-$(ET)_2I_3$ work[48].

4.2.4 Linewidth and spin-spin relaxation rate

Impurity substitution made distinctive effect on the linewidth. Figure4.14 shows the temperature dependence of the full width at half maximum (FWHM) in fields of $H \perp$ conduction plane and the inset shows the temperature dependence of T_2^{-1} for inner and outer peaks of both samples. The FWHM of both samples are almost constant from 150 K down to 1.7 K. On decreasing temperature, the FWHM gradually increases down to 8 K. The FWHM of the outer site which has larger hyperfine coupling constant is broader than that of the inner site as in the previous work[15]. As described in section4.2.3, the line broadening of x=0.05 sample is larger than that of the pure sample. Below 8 K, further broadening is observed in both samples. Contrary to that above 8 K, the FWHM is almost the same in both samples at 1.7 K. In Fourier transform NMR, the linewidth, $\Delta\omega$, of the spectrum is

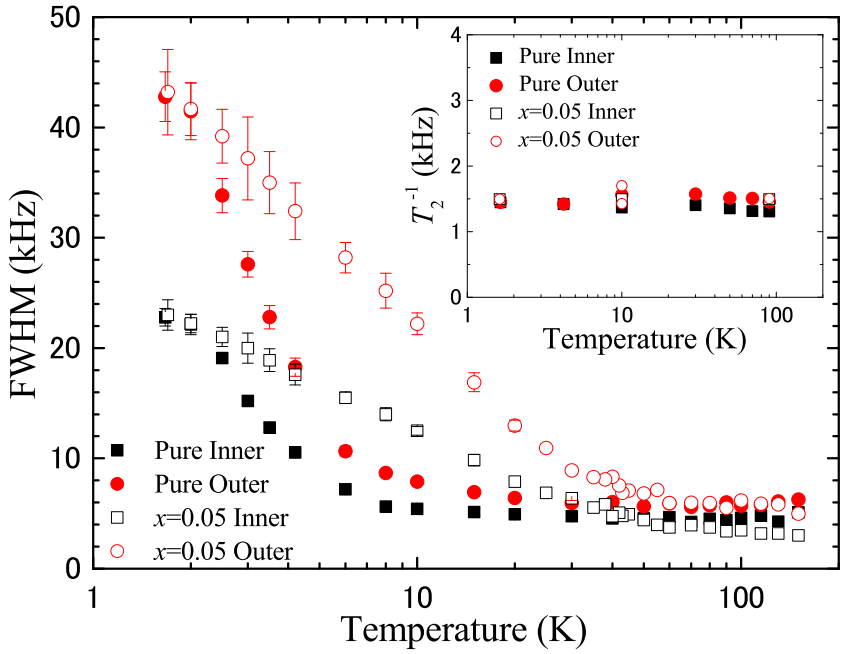

Figure 4.14: Temperature dependence of FWHM. Inset shows temeperature dependende of T_2^{-1}.

generally described as

$$\Delta\omega = \frac{2\pi}{T_2} + \gamma\Delta H, \tag{4.3}$$

where ΔH is the inhomogeneity of the local magnetic field at the corresponding nuclei. The first term is homogeneous width caused by the dynamics and the second term is a static inhomogeneous width caused by the inhomogeneity of the external and the local magnetic field. The measurement of T_2^{-1} differentiate the statics and dynamics. T_2^{-1} can detect slow magnetic fluctuations representing the following equation

$$\frac{1}{T_2} = \frac{1}{2}\int_{-\infty}^{\infty} d\tau H_{\perp}(0)H_{\perp}(\tau)\cos(\omega\tau) + \lim_{\omega\to 0}\int_{-\infty}^{\infty} d\tau H_{\parallel}(0)H_{\parallel}(\tau)\cos(\omega\tau), \tag{4.4}$$

where first term corresponds to T_1^{-1}. Since the value of the second term is much larger than that of T_1^{-1}in the solid-state, T_2^{-1} is described mainly by the second term. For ^{13}C, the time scale of the magnetic fluctuations is from a few $\sim$ 10 kHz.

As shown in the inset of Fig.4.14, the temperature dependence of T_2^{-1} is constant which is about 1.4 kHz from 150 K down to 1.7 K in both samples. Therefore, the increase of the linewidths is due to an enhancement of the static inhomogeneity. In order to evaluate the inhomogeneous width, we subtracted 2.8 kHz of the dynamic part of the linewidth from the FWHM. Figure4.15 shows temperature dependence of the ratio of inhomogeneous width of the outer to inner site. The values are about 2 in both samples and comparable to the ratio of the hyperfine coupling constants obtained from the δ-χ plot.

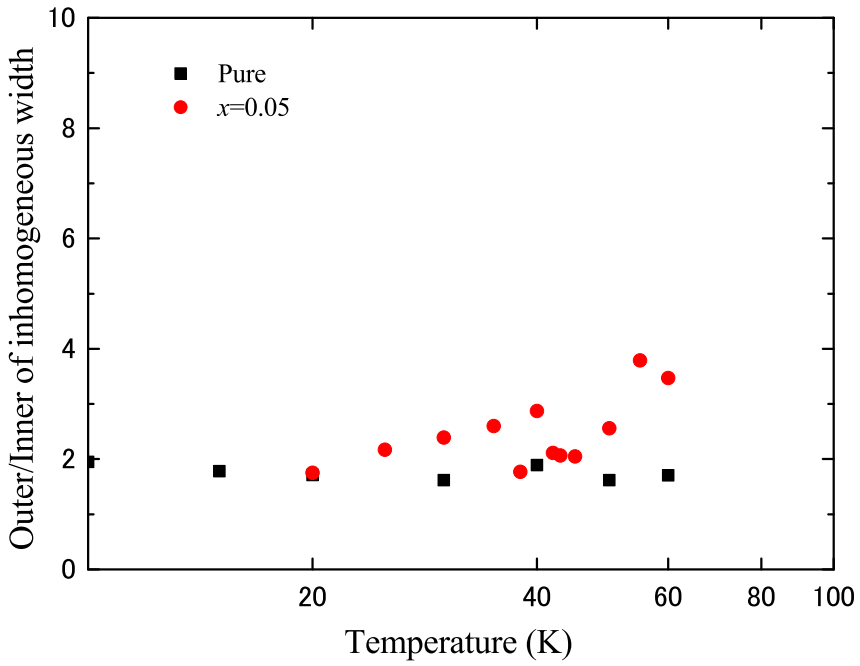

Figure 4.15: Temperature dependence of the ratio of inhomogeneous width of the outer to inner site.

4.2.5 Spin-lattice relaxation rate

We measured the spin-lattice relaxation rate, T_1^{-1}, in order to investigate the impurity substitution effect on the spin dynamics. Figure4.16 shows comparison of the temperature dependence of $(T_1T)^{-1}$ for both samples with the result from the previous report[47] under the same configuration. We evaluated T_1^{-1} from the single exponential curve fitting for the inner and outer sites separately, or the sum of spectrum intensity with the two exponentials model using a ratio, $T_{1,\mathrm{inner}}/T_{1,\mathrm{outer}}$, of 3, which was determined at 100 K. This value is typical of the κ-$(\mathrm{ET})_2X$ salts. The pure sample reproduced the data in the previous work[47]. No significant change between both samples

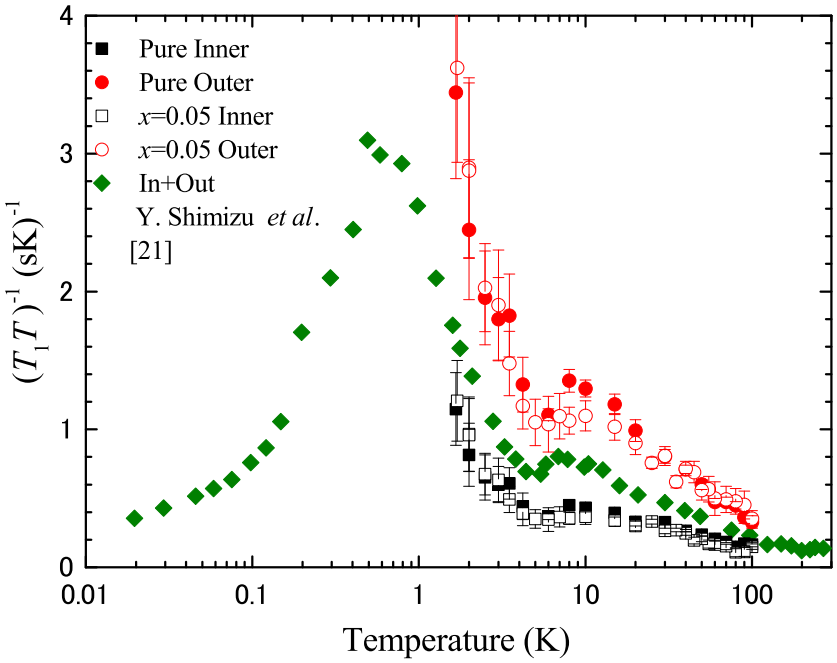

Figure 4.16: Temperature dependence of $(T_1T)^{-1}$.

down to 1.7 K was observed. Considering the results of the static susceptibility, the Knight shift, and $(T_1T)^{-1}$, no significant change of the magnetic properties occurred by the impurity substitution. As lowering temperature, the $(T_1T)^{-1}$ increases and shows a broad peak-like behavior near 8 K. However, it should be noted that recovery curves for both samples deviated from

the exponential fitting below 6 K suggesting distribution of T_1^{-1} as shown in Fig.4.17-4.18 where dashed line represents the model fitting curve. This distribution corresponds to the anomalous broadening below 8 K as mentioned in section 4.2.3.

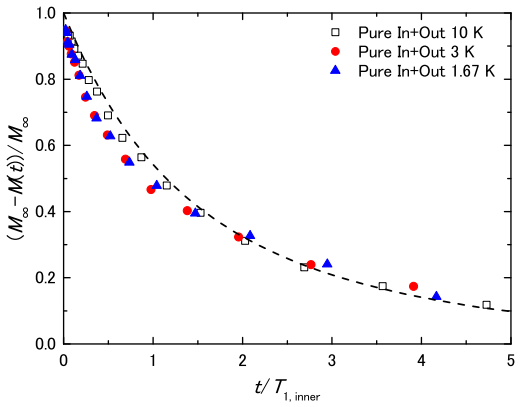

Figure 4.17: Recovery curve of pure sample at several temperatures.

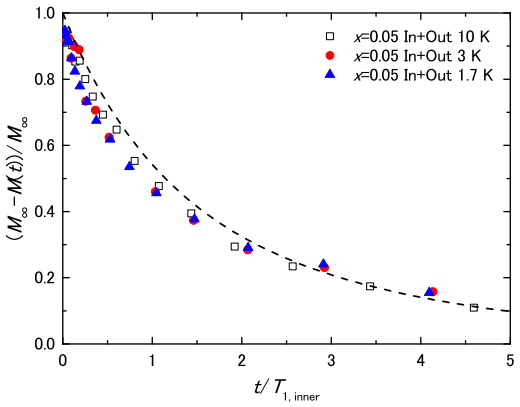

Figure 4.18: Recovery curve of x=0.05 sample at several temperatures.

4.2.6 NMR Spectra and shift of the impurity site

Figure 4.19 shows NMR spectra from impurity sites at several temperatures. Two peaks are observed at 100 K. Linewidth broadening occurs at low temperature and no AF ordering appears. The NMR shift is less than that of the bulk sites. To estimate the local spin susceptibility of the impurity site, hyperfine coupling constant of STF is required. Therefore, we measured mangetic susceptiblity and NMR shift of $x = 1$ sample, so that we could obtain its hyperfine coupling constant for the same direction by $\delta - \chi$ plot. Figure 4.20 shows $\delta - \chi$ plot for $x = 1$ sample and the plots gives the hyperfine coupling constants $A_{\|a^*,x=1\,\text{in}}$ =-1.05 kOe/μ_B and $A_{\|a^*,x=1\,\text{out}}$ =1.48 μ_B/kOe, and $\sigma = 110$ ppm. The hyperfine coupling constants of $x = 1$ sample are very close to that of pure sample, indicating the local spin susceptibility becomes small comapared with pure sample. Also the chemical shift of STF is comparable to that of ET, indicating their chemical environments around ^{13}C is almost the same. To compare spin susceptibility between ET and STF sites without chemical shift term, we used the following equation $\Delta\delta = \delta_{\text{out}} - \delta_{\text{in}} = \Delta A \chi_{\text{spin}}$ (see Eq. 3). The local spin susceptibility at a STF

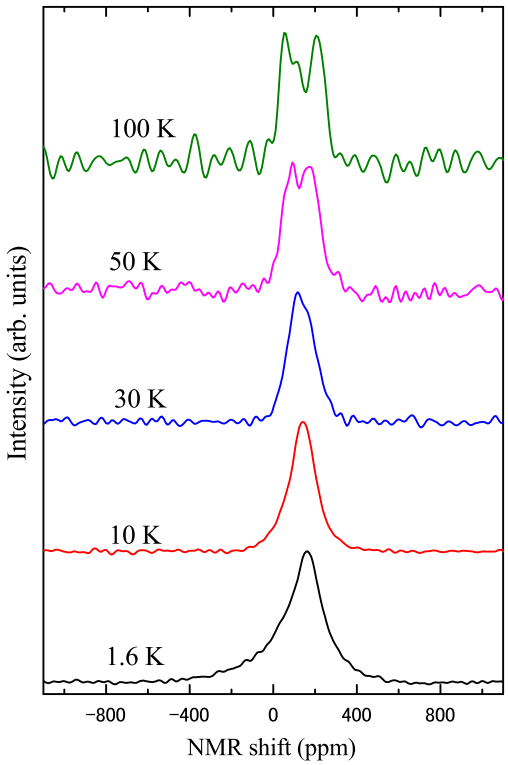

Figure 4.19: NMR spectra at several temperature of impurity sites.

site, $\chi_{\rm imp}$, was estimated 60% of that at a ET site, $\chi_{\rm bulk}$, at 100 K where the NMR peak separation is clear. This reduction of the local spin susceptibility reveals the STF substitution can affcet the electronic state experimentally.

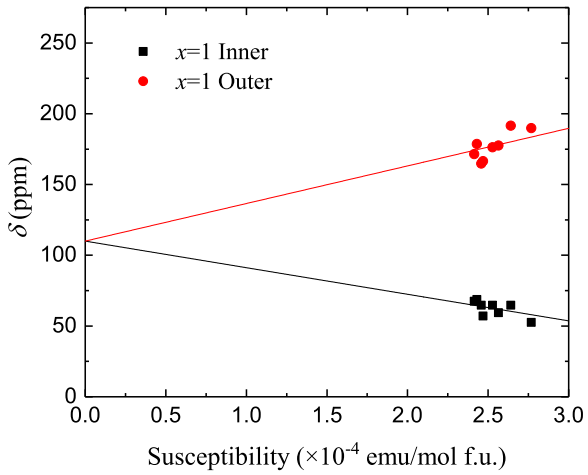

Figure 4.20: Temperature dependence of $\delta-\chi$ plot for $x = 1$ sample.

Figure 4.21 shows the temperature dependence of FWHM of the NMR lines from impurity sites as a function of temperature. The FWHM of the NMR line of the impurity site at low temperature is less than that of bulk sites. The ratio of inhomogeneous linewidth $\nu_{\rm imp}/\nu_{\rm bulk}$ is about 0.5, which is consistent with $\chi_{\rm imp} \simeq 0.6\chi_{\rm bulk}$. Therefore, $\Delta\chi/\chi$ at the bulk and impurity sites are much the same since $\nu \propto \Delta\chi$.

4.2.7 $(T_1T)^{-1}$ of the impurity site

Figure 4.22 shows $(T_1T)^{-1}$ for the bulk and $(T_1T)^{-1}$ scaled for the impurity sites, both as functions of temperature. Each curve is the mean value of the associated inner and outer sites. The temperature dependence of $(T_1T)^{-1}$ for impurity sites is similar to that for bulk sites. We also observed recovery curves deviated from the exponential fits below 8 K, which suggested distribution of T_1^{-1}. Scaling $(T_1T)^{-1}$ for impurity sites by a factor of two matches well with the results for $(T_1T)^{-1}$ for the bulk sites.

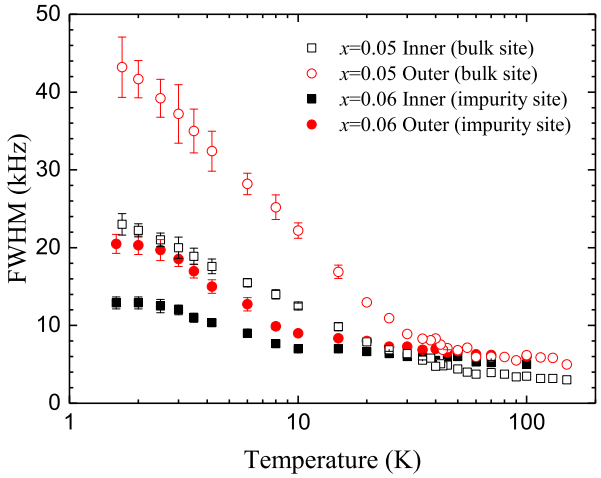

Figure 4.21: FWHM of NMR line for impurity and bulk sites as a function of temperature.

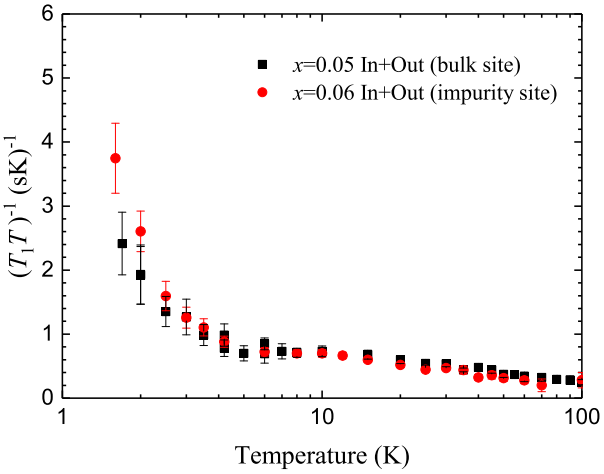

Figure 4.22: Temperature dependence of $(T_1T)^{-1}$ of mean value for impurity and bulk sites. Each plot is the mean value of the associated inner and outer sites. $(T_1T)^{-1}$ for the impurity site is scaled by a factor of two.

4.3 λ-$(ET)_2GaCl_4$

4.3.1 Magnetic susceptibility

Figure 4.23 shows temperature dependence of the magnetic susceptibility χ for powder samples of λ-$(ET)_2GaCl_4$. The core diamagnetic contribution of 4.67×10^{-4} emu/mol f.u. was already subtracted. The χ at room temperature is 7 emu/mol which is greater than 4.4 emu/mol of κ-$(ET)_2X$ salts [49], suggesting the electronic state of λ-$(ET)_2GaCl_4$ is more localized than that of κ-type salts. The χ increases with decreasing temperature and shows a broad hump structure which originates from the low dimensional magnetic interaction network. Solid line is fit by using two-dimensional $S = 1/2$ square lattice Heisenberg AF model [50] with exchange interaction $J/k_B = 98$ K as shown by red curve in Fig. 4.23. The Curie constant C was estimated to be 0.45 emu·K/mol, indicating the effective magnetic spin moment (μ_{eff}) is about 1.1 μ_B, which is similar to that of organic Mott insulator β'-$(ET)_2ICl_2$ whose moment is 1 μ_B per dimer [51]. Below 13 K, the χ shows upturn.

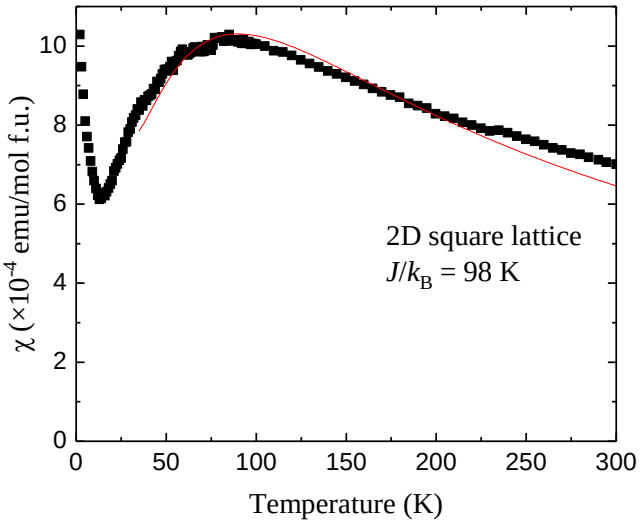

Figure 4.23: Magnetic susceptibility as a function of temperature for λ-$(ET)_2GaCl_4$. Solid curve represents the result of two-dimensional $S = 1/2$ square lattice Heisenberg AF model with J/k_B=98 K.

4.3.2 NMR Spectra

Figure 4.24(a) shows the temperature dependence of the ^{13}C NMR spectrum from 100 K to 4.2 K under the magnetic field of 7 T applied to [110] direction. In λ-$(ET)_2GaCl_4$, there are two crystallographically non-equivalent ET molecules in a unit cell, and each molecule has two non-equivalent ^{13}C sites. Therefore, four independent peaks are expected. As confirmed in Fig. 4.24(a), a broad peak with fine structure is observed at 100 K, indicating the four peaks are merged into the broad peak due to almost the same hyperfine coupling constant. Above 20 K, the NMR peak shows no significant temperature dependence. However, the broad peak splits into 5 discrete peaks below 13 K and the peak splitting is enhanced as temperature decreases, indicating emergence of local field due to AF ordering.

The nuclear spin-lattice relaxation rate $1/T_1$ probes spin fluctuation, which is written as

$$\frac{1}{T_1} \propto \sum_q \left(A_q A_{-q}\right) \frac{\chi''_q(\omega)}{\omega}. \tag{4.5}$$

Here, A and $\chi''_q(\omega)$ are the hyperfine coupling constant between an electron and a nucleus, and the imaginary part of the dynamic susceptibility at wave vector q, respectively. ω is the nuclear Larmor frequency. Figure 4.24(b) shows the temperature dependence of $1/T_1$. The $1/T_1$ is constant in the temperature range between 100 K and 20 K as expected in a localized spin system well above Néel temperature of T_N. The $1/T_1$ increases drastically below 20 K due to the critical slowing down and diverges around 13 K, which coincides with the temperatures where the anomaly in the magnetic susceptibility and the NMR peak splitting are observed. Below 13 K, the temperature dependences of $1/T_1$ of both peak 1 and peak 2 indicated by blue inverted triangle and red circle, respectively in Fig. 4.24(a) show thermal activation behavior.

4.4 λ-$(STF)_2GaCl_4$

4.4.1 NMR spcetra, linewidth and line shift

Figure 4.25 shows NMR spectra at several temperatures under a magnetic field parallel to [110]. A broad peak with a fine structure because of

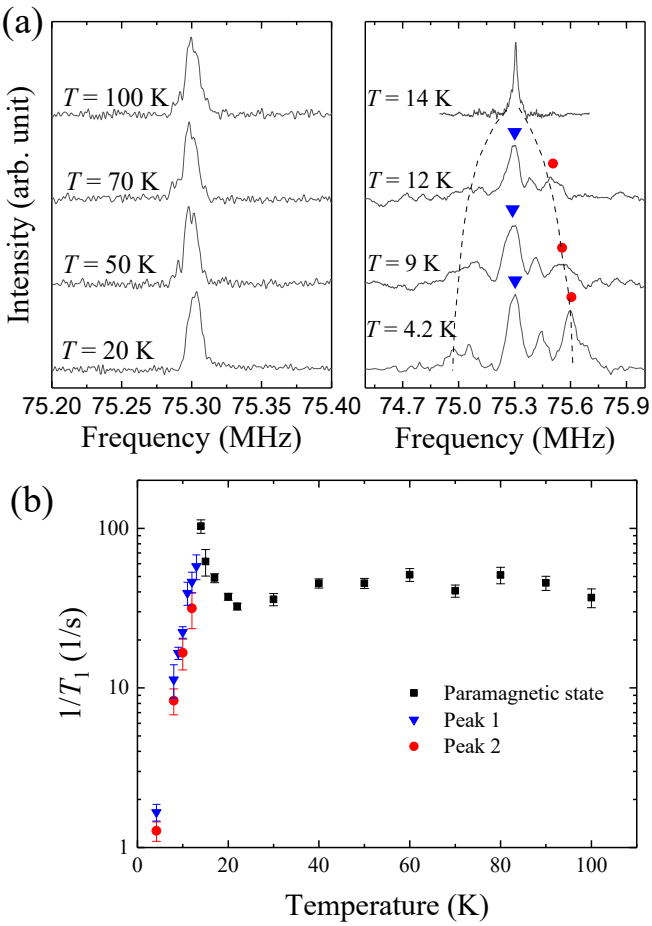

Figure 4.24: (a) ^{13}C NMR spectra at several temperature. The dashed lines are a guide to the eye. (b) $1/T_1$ as a function of temperature. Peak 1 and peak 2 represent blue inverted triangle and red circle in the NMR spectra, respectively.

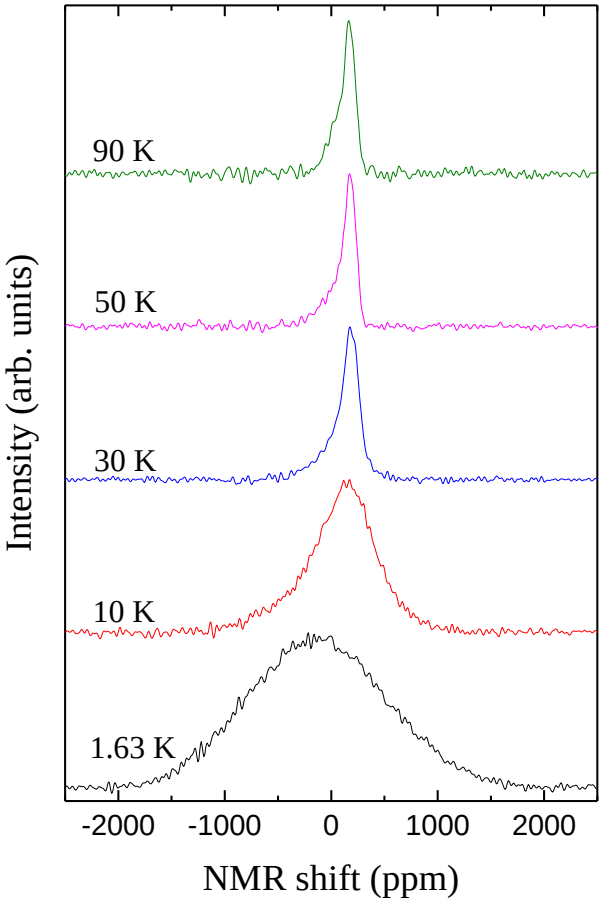

Figure 4.25: NMR spectra at several temperatures for a magnetic field applied to [110].

superposition of independent peaks is observed at 90 K as well as well as λ-STF salt. With decreasing temperature, the spectrum broadens, however, no peak spliting occurs down to 1.63 K.

Figure 4.26 shows temperature dependence of the FWHM of the NMR lines and the inset shows the temperature dependence of T_2^{-1}. The NMR linewidth broadens below 40 K, whereas T_2^{-1} remains constant at all temperatures, indicating that the broadening is originated not from dynamics but from inhomogeneous broadening (see Eq.4.3).

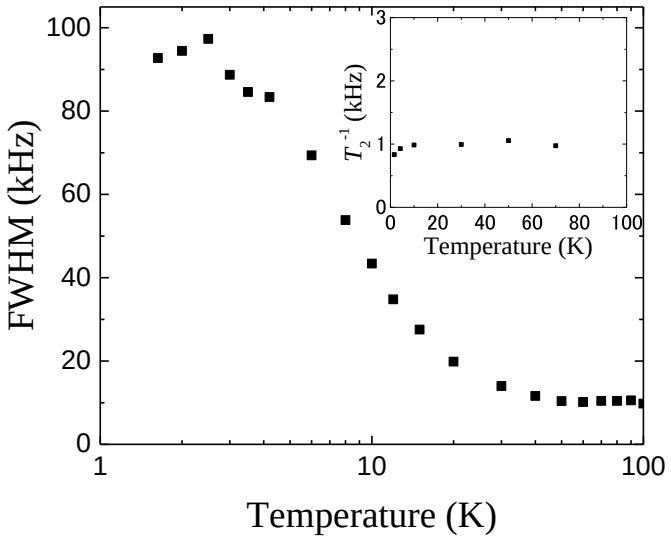

Figure 4.26: Temperature dependence of FWHM. The inset shows T_2^{-1}.

Figure 4.27 shows temperature dependence of NMR shift. From 100 K down to 20 K, NMR shift does not change much, indicating the hyperfine coupling constant is small, wheareas a steep decrease of the shift is observed below 15 K.

4.4.2 Spin-lattice relaxation rate

Figure 4.28 shows temperature dependence of $1/T_1$ with fitting of $\beta = 0.78$. $1/T_1$ was evaluated from the single-stretched-exponential recovery, $1 - M(t)/M_0 = \exp[1-(t/T_1)^{\beta}]$ where $M(t)$ is the nuclear magnetization and M_0 is a saturated value of $M(t)$, because the central peak consists of multiple peaks whose chemical environments are slightly different from each other.

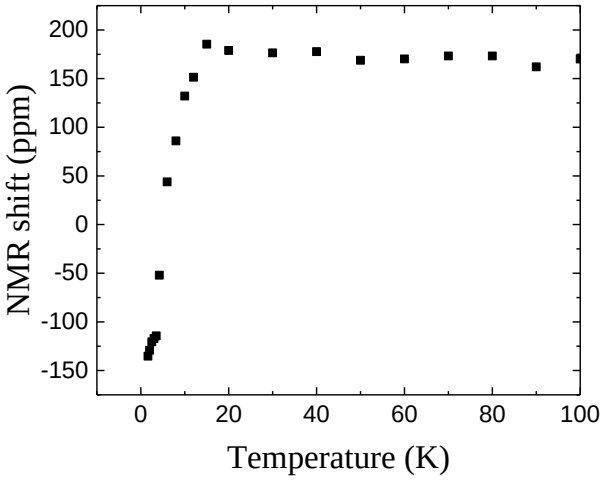

Figure 4.27: Temperature dependence of NMR shift. The inset shows T_2^{-1}.

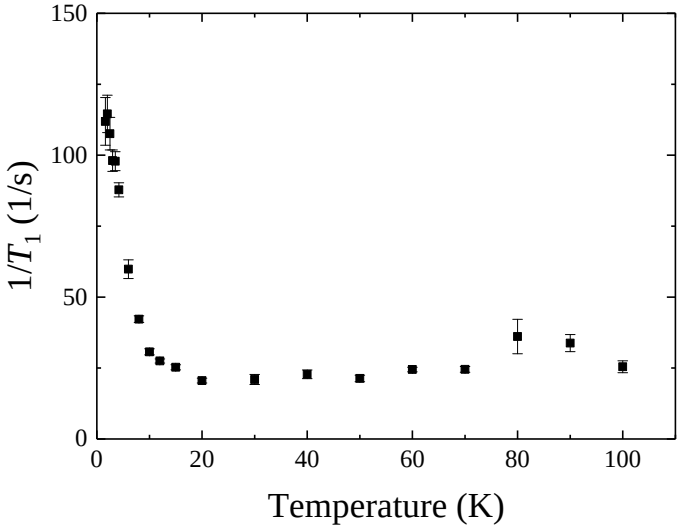

Figure 4.28: Temperature dependence of $1/T_1$ for λ-STF salt.

$1/T_1$ is constant down to 20 K and exhibts an increase below 20 K as well as λ-ET salt, and there was no divergence peak like λ-ET salt.

Figure 4.29 shows relaxation curves of nuclear magnetization $M(t)$ at 90, 20 and 2 K. The dashed line represents fit, $1-M(t)/M_0 = \exp[1-(t/T_1)^{0.78}]$. The recovery was well discribed with $\beta = 0.78$ above 20 K, however, deviation occurs below 20 K, suggesting the distribution of $1/T_1$ developed below 20 K and the inhomogeneous at low temperature.

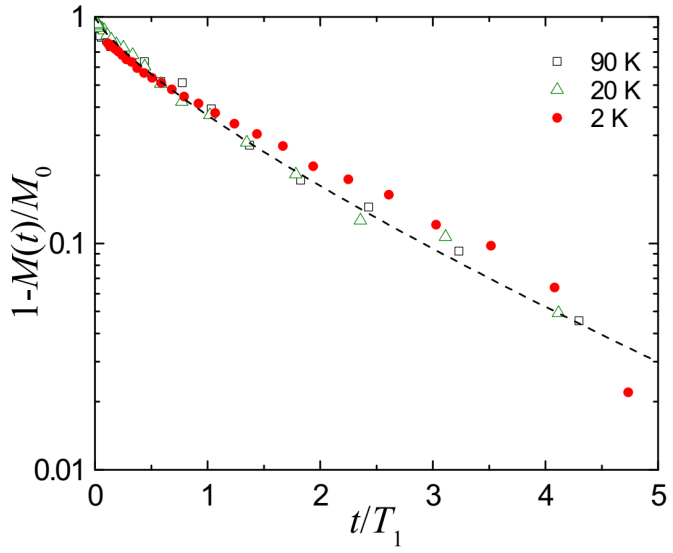

Figure 4.29: Profile of relaxation curves of the nuclear magnetization at serveral temeperatures. The dashed line represents fitting with $\beta = 0.78$.

Figure 4.30 shows temperature dependence of $(T_1T)^{-1}$. $(T_1T)^{-1}$ could be fit by Curie-Weiss law with values $C = 19.3 \pm 0.7$ and $\Theta = 4.1 \pm 0.1$. The increase of $(T_1T)^{-1}$ indicates the development of AF spin fluctuation.

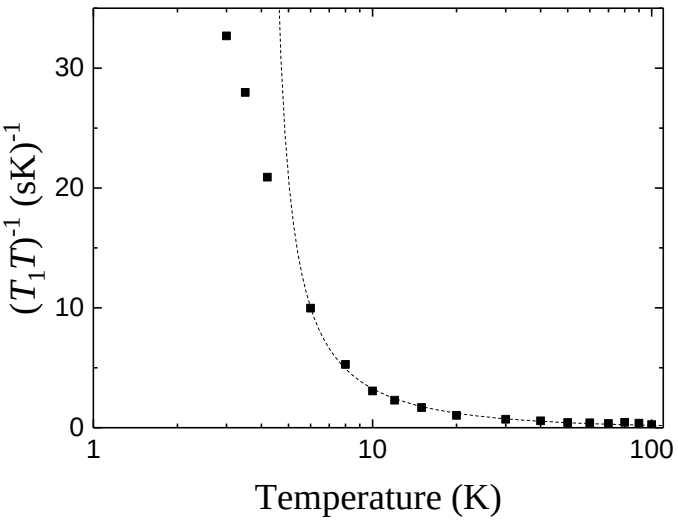

Figure 4.30: Temperature dependence of $(T_1T)^{-1}$ for λ-STF salt. The solid line represents Curie-Weiss fit.

Chapter 5

Discussion

5.1 κ-$(ET)_2X$ (X=Cu[N(CN)$_2$Br, Cu(NCS)$_2$)

5.1.1 Hyperfine coupling tensor

The NMR shift can be expressed from the Knight shift (K), the chemical shift (σ), and the spin susceptibility (χ_s), using the equation $\delta = K + \sigma = A\chi_s + \sigma$. The hyperfine coupling tensor A and the chemical shift tensor σ can be determined using the equations, $A = \vec{h}^T \overleftrightarrow{A} \vec{h}$, $\sigma = \vec{h}^T \overleftrightarrow{\sigma} \vec{h}$, respectively. Here, A is the hyperfine coupling constant between the nuclear and electron spins and $\vec{h}$ is the cosine of the direction of the external field. As the chemical shift is caused by the orbital motion of the electron charge near the nuclei, the chemical shift depends mainly on the molecular structure and the chemical shifts of the inner and outer sites are the same. The chemical shift also has anisotropy due to the planar molecular structure and depends on the charge of the molecule. This requires the chemical shift tensor of the $+0.5e$ charge state, which was estimated from the ^{13}C-NMR of nonmagnetic α-$(ET)_2I_3$ to be a diagonalized $\overleftrightarrow{\sigma_m} = (\sigma_{xx}, \sigma_{yy}, \sigma_{zz}) = (115.6, 175.1, 55.4)$(ppm) for the molecular coordinates shown in Fig.3.1 [48]. The chemical shift in the orthogonal crystal coordinate system, $\overleftrightarrow{\sigma_c}$, can be obtained by a basis transformation from molecular to orthogonal crystal system using the unitary

operation as follows:

$$\sigma_c = \overleftrightarrow{U}\overleftrightarrow{\sigma_m}\overleftrightarrow{U}^{-1},$$

$$\overleftrightarrow{U}^{-1} = \begin{pmatrix} \vec{x}_m \cdot \vec{x}_a & \vec{x}_m \cdot \vec{x}_b & \vec{x}_m \cdot \vec{x}_c \\ \vec{y}_m \cdot \vec{x}_a & \vec{y}_m \cdot \vec{x}_b & \vec{y}_m \cdot \vec{x}_c \\ \vec{z}_m \cdot \vec{x}_a & \vec{z}_m \cdot \vec{x}_b & \vec{z}_m \cdot \vec{x}_c \end{pmatrix},$$

where $\vec{x}_m$, $\vec{y}_m$, $\vec{z}_m$ are unit vectors in molecular coordinate system shown in Fig. 3.1 and $\vec{x}_a$, $\vec{y}_b$, $\vec{z}_c$ are are those in the orthogonal crystal coordinate system. Thus, the chemical shift in the crystal coordinate system can be obtained for dimer A of κ-Br can be calculated as:

$$\begin{aligned} \overleftrightarrow{\sigma_c} &= \begin{pmatrix} \sigma_{aa} & \sigma_{ab} & \sigma_{ac} \\ \sigma_{ab} & \sigma_{bb} & \sigma_{bc} \\ \sigma_{ac} & \sigma_{bc} & \sigma_{cc} \end{pmatrix} \\ &= \begin{pmatrix} 112.9 & -0.4 & -48.8 \\ -0.4 & 116.3 & -34.6 \\ -48.8 & -34.6 & 117.0 \end{pmatrix} \text{(ppm)} \end{aligned}$$

and for dimer A of κ-NCS as:

$$\begin{aligned} \overleftrightarrow{\sigma_c} &= \begin{pmatrix} \sigma_{a^*a^*} & \sigma_{a^*b} & \sigma_{a^*c} \\ \sigma_{a^*b} & \sigma_{bb} & \sigma_{bc} \\ \sigma_{a^*c} & \sigma_{bc} & \sigma_{cc} \end{pmatrix} \\ &= \begin{pmatrix} 97.6 & 39.4 & -9.3 \\ 39.4 & 134.0 & 40.1 \\ -9.3 & 40.1 & 114.6 \end{pmatrix} \text{(ppm)} \end{aligned}$$

As the spin susceptibility is almost isotropic [52], the anisotropy of the NMR shift is due to the anisotropy of the hyperfine coupling constant. The hyperfine coupling tensor for the dimer unit of κ-Br can be determined using the NMR shift, the chemical shift tensors and the spin susceptibility as:

$$\begin{aligned} \overleftrightarrow{A_{in}} &= \begin{pmatrix} A_{aa} & A_{ab} & A_{ac} \\ A_{ab} & A_{bb} & A_{bc} \\ A_{ac} & A_{bc} & A_{cc} \end{pmatrix} \\ &= \begin{pmatrix} 0.7(4) & 1.1(4) & 2.8(6) \\ 1.1(4) & -1.3(2) & 1.5(4) \\ 2.8(6) & 1.5(4) & 1.4(3) \end{pmatrix} \text{(kOe/}\mu_B\text{)} \\ \overleftrightarrow{A_{out}} &= \begin{pmatrix} 2.4(0.7) & 2.1(7) & 4(1) \\ 2.1(7) & 1.3(4) & 2.9(7) \\ 4(1) & 2.9(7) & 4.0(5) \end{pmatrix} \text{(kOe/}\mu_B\text{)} \end{aligned}$$

and for the dimer unit of κ-NCS as:

$$\overleftrightarrow{A}_{in-1} = \begin{pmatrix} A_{aa^*} & A_{a^*b} & A_{a^*c} \\ A_{a^*b} & A_{bb} & A_{bc} \\ A_{a^*c} & A_{bc} & A_{cc} \end{pmatrix}$$

$$= \begin{pmatrix} -1.2(2) & -1.7(3) & 1.5(4) \\ -1.7(3) & 0.2(2) & -2.6(4) \\ 1.5(4) & -2.6(4) & 0.5(2) \end{pmatrix} (\mathrm{kOe}/\mu_B)$$

$$\overleftrightarrow{A}_{out-1} = \begin{pmatrix} 1.1(4) & -2.6(5) & 2.1(6) \\ -2.6(5) & 2.7(4) & -2.9(7) \\ 2.1(6) & -2.9(7) & 1.5(4) \end{pmatrix} (\mathrm{kOe}/\mu_B)$$

$$\overleftrightarrow{A}_{in-2} = \begin{pmatrix} -1.0(2) & -1.7(3) & 1.4(4) \\ -1.7(3) & 1.0(2) & -2.5(5) \\ 1.4(4) & -2.5(4) & 0.4(2) \end{pmatrix} (\mathrm{kOe}/\mu_B)$$

$$\overleftrightarrow{A}_{out-2} = \begin{pmatrix} 2.3(5) & -3.4(7) & 2.8(8) \\ -3.4(7) & 3.8(5) & -3.7(9) \\ 2.8(8) & -3.7(9) & 2.5(5) \end{pmatrix} (\mathrm{kOe}/\mu_B)$$

To assess the properties of the hyperfine coupling tensor, the tensor can be expressed using the molecular coordinates shown in Fig.3.1 and the isotropic and anisotropic parts can be separated for κ-Br as:

$$\begin{aligned} \overleftrightarrow{A_{in}} &= \begin{pmatrix} -1.7(3) & 0.1(4) & 0.5(4) \\ 0.1(4) & -1.9(4) & -0.3(4) \\ 0.5(4) & -0.3(4) & 4.4(4) \end{pmatrix} \\ &= \begin{pmatrix} 0.27 & 0 & 0 \\ 0 & 0.27 & 0 \\ 0 & 0 & 0.27 \end{pmatrix} \\ &+ \begin{pmatrix} -1.97 & 0.1 & 0.5 \\ 0.1 & -2.17 & -0.3 \\ 0.5 & -0.3 & 4.13 \end{pmatrix} (\mathrm{kOe}/\mu_B) \\ \overleftrightarrow{A_{out}} &= \begin{pmatrix} -0.3(6) & 0.1(8) & -0.6(8) \\ 0.1(8) & -0.5(8) & -0.1(8) \\ -0.6(8) & -0.1(8) & 8.6(8) \end{pmatrix} \\ &= \begin{pmatrix} 2.6 & 0 & 0 \\ 0 & 2.6 & 0 \\ 0 & 0 & 2.6 \end{pmatrix} \end{aligned}$$

$$+ \quad \begin{pmatrix} -2.9 & 0.1 & -0.6 \\ 0.1 & -3.1 & -0.1 \\ -0.6 & -0.1 & 6.0 \end{pmatrix} (\mathrm{kOe}/\mu_B)$$

and for κ-NCS as:

$$\overleftrightarrow{A}_{in-1} = \begin{pmatrix} -2.1(3) & 0.1(3) & 0.4(3) \\ 0.1(3) & -2.4(3) & 0.2(3) \\ 0.4(3) & 0.2(3) & 4.0(3) \end{pmatrix}$$

$$= \begin{pmatrix} -0.17 & 0 & 0 \\ 0 & -0.17 & 0 \\ 0 & 0 & -0.17 \end{pmatrix}$$

$$+ \begin{pmatrix} -1.93 & 0.1 & 0.4 \\ 0.1 & -2.23 & 0.2 \\ 0.4 & 0.2 & 4.17 \end{pmatrix} (\mathrm{kOe}/\mu_B)$$

$$\overleftrightarrow{A}_{out-1} = \begin{pmatrix} -0.8(5) & 0.0(6) & -0.7(6) \\ 0.0(6) & -1.0(6) & 0.0(6) \\ -0.7(6) & 0.0(6) & 6.9(6) \end{pmatrix}$$

$$= \begin{pmatrix} 1.7 & 0 & 0 \\ 0 & 1.7 & 0 \\ 0 & 0 & 1.7 \end{pmatrix}$$

$$+ \begin{pmatrix} -2.5 & 0.0 & -0.7 \\ 0.0 & -2.7 & 0.0 \\ -0.7 & 0.0 & 5.2 \end{pmatrix} (\mathrm{kOe}/\mu_B)$$

$$\overleftrightarrow{A}_{in-2} = \begin{pmatrix} -1.9(3) & 0.1(4) & 0.3(4) \\ 0.1(4) & -1.9(4) & -0.1(4) \\ 0.3(4) & -0.1(4) & 4.2(4) \end{pmatrix}$$

$$= \begin{pmatrix} 0.13 & 0 & 0 \\ 0 & 0.13 & 0 \\ 0 & 0 & 0.13 \end{pmatrix}$$

$$+ \begin{pmatrix} -2.03 & 0.1 & 0.3 \\ 0.1 & -2.03 & -0.1 \\ 0.3 & -0.1 & 4.07 \end{pmatrix} (\mathrm{kOe}/\mu_B)$$

$$
\overleftrightarrow{A}_{out-2} = \begin{pmatrix} -0.3(7) & -0.1(7) & -1.0(7) \\ -0.1(7) & -0.6(7) & 0.3(7) \\ -1.0(7) & 0.3(7) & 9.4(7) \end{pmatrix}
$$

$$
= \begin{pmatrix} 2.83 & 0 & 0 \\ 0 & 2.83 & 0 \\ 0 & 0 & 2.83 \end{pmatrix}
$$

$$
+ \begin{pmatrix} -3.13 & -0.1 & -1.0 \\ -0.1 & -3.43 & 0.3 \\ -1.0 & 0.3 & 6.56 \end{pmatrix} (\mathrm{kOe}/\mu_B)
$$

The tilt angle of the principal axis of the tensor A_{zz} can be calculated from the direction of the p_z orbital shown in Fig.5.1. In κ-Br, θ is 5.4° for inner sites and 3.6° for outer sites, with θ at the inner sites in good agreement with previous findings [53]. In κ-NCS, θ is 4.3° for inner site-1, 2.8° for outer site-1, 4.8° for inner site-2, and 6.2° for outer site-2. The tilt from the principal axes is considered to be caused by a displacement along the molecular long axis. The inter-plane distances in a dimers of κ-Br and of κ-NCS were found to be 3.45 Åand 3.53 Å, respectively. As the overlap modes of these salts were almost the same, almost the same tensors were expected, but they were found to differ. We first focused on the differences between inner and outer sites. The anisotropic parts caused by the p_z orbital have uniaxial symmetry, with almost the diagonal configuration relative to molecular coordinates. The amplitude of the anisotropic terms could be explained mainly by the dipole field of the p_z orbital on the ^{13}C sites. The isotropic parts of the inner and outer sites differed markedly. The difference between inner and outer sites was mainly due to the isotropic part. The inner sites in a dimer couple are directly due to their p_z orbitals. The direct coupling results in an antiferromagnetic interaction and a negative exchange field, reducing the isotropic term of the inner sites.

Next, we compared the tensors with those of the β'-ICl_2 salt. β'-ICl_2 has a dimer based structure with a different dimer arrangement. The manner of overlap, with an interplane distance of 3.48 Å, was almost the same as that in κ-salts. The hyperfine coupling tensor in β'-ICl_2 was calculated as

described [54]:

$$\overleftrightarrow{A}_{in} = \begin{pmatrix} -1.41 & 0.40 & -0.07 \\ 0.40 & -0.91 & 1.45 \\ -0.07 & 1.45 & 3.17 \end{pmatrix}$$
$$= \begin{pmatrix} 0.28 & 0 & 0 \\ 0 & 0.28 & 0 \\ 0 & 0 & 0.28 \end{pmatrix}$$
$$+ \begin{pmatrix} -1.69 & 0.40 & -0.07 \\ 0.40 & -1.19 & 1.45 \\ -0.07 & 1.45 & 2.89 \end{pmatrix} (\mathrm{kOe}/\mu_B)$$
$$\overleftrightarrow{A}_{out} = \begin{pmatrix} -0.40 & 0.09 & -1.70 \\ 0.09 & -0.36 & 1.48 \\ -1.70 & 1.48 & 6.62 \end{pmatrix}$$

$$= \begin{pmatrix} 1.95 & 0 & 0 \\ 0 & 1.95 & 0 \\ 0 & 0 & 1.95 \end{pmatrix}$$
$$+ \begin{pmatrix} -2.35 & 0.09 & -1.7 \\ 0.09 & -2.31 & 1.48 \\ -1.7 & 1.48 & 4.67 \end{pmatrix} (\mathrm{kOe}/\mu_B)$$

In β'-ICl_2, θ was 17.8° for inner sites and 16.2° for outer sites. Almost the same dimer structure suggested that the Knight shift tensor should be almost the same. However, their tensors differed from those in κ-salts, especially the tilt angles of the principal axes. The local magnetic field on a ^{13}C site, $\vec{h}_{\mathrm{local}}$, can be calculated based on the contributions of the spin magnetizations on a dimer through $\overleftrightarrow{A_0}$ and on neighboring dimers through $\overleftrightarrow{B_i}$, as shown in Fig.5.2:

$$\vec{h}_{\mathrm{local}} = \overleftrightarrow{A_0}\vec{M}_0 + \sum_i \overleftrightarrow{B_i}\vec{M}_i$$

where $\vec{M}_0$ and $\vec{M}_i$ are the on-site and off-site spin magnetizations, respectively. As $\vec{M}_0 = \vec{M}_i = \vec{M}$ in the paramagnetic state,

$$\vec{h}_{\mathrm{local}} = (\overleftrightarrow{A_0} + \sum_i \overleftrightarrow{B_i})\vec{M},$$
$$\delta = (\overleftrightarrow{A_0} + \sum_i \overleftrightarrow{B_i})\chi$$

Here $(\overleftrightarrow{A_0}+\sum_i \overleftrightarrow{B_i})$ is the experimentally estimated hyperfine coupling tensor. This hyperfine coupling tensor includes the contributions of both on-site and off-site dimers. The large tilt angle of β'-ICl_2 suggests that the anisotropic part of $\overleftrightarrow{B_i}$ of the neighboring dimer contribution should be considered because the manners of stacking differ for the κ and β' salts (Fig.5.2). The hyperfine coupling tensors of these compounds are highly dependent on their crystal structure and dimer arrangement. Our results suggest that it is not appropriate to use the same tensors for different crystal systems, even when their bases are the same.

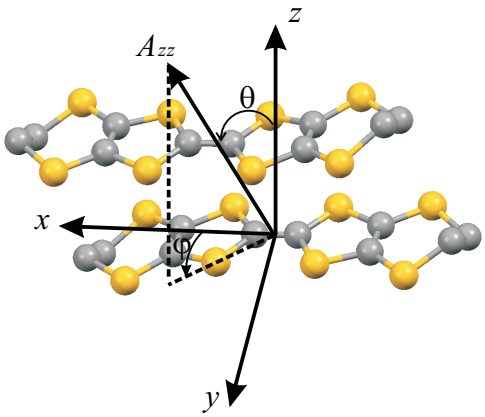

Figure 5.1: Molecular coordinates of the ET molecule and principal axes of the hyperfine tensor.

5.1.2 Korringa factors of superconducting κ-salts

The pressure dependence of cyclotron mass m_c^* and superconducting transition point T_c suggested a correlation between m_c^* and T_c [9] as shown in Fig.5.3. Antiferromagnetic electron correlation may therefore play an important role in the superconductivity of κ-salts. The Korringa factor $\mathcal{K}(\alpha)$ describing electron correlations is satisfied:

$$T_1 T K_s^2 = F\mathcal{K}(\alpha)^{-1} \frac{\hbar}{4\pi k_B} \left(\frac{\gamma_e}{\gamma_n}\right)^2$$

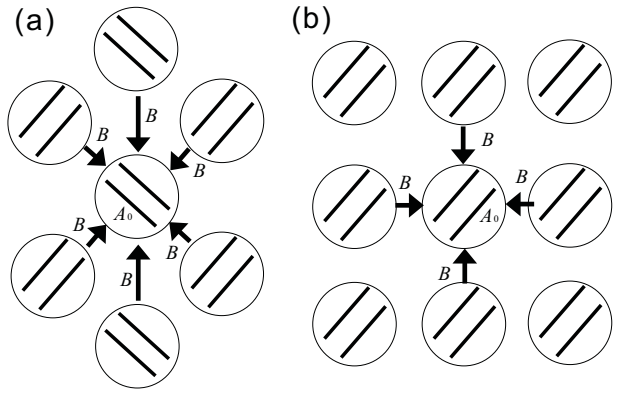

Figure 5.2: Schematic view of the hyperfine coupling field around neighboring dimers. (a) κ type. (b) β' type.

where F is a form factor due to the anisotropic hyperfine coupling constant (see the analytical expressions of ^{13}C NMR for κ-$(ET)_2X$ [10]), and γ_e and γ_n are gyromagnetic ratios of electrons and ^{13}C nuclei, respectively. If $\mathcal{K}(\alpha) = 1$, the system is regarded as a simple metal. $\mathcal{K}(\alpha) < 1$ is regarded as indicative of ferromagnetic correlations, whereas $\mathcal{K}(\alpha) > 1$ is indicative of anti-ferromagnetic correlations. The pressure dependence of the Korringa factor in κ-NCS [8] is shown in Fig.5.3. Increasing pressure from ambient pressure to 0.25 GPa reduces the Korringa factor by 50 %, whereas additional pressure cause a further slow decrease. This behavior is similar to the pressure dependence of m_c^*. The behavior of $\mathcal{K}(\alpha) > 1$ suggests additional antiferromagnetic contributions. However, the estimated value was normalized to 8 at ambient pressure [10]. Although these results showed a qualitative similarity between the Korringa factor and m^*, the quantitative value of the Korringa factor at the pressure at which $m^* = m_0$ has not been determined. As it is important to verify the antiferromagnetic correlation experimentally, we evaluated the Korringa factor at ambient pressure by calculating the form factor F from the tensor of κ-NCS. Using the appropriate equation, we calculated that, for the κ-NCS salt, $F_{\rm in} = 0.13$ and $K_{in}(\alpha) = 5.90$ for H $\perp$conduction plane at 15 K (Fermi liquid state) . As $\mathcal{K}(\alpha) \approx 5.9$ at ambient pressure, an antiferromagnetic factor may contribute to κ-NCS. Using a $\mathcal{K}(\alpha) \approx 2.2$ at 0.9 GPa, we found that electron correlation became weak, such as for a quasi-one dimensional organic conductor $(TMTSF)_2PF_6 \approx 1$ and for alkali metals ≈ 0.6. These results suggested that

antiferromagnetic correlation almost disappeared at the pressure at which $m^* = m_e$.

Evaluation of the Korringa factor of κ-Br at the ambient pressure in the same way resulted in $F_{\rm in} = 0.15$ and $\mathcal{K}_{in}(\alpha) = 5.75$, values comparable to those of κ-NCS. The almost identical superconducting temperatures of the two salts suggest a correlation between superconductivity and antiferromagnetic properties.

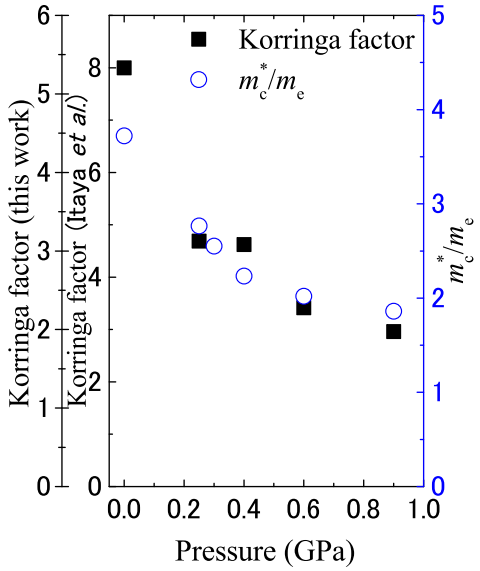

Figure 5.3: Pressure dependence of the Korringa factor and the effective cyclotron mass.

5.1.3 Further applications of the tensors

To characterize the superconductivity persisting in fields in excess of the Pauli limit (H_p), ^{13}C NMR measurements were performed on κ-NCS with an external field parallel to the conducting layers [55, 56]. Above H_p, the spectral evolution changed abruptly and multiple peaks were detected at higher and lower frequencies. The second moment increased from its low-field value as a function of the applied field, indicating a transition from within the superconducting state associated with an increase in electronic spin polarization. However, the properties of the high field phase were unclear

because the spectra were complicated by Pake doublets and the lack of site assignments. Site assignments are possible because dipolar splitting widths can be calculated using hyperfine coupling tensors. Moreover, as shown in Fig.4.5, the field dependence of NMR spectra for the field parallel to the b axis were simpler to compare than the field dependence of the spectra parallel to other directions. Experiments using the field parallel to the b axis on one side of the central C=C bond in ET molecules enriched with ^{13}C, thus avoiding the Pake doublet problem, are required to determine the high field phase. In the FFLO state, the NMR spectra broaden due to a spatial distribution of χ from $\chi_s = 0$ to $\chi_{s\mathrm{Metal}}$. Hence the spectrum should span a range from 116 to 448 ppm. The chemical shift and hyperfine tensors reported here may help analyze these spectra because the tensors can be used to calculate peak positions.

The tensors determined for κ-Br can be used for κ-Cl and κ-I, which belong to the same crystal system [57]. In κ-Cl, multiferroic behavior may be due to a dielectric anomaly [58]. The κ-I salt showed different behavior with the same disorder, which could not be determined using the phase diagram [59, 60]. These novel physical properties have not been studied in detail. These tensors should contribute to NMR analysis of these properties.

5.2 κ-$(ET)_2Cu_2(CN)_3$

5.2.1 Modification of transfer integrals

I consider the modification of transfer integrals due to the extended $4d$ orbital of the Se atoms. The 5 %, STF substitution modifies the transfer integrals of the affected sites as shown in Fig. 5.4, where t_a, t'_a, and t_b are transfer integrals among dimers. In fact, the transfer integral in the side-by-side direction of the BEDT molecules of α-$(STF)_2I_3$ is 46.5% greater than that of α-$(ET)_2I_3$ [61]. Since transfer integral consist of ET and STF in the substituted system, transfer integral should be around half of that consist of STF and STF. Therefore, the interdimer transfer integrals around the substituted dimer may be estimated to be about 20% greater than that of the original dimer. As shown in Fig. 5.4, 20% of the triangular lattices are distorted; thus, the resulting area of the original triangular lattice is confined to a radius of 2–3 dimers.

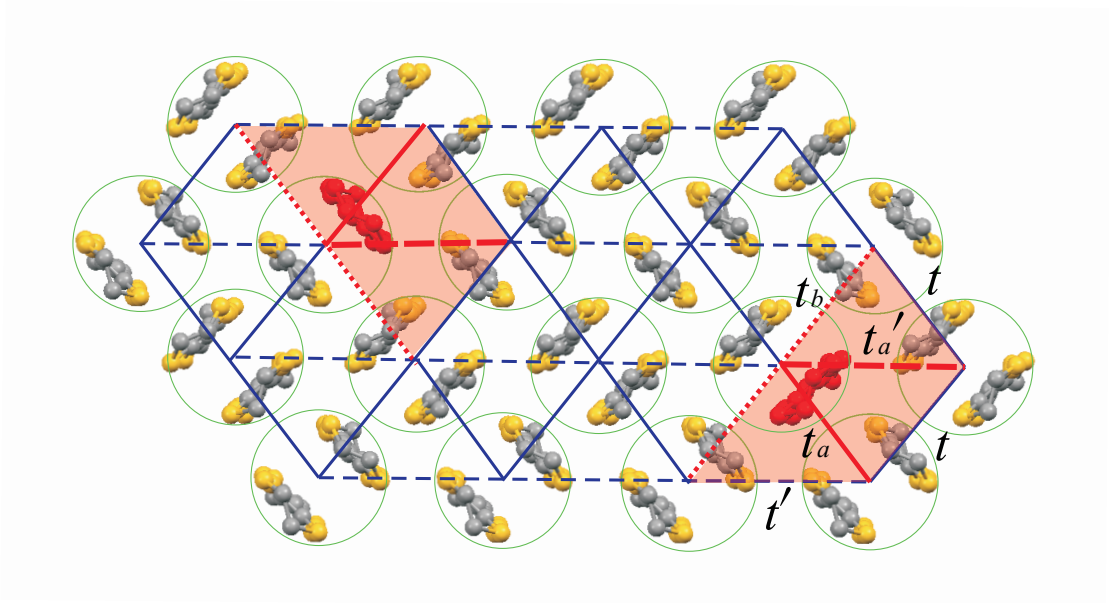

Figure 5.4: Triangular lattice of the x=0.05 sample.

5.2.2 Conductivity

Δ of the x=0.05 sample was about half value of the pure sample. Since STF substitution is not carrier doping, we have to rule out the carrier doping and consider another mechanism. The STF substitution increases transfer integrals among various sites as shown in Fig.5.4. In the hopping picture, Δ is expected to decrease as transfer integrals increase. Therefore, the decrease of the Δ should be the consequence of the enhancement of the transfer integrals due to the Se substitution. At low temperature, the conductivity was explained by the VRH model, suggesting that no intrinsic charge gap open in both samples as in the previous work for the pure sample[17]. To explain for $d = 1$ for the x=0.05 sample, the competition between electron correlation and randomness might be taken into account[21]. We could confirm the remarkable impurity substitution effect about charge degrees of freedom.

To confirm the substitution effect, opitical conductivity measurements were performed. Figure 5.5 shows optical conductivity of pure, $x = 0.4$, 0.11 samples for $E||b$. Spectral weight (SW) of the $x = 0.04$ sample shifted from high to low frequency compared with that of the pure sample and this behavior was enhanced with decreasing temperature. $x = 0.11$ sample exhbited more pronounced behavior at low temperature. These results indicate that the substitution affected electronic state of the pure sample.

5.2.3 Spin susceptibility

Figure5.6 shows ^{13}C NMR spectra of the $(CN)_3$ salt at H_0=8 T applied perpendicular to the conducting plane using both side of central C=C bond enriched sample[47]. The observed four resonance lines at high temperatures come from the inner and outer sites with the nuclear dipolar coupling. Due to the nuclear dipolar coupling, the behavior of the NMR shift was complicated. Two peaks at 10.8 K may be due to the inner and outer sites whereas two peaks below 1 K might be due to the dipole splitting of 200 ppm.

We could clarify the temperature dependence of the NMR shift by one side of the central C=C bond substituted with ^{13}C isotope. The NMR shift δ is written as

$$\delta = K + \sigma = A\chi_s + \sigma \tag{5.1}$$

where K is the Knight shift, A is the hyperfine coupling constant, and σ is the chemical shift. In order to discuss the spin susceptibility, the chemical

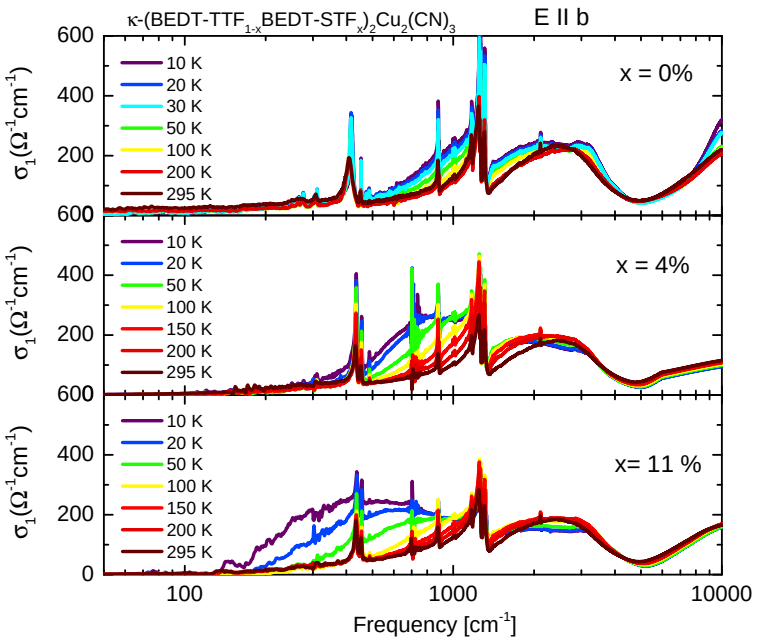

Figure 5.5: Optical conductivity of pure, $x = 0.4$, $x = 0.11$ samples for $E||b$.

shift of $(ET)^{+0.5}$ under this configuration was evaluated to be σ=117 ppm from the chemical shift tensor of α-$(ET)_2I_3$[48].

As shown in Fig.4.23, finite susceptibility seems to remain at 0 K in the static susceptibility measurement in the pure sample, which is one of the evidences of the spin liquid picture. However, because of slight paramagnetic impurities, it is unclear whether finite susceptibility remains or not. NMR can detect local spin susceptibility separately from paramagnetic impurities. The value of the NMR shift at low temperature was almost the same as the chemical shift shown in Fig.4.12, indicating spin susceptibility vanished at 0 K. This is inconsistent with the spin liquid picture.

In the x=0.05 sample, the behavior of static susceptibility was quantitatively similar to that of the pure sample from 300 K down to 2 K shown in Fig.4.23. Similarly to the pure sample, no peak splitting was observed at low temperature and the value of the NMR shift was almost the same to the chemical shift, indicating spin susceptibility vanished at 0 K as well as in the pure sample at low temperature. These results suggest that the substitution should not change the spin susceptibility, as opposed to the distinct impurity substitution effect of conductivity.

Next I discuss the spin susceptiblity of the impurity sites. $\chi_{\rm imp}$ was estimated 60% of $\chi_{\rm bulk}$. The 60% spin susceptibility leads the magnetic moment of 0.8 μ_B in a dimer consisting of ET and STF, suggesting dimer-Mott insulating picture that is 1 μ_B per one dimer breaks locally in the STF-substituted system.

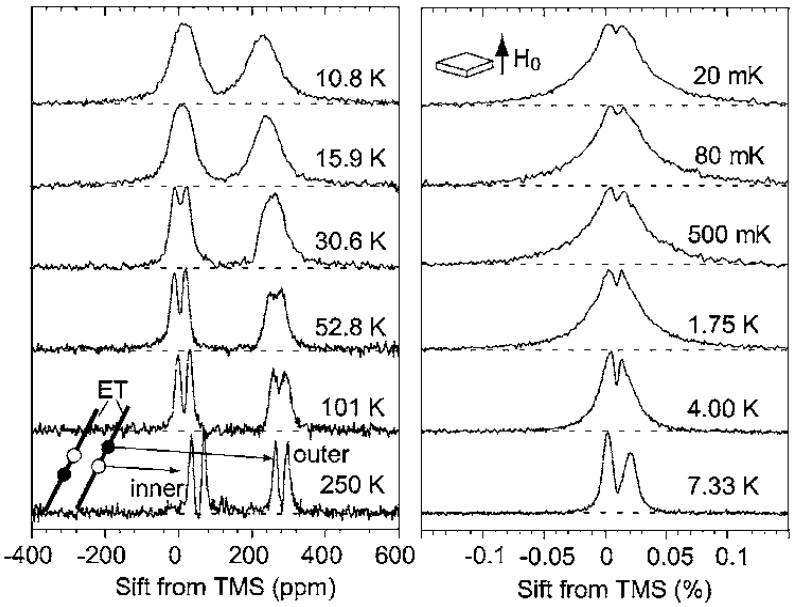

Figure 5.6: ^{13}C NMR spectra of κ-$(ET)_2Cu_2(CN)_3$ at H_0=8 T applied perpendicular to the conducting plane where ^{13}C was enriched for the doubly bonded carbon sites at the center of ET.

5.2.4 Linewidth

In the pure sample, linewidth is gradually broadened on decreasing temperature, whereas T_2^{-1} remains constant. This indicates that the broadening is attributed primarily to the inhomogeneous broadening. Moreover, the outer site which has larger hyperfine coupling constant is broader than the inner site. The ratio of the inhomogeneous width was about 2 from 60 K where linewidth broadening developed down to 10 K and comparable to the ratio of the hyperfine coupling constants. The broadening of the linewidths is correlated with hyperfine coupling constants, suggesting the inhomogeneity of the spin density on molecules.

The spin susceptibility vanished at 0 K from the NMR shift at low temperature. If the spin singlet state is formed, the linewidth is expected to be narrow. However, the FWHM did not decrease at low temperature. Shimizu *et al.* reported that the linewidth is proportional to the magnetic field as shown in Fig.5.7[47]. Recently, μSR measurements suggested that the spins fluctuate paramagnetically in zero-field and the microscopic phase separates into the singlet phase and the paramagnetic phase below 3 K[62]. They proposed the paramagnetic microscopic islands surrounded by the singlet sea the with finite gap as shown in Fig.5.8. This picture is consistent with that the NMR spectra at the chemical shift with broad linewidth and the behaivor that the linewidth is proportional to magnetic field at low temperature. Since the volume fraction of the singlet sea is much larger than that of the paramagnetic area, the paramagnetic spin behaves as a magnetic impurity, contributing only to linewidth of non-magnetic NMR spectrum.

In the x=0.05 sample, the line broadening was also observed below 60 K and larger than that of the pure sample above 10 K. Because T_2^{-1} of the x=0.05 sample is constant, the broadening is attributed to the inhomogeneous broadening as well as the pure sample. The ratio of the inhomogeneous width of the inner and outer sites resembles to that of the hyperfine coupling constant. This suggests that the impurity substitution effect should enhance the disorder.

In frustrated spin systems, impurities can induce local staggered moments and line broadening is expected owing to staggered spin density oscillations, as expected from the AF character of magnetic correlations [63, 64]. If impurities induce AF moment, the FWHM of x=0.05 is broader than that of the pure sample. The FWHM in both sample was almost the same at the lowest temperature in contrast to the behavior above 10 K, suggesting

another mechanism of linewidth broadening. This result supports the paramagnetic island picture. The paramagnetic island does not depend on non magnetic impurities such as the STF. Therefore, the paramagnetic island is independent on the STF and makes a inhomogeneous dipole field with the same amplitude in both samples, resulting in the same amplitude of broadening in both samples. The finite susceptibility in the static susceptibility measurement might be the consequence of this paramagnetic components.

NMR at the impurity site also gives consistent results. The FWHM of the NMR line of the impurity site at low temperature is less than that of bulk sites. The ratio of inhomogeneous linewidth $\nu_{\rm imp}/\nu_{\rm bulk}$ is about 0.5, which is consistent with $\chi_{\rm imp} \simeq 0.6\chi_{\rm bulk}$. Therefore, $\Delta\chi/\chi$ at the bulk and impurity sites are much the same since $\nu \propto \Delta\chi$. These results indicate that the difference of the linewidth at the bulk and impurity sites is described by the difference of the local spin susceptibility and that the impurities do not induce staggered moments, which are consistent with no indication of the staggered moments in comparison of the FWHM for the bulk sites between the pure and $x = 0.05$ samples.

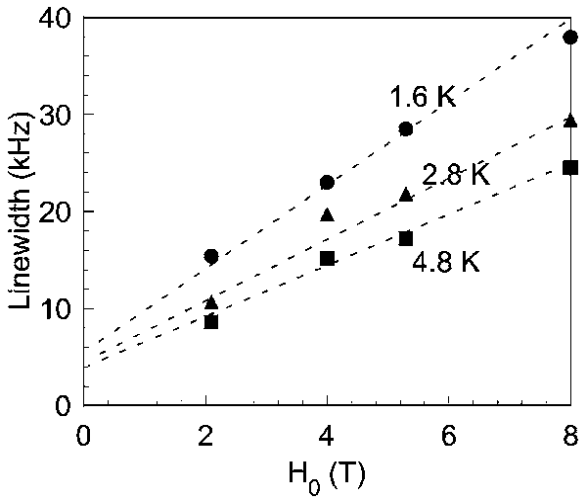

Figure 5.7: External field dependence of the linewidth at various temperatures ($H_0 \parallel a^*$).[47]

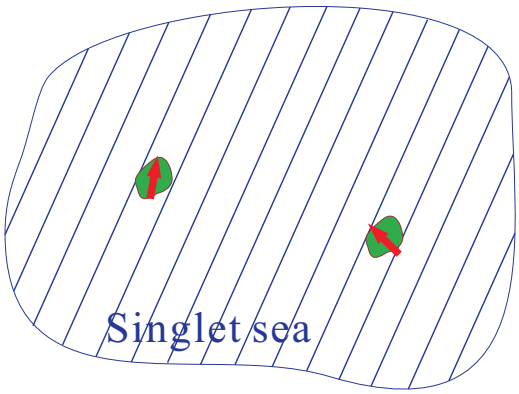

Figure 5.8: Paramagnetic islands in singlet sea.

5.2.5 Spin-lattice relaxation rate

T_1^{-1} detects the local magnetic fluctuation at nuclei. It is sensitive to the type of the magnetic fluctuation. $(T_1T)^{-1}$ of the pure sample reproduced the previous work[47]. $(T_1T)^{-1}$ increases with decreasing temperature below 8 K and distribution of T_1^{-1} below which linewidth broadens rapidly as shown in Fig.4.14. Thus, this behavior below 6 K is still unclear. As shown in Fig.5.4, we introduced a STF into triangular lattice at the interval of about three dimers. This affected the behavior of charge as DC and optical conductvities revealed. However, the behavior of $(T_1T)^{-1}$ of x=0.05 sample was very similar to that of the pure sample as shown in Fig.4.16, indicating little effect by the impurity substitution. If the geometrical frustration exists, $(T_1T)^{-1}$ changes by the suppression of the frustration. Thus this result is inconsistent with the spin liquid picture indicating the behavior of $(T_1T)^{-1}$ not originated from the frustration.

Scaling $(T_1T)^{-1}$ for impurity sites by a factor of two matches well with the results for $(T_1T)^{-1}$ for the bulk sites. According to Anderson-like behavior, CN_3 sale may be regarded as disordered metal. In Fermi liquid theory, $(T_1T)^{-1}$ is proportional to the square of the product of the hyperfine coupling constant $A_{\rm hf}$ and the density of state $N(E_{\rm F})$ at the Fermi energy:

$$\frac{1}{T_1T} = \frac{\pi k_B}{\hbar} A_{\rm hf}^2 N^2(E_{\rm F}). \tag{5.2}$$

Here, $N(E_{\rm F})$ corresponds to the local spin susceptibility. Since $\chi_{\rm imp}$ is $0.6\chi_{\rm bulk}$, the $N^2(E_{\rm F})$ which was 2.77 ($= 1/0.6^2$) times smaller than that for the bulk site was expected. Therefore, the scaling factor of two should be explained by the small $N(E_{\rm F})$ at the impurity site.

The similar behaviors of $\Delta\chi/\chi$ and $(T_1T)^{-1}$ for both sites suggests that the electronic properties at the bulk and impurity sites are described by one-fluid model. The result of the impurity site where Mott insulating picture breaks is the same as that of the bulk site indicates that the magnetic behavior of $(CN)_3$ salt is not due to the geometrical frustration. Instead, the suppression of the AF transition and the electronic state of $(CN)_3$ salt may be due to disorder and electronic correlation, in addition to the ideal geometrical frustration, as theoretically suggested [19, 20, 21, 65].

5.2.6 Interpretation of the behavior in κ-$(ET)_2Cu_2(CN)_3$

The static and dynamic magnetic properties did not change as opposed to the distinct impurity substitution effect of conductivity. The $(CN)_3$ salt may have already undergone the Mott-Anderson transition by the inherent random potential presented in the pure sample. The impurity substitution effect of conductivity could be explained as a consequence of enhancing the disorder. Therefore, we interpret the behavior of the $(CN)_3$ salt as a disordered metal. Spin susceptibility in an itinerant system is written as

$$\chi_s \propto N(E_F) \propto \frac{1}{W}, \tag{5.3}$$

where $N(E_F)$ is density of state and W is bandwidth. When the bandwidth is narrow, the electron tends to be localized inhomogeneously. Geiser *et al.* did band calculation and pointed out that the bandwidth was small in the $(CN)_3$ salt[41]. Indeed, χ of the $(CN)_3$ salt is lager than that other κ salts as shown in Fig.5.9, suggesting the $(CN)_3$ salt could have the narrow bandwidth relative to other κ-$(ET)_2X$ salts. Hence, the $(CN)_3$ salt is expected to readily localize electrons. Because spin density is considered to be proportional to electron density, local spin susceptibility becomes inhomogeneous if the electron localizes inhomogeneously. The result that the ratio of the inhomogeneous width is comparable to hyperfine coupling constants, suggesting the conducting electron is localized inhomogeneously. Since the impurity substitution makes additional disorder directly into the conducting sheet, the experimental result that the linewidth broadening in x=0.05 was larger than that in the pure sample could also be explained by the localization picture.

The localization picture based on the assumption that the electronic structure of the $(CN)_3$ salt is essentially the same as other κ-$(ET)_2X$ salts with relatively narrow band width. In the localization picture, the same behavior of $(T_1T)^{-1}$ is expected. Hence, it is important to compare $(T_1T)^{-1}$ in the $(CN)_3$ salt with other κ-$(ET)_2X$ salts. However, there were not any systematic comparison of $(T_1T)^{-1}$ in κ-$(ET)_2X$ salts. Since the $(CN)_3$ and NCS salts are almost iso-structure, we chose the NCS salt as a reference[8]. Figure5.10 shows temperature dependence of normalized $(T_1T)^{-1}$ by χ^2 of the $(CN)_3$ and NCS salts at the field applied perpendicular to the conducting plane. The temperature dependence of the $(CN)_3$ salt was quantitatively similar to the NCS salt above T^* which is the characteristic temperature

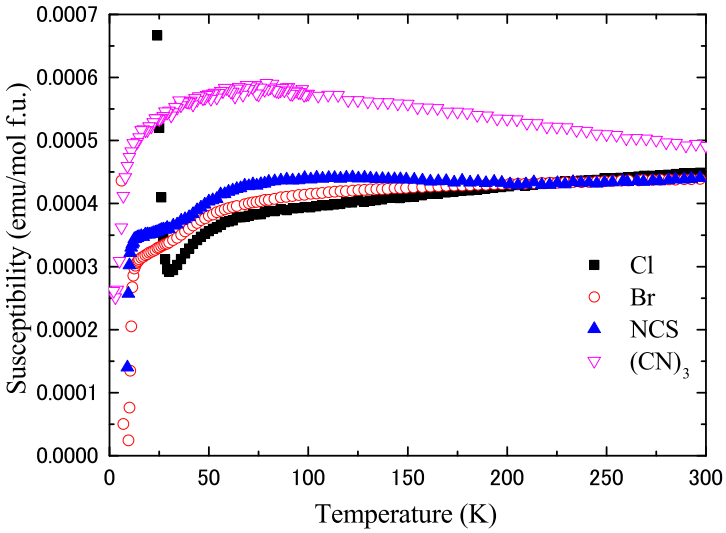

Figure 5.9: Temperature dependence of static susceptibility of κ-$(ET)_2X$ (X=Cu[N(CN)$_2$Cl, Cu[N(CN)$_2$Br, Cu(NCS)$_2$, and Cu$_2$(CN)$_3$).

where the AF fluctuation in the NCS salt is suppressed. The quantitative similarity suggests that the magnetic fluctuation on the $(CN)_3$ salt be the same as that on other κ-$(ET)_2X$ salts above T^*.

5.3 λ-$(ET)_2GaCl_4$

5.3.1 Magnetic ordering

As shown in Fig. 4.23, the behavior of χ can be explained by two-dimensional $S = 1/2$ square lattice Heisenberg AF model [50] with exchange interaction $J/k_B = 98$ K. This result indicate AF interaction exists in λ-$(ET)_2GaCl_4$. The increase of χ below 13 K may be due to the canting antiferromagnetism or impurities.

Indeed, the NMR line splitting was observed at 13 K, indicating AF odering occured. The splitting of the NMR peak into a finite number of peaks demonstrates that the local field distributes discretely, indicating that the AF magnetic structure is commensurate.

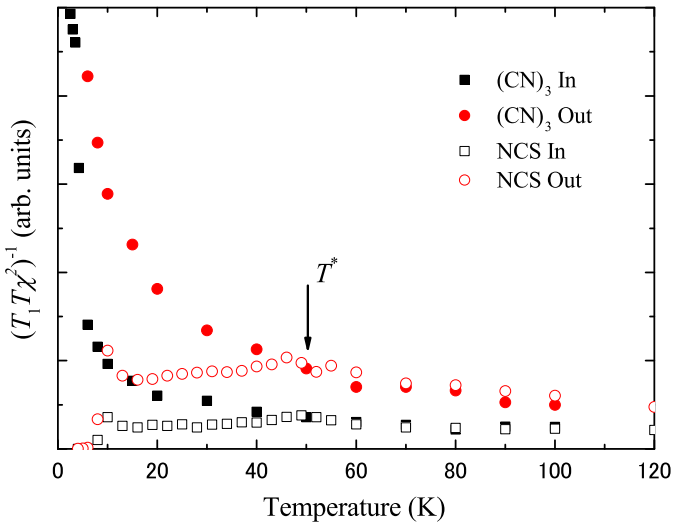

Figure 5.10: Temperature dependence of $(T_1T\chi^2)^{-1}$of κ-$(ET)_2X$ (X =$Cu_2(CN)_3$ and $Cu(NCS)_2$) at the field applied perpendicular to the conducting plane.

5.3.2 Dimer-Mott insulationg picture

The commensurate AF structure can be explained by the dimer-Mott insulating picture. Figures 5.11(a) and 5.11(b) show the donor arrangements of the λ-type and κ-type salts, respectively. Although the arrangements of the dimers are different from each other, the overlap characteristics of two ET molecules in a dimer are almost the same. The interplanar distance between two ET molecules forming a dimer is 3.769 Å [31] for λ-type salts and 3.45–3.53 Å for κ-type salts [66], and the intradimer transfer integral of λ-$(ET)_2GaCl_4$ is more than twice as large as the other transfer integrals [67, 30], suggesting that λ-type salts have a dimerized structure as in κ-type salts (see Fig1.5). The extended Hučkel tight-binding band calculation shows the upper two and lower two bands with the large energy gap due to dimerization in λ-type salts, as shown in Fig. 5.11(c) [30], which is similar to the case of κ-type salts in Fig. 5.11(d) [3]. Because $GaCl_4^-$ is a monovalent anion and the formal charge of a donor molecule is $+0.5e$, the lower two bands are fully filled and the upper two bands are half-filled. Hence, the electronic system is regarded as a half-filled system, called the dimer-Mott system, as in

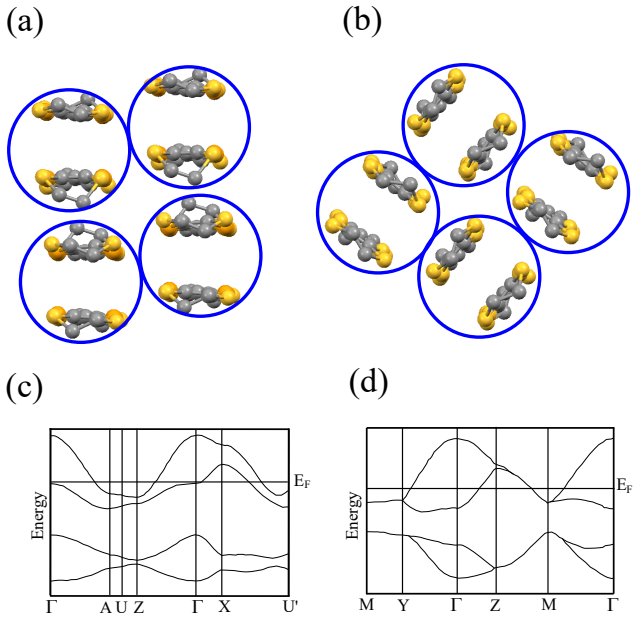

Figure 5.11: Dimer arrangements of (a) λ-type and (b) κ-type salts. Circles represent dimers. Band structures of (c) λ-type [30] and (d) κ-type [3] salts.

κ-type salts. In the dimer-Mott system, electrons localize because of larger effective on-site Coulomb repulsion U_{eff} than interdimer transfer integral t' as shown in Fig. 5.12. Hartree–Fock calculations suggested that the AF dimer-Mott state can appear in λ-type salts [68]. In a dimer-Mott system, one spin is localized on one dimer unit due to on-site Coulomb repulsion, and the AF spin fluctuation from the exchange interaction J is expected.

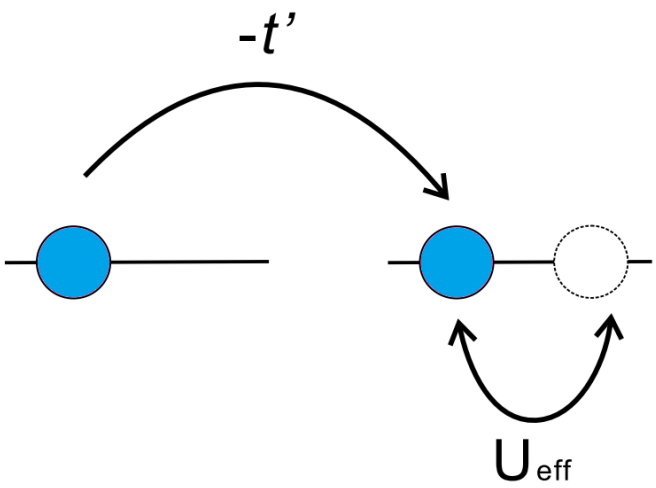

Figure 5.12: Competition between the interdimer transfer integral t' and the effective on-site Coulomb repulsion U_{eff} in Mott insulator.

We could evaluate J from $1/T_1$, using Moriya's expression [69]. The $1/T_1$ of antiferromagnets at a sufficiently high temperature is expressed as

$$\frac{1}{T_1} = \frac{\sqrt{2\pi} g^2 \gamma_{\mathrm{N}}^2 A_{\mathrm{hf}}^2 S(S+1)}{3\omega_{ex}}, \tag{5.4}$$

where

$$\omega_{ex}^2 = \frac{2zJ^2 S(S+1)}{3\hbar^2}. \tag{5.5}$$

Here, g is the g value of the electron, γ_{N} is the gyromagnetic ratio of the ^{13}C nuclei, and z is the number of nearest-neighbor spins. A_{hf} is the hyperfine coupling constant. We assumed that z is 4 for the square lattice system, and A_{hf} is 2.9 kOe/μ_{B} from the results in β'-type salts, which have the same overlapping mode of ET in a dimer [54, 66]. $1/T_1$ is 45 1/s and constant in the high-temperature region. From the $1/T_1$ value, J/k_{B} was estimated to

be 112 K, which is in good agreement with the $J/k_B \simeq 98$ K value evaluated from the magnetic susceptibility measurement. This result also supports the electronic state of this salt described by the dimer-Mott picture, according to which the localized spins interact with J, and the ground state of λ-$(ET)_2GaCl_4$ is the AF ordered state as shown in Fig. 5.13

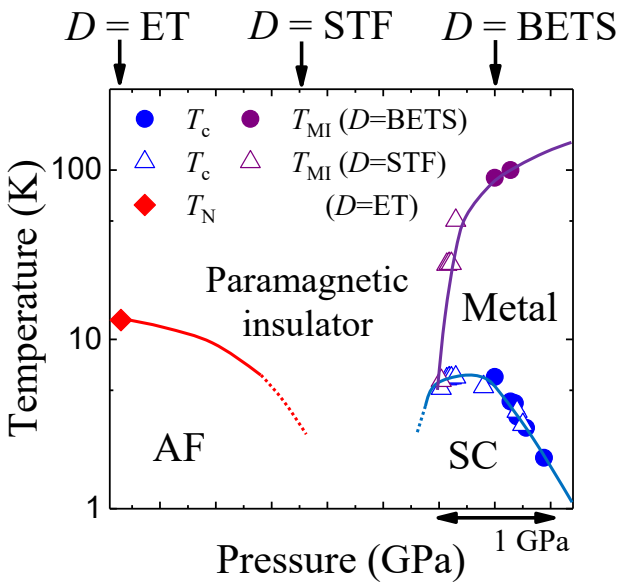

Figure 5.13: P-T phase diagram of λ-D_2GaCl_4 (D = ET, STF, and BETS).

5.3.3 Relation to AF ordering in λ-$(BETS)_2FeCl_4$

I mention the magnetic nature of λ-$(BETS)_2FeCl_4$, which is isostructural with λ-$(BETS)_2GaCl_4$ and has magnetic anions. It is a coexistent system of $3d$ spins in the $FeCl_4$ layers and π electrons in the BETS molecule layers. It exhibits an AF ordering in zero magnetic field accompanied by a metal–insulator transition at 8.3 K as shown in Fig. 5.14[67]. The $3d$ spins in λ-$(BETS)_2FeCl_4$ were considered to play the primary role in the AF ordering, as in a similar system of κ-$(BETS)_2FeX_4$ (X = Cl, Br) [70, 71]. However, Akiba *et al.* performed specific heat measurements for λ-$(BETS)_2FeCl_4$ and revealed that the $3d$ spin system shows a Schottky-like anomaly in the magnetic heat capacity below T_{MI}, as shown in Fig. 5.15. If the π and $3d$ spins

cooperatively align antiferromagnetically below T_{MI}, the larger peak of the specific heat would only exist at T_{MI} without the formation of the hump. The aunthors suggested that the localized π electron system undergoes an AF ordering at T_{N}, while the $3d$ spin system maintains a paramagnetic state under the effective magnetic field arising from the $\pi-d$ interaction. [72]. However, the AF ordering state had not been found in λ-type systems with nonmagnetic anions. The observed AF phase in λ-$(\mathrm{ET})_2\mathrm{GaCl}_4$ may yield information on the nature of the AF ordering in λ-$(\mathrm{BETS})_2\mathrm{FeCl}_4$. Our result revealed that λ-type salts are a dimer-Mott system, and there is an AF Mott insulating phase adjacent to the SC phase. Hence, there is a possibility that in the case of λ-$(\mathrm{BETS})_2\mathrm{FeCl}_4$, which has localized $3d$ spins, the π electron system undergoes the AF ordered state adjacent to the SC phase.

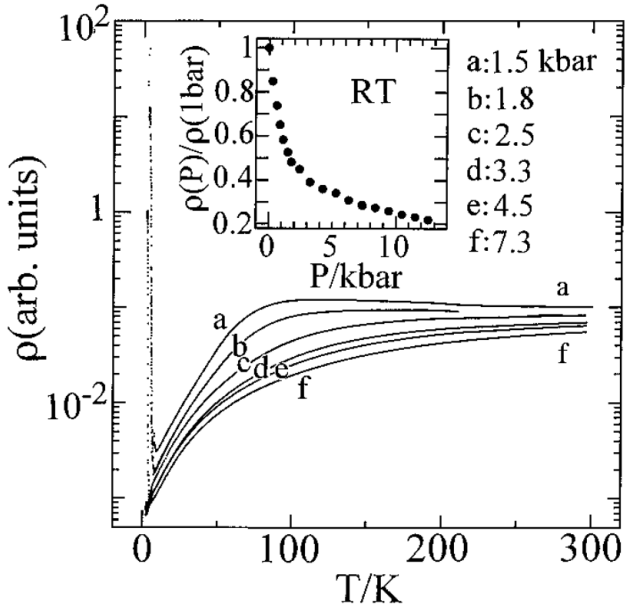

Figure 5.14: Resistivity of λ-$(\mathrm{BETS})_2\mathrm{FeCl}_4$ as a function of pressure. The inset shows the pressure dependence of the room-temperature resistivity.

5.4 λ-$(STF)_2GaCl_4$

5.4.1 Magnetic ordering

NMR peak splitting was not observed down to 1.63 K. Above 20 K, the behavior of $1/T_1$ is similar to that of λ-STF salt qualitatively. $(T_1T)^{-1}$ deviated from Curie-Weiss law below 15 K and the deviation is expected near transition temperature. However, no divergence peak was observed. Noted temperature dependence of $1/T_1$ has ambiguity because of distribution of $1/T_1$. These results indicate no magnetic ordering occurs and AF spin fluctuation persists down to the low enrgy region which is two order of magnitude smaller than the exchange interaction $J \simeq 165$ K. J is calculated with $1/T_1 = 24$ 1/s as well as λ-ET salt (see Eq.5.5). J/k_B is 215 K for square lattice and 176 K for triangular lattice, which is in good agreement with $J/k_B = 165$ K from static magnetic susceptibility fit by triangular lattice Heisenberg model.

5.4.2 Comparison of $(T_1T)^{-1}$ in λ-D_2GaCl_4

Figure 5.16 shows $(T_1T)^{-1}$ of λ-ET, STF, and BETS salts as a function of temperature. With decreasing temperature, $(T_1T)^{-1}$ of ET and STF salts increases gradually, indicating development of AF spin fluctuation since $(T_1T)^{-1}$ is proportional to $\sum_q (A_q A_{-q}) \frac{\chi''_q(\omega)}{\omega}$. With changing the donor molecule from ET to BETS (which means increasing itinerancy), $(T_1T)^{-1}$ at high temperature is suppressed. These results are consistent that λ-D_2GaCl_4 is discribed in terms of chemical pressure effect.

5.4.3 Absence of magnetic ordering

It is remarkable that magnetic ordering was not observed at $T < J/100$ in STF salt. I consider that the absence of no AF transition on the dimer-Mott insulating picture. λ-STF salt may be regarded to have spin-1/2 anisotropic trinagular lattices due to expansion of transfer integral of Se atoms. There is a possibility that geometrical frustration due to the triangular lattice suppresses the AF transition and quantum spin liquid state is realized at low temperature. In the candidate of spin liquid material, $1/T_1$ was suppressed at low temperature. Our observation, the developping $1/T_1$ at low temperature

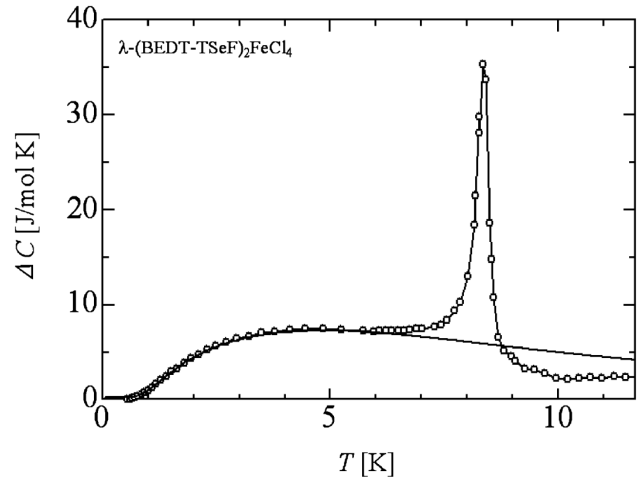

Figure 5.15: Excess specific heat ΔC of λ-$(BETS)_2FeCl_4$ obtained by subtracting the lattice and electric specific heats estimated for λ-$(BETS)_2GaCl_4$. The solid curve shows the calculated specific heat based on the paramagnetic $3d$ spin ($Fe^{3+}S = 5/2$) system under the effective magnetic field $H_{\pi-d} = 4$ T.

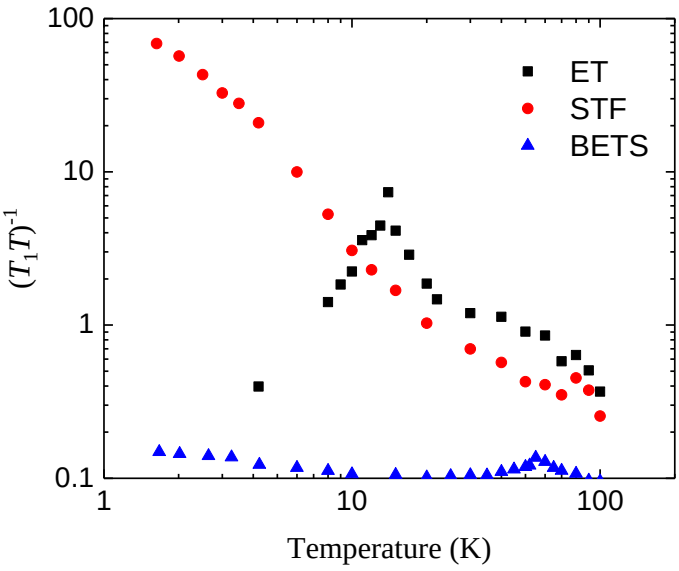

Figure 5.16: $(T_1T)^{-1}$ of λ-ET, STF, and BETS salts as a function of temperature.

was qualitatively different from that in the spin liquid candidates. Then we have to focus on the other possibility.

The inhomogenetity would plays an important role for absence of magnetic ordering. In the case of the λ salts, two non-equivalent molecules A and B form a dimer and each molecule has positional disorder because the postion of Se atoms are unsymmetric in the molecule, as shown in Figs. 1.26(b) and 1.26(c). The positional disorder enhances the random potential, giving rise to to the inhomogenety of the spin density on conducting layers. Indeed, a disorder effect is observed by comparison of conductivity measurement between symmetrical and unsymmetrical-STF salts[73].

Absence of magnetic ordering in disordered state was also observed in other organic conductors. X-ray irradiation to an AF insulator, κ-$(ET)_2Cu[N(CN)_2]Cl$, suppressed the AF transition. κ-$(ET)_4Hg_{2.89}X_8$ (X= Br, Cl) which shows anomalous AF fluctuations at low temperatures without AF transition has a mercury chain incommensurate against the donor lattice which may relate to disorder [74]. Indeed, linewidth of X=Br salts became broad, suggesting the inhomogeneity of the electron. Applying pressure to X=Br salt, the broadening of the linewidth was suppessed and the salt showed the superconductivity. The absence of AF transition can be understand by inhomogeneity of the electron on the molecule.

5.4.4 Anomalous line shift

Figure 5.17 shows temperature dependence of NMR shift with the spin susceptiblitiy χ_s from SQUID measurement [32]. In general, the NMR shift δ is proportional to the spin susceptibility (see Eq.5.1), however, the shfit was not scaled to the spin susceptibility below 15 K as shown in Fig. 5.17, showing the negative value at low temperature. Similar behavior is observed in κ-$(ET)_2Cu[N(CN)_2]Cl$ [53, 75]. The K is not sclaed to χ_s even above T_N as shown in Fig. 5.18. Field-induced staggered moments in the short-range ordered spins can appear in the presence of Dzyaloshinsky-Moriya (DM) interaction. Therefore, such a situation might occurs in λ-$(STF)_2GaCl_4$. Noted that magnetic susceptibility at low temperature depends on subtraction of magnetic impurity.

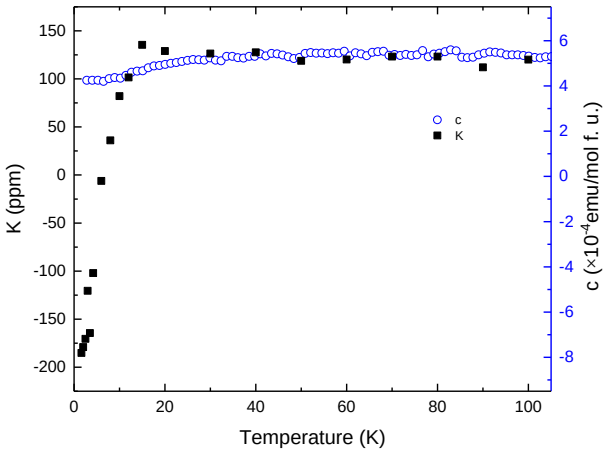

Figure 5.17: Temperature dependence of NMR shift and magnetic susceptibility. The magnetic susceptibility is taken from Ref. [32].

5.4.5 Comparsion with a x-ray irradiated Mott insulator

I compare the present results with the behavior of a disordered Mott insulator, x-ray irradiated κ-$(ET)_2Cu[N(CN)_2]Cl$. Figure 5.19 shows temperature dependence of ^1H T_1^{-1} before and after 500-hour x-ray irradiation[23]. By introducing disorder with x-ray irradiation, ^1H NMR spectrum does not change from 100 K down to 340 mK without AF transition. Temperature dependence of $(T_1T)^{-1}$ of x-ray irradiated κ-$(ET)_2Cu[N(CN)_2]Cl$ shows monotonous increase even below T_N of non-irradiated κ-$(ET)_2Cu[N(CN)_2]Cl$. T_1^{-1} shows neither critical increase towards long-range mangetic ordering nor a cusp stucuture due to spin freezing at whole temperature. Below T_N of non-irradiated κ-$(ET)_2Cu[N(CN)_2]Cl$, temperature dependence obeys a power law, $T_1^{-1} \propto T^{0.5}$, whereas T_1^{-1} of λ-STF salt still increased down to 1.63 K. Therefore, 500-hour x-ray irradiation affect the electronic state more than the positional disorder and suppress critcal slowing down, and in λ-STF salt, the disorder in donor layer may suppress ideal T_N.

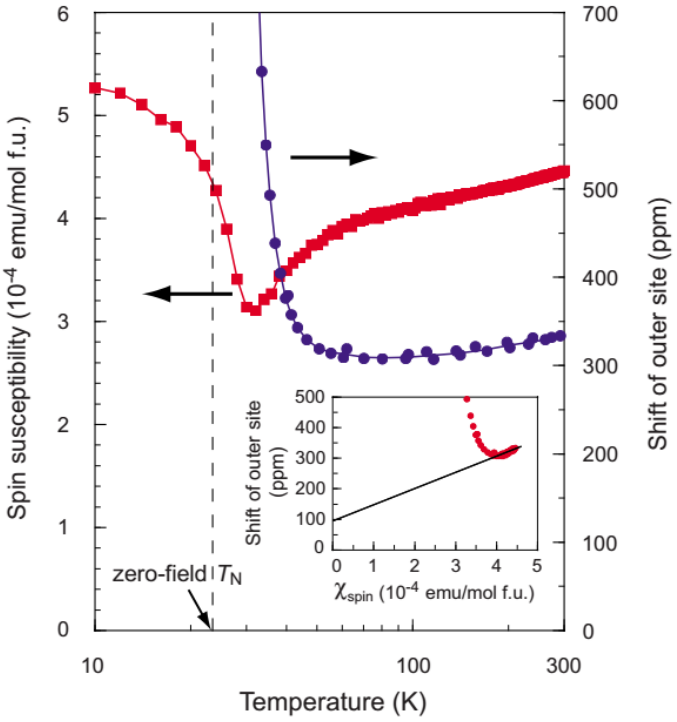

Figure 5.18: Spin susceptibility measured under 7 T and ^{13}C-NMR shift of the outer site. Solid lines are guide for the eyes. Inset: $K - \chi$ plot. The hyperfine coupling constant was estimated from the linear fitting shown in the inset. [75]

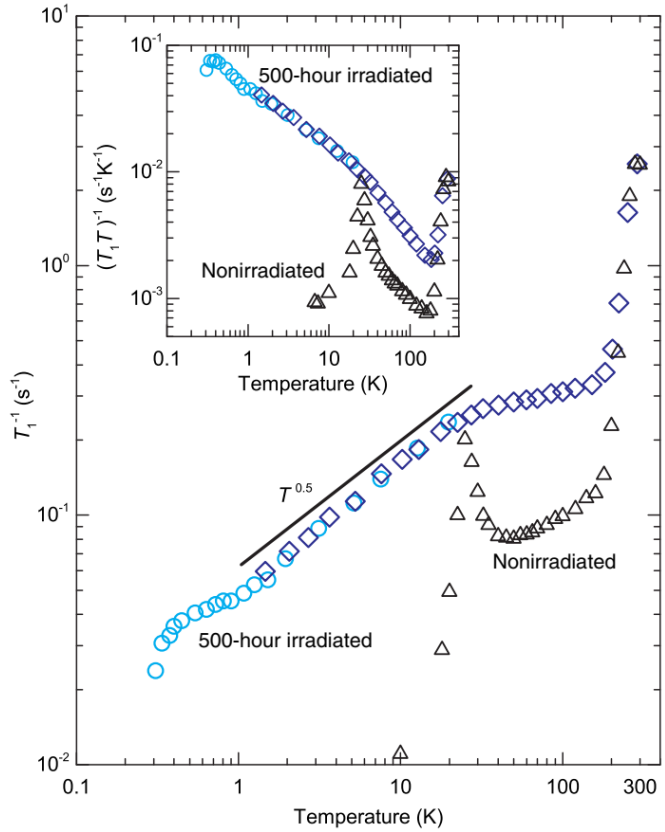

Figure 5.19: Temperature dependence of the ^{1}H nuclear spin-lattice relaxation rate of κ-Cl. The main panel shows the ^{1}H nuclear spin-lattice relaxation rate T_1^{-1} of 500-h x-rayirradiated and nonirradiated κ-Cl crystals. The inset shows $(T_1T)^{-1}$. The light blue circles and dark blue diamonds correspond to the data acquired with the use of ^{3}He and ^{4}He cryostats, respectively. The black triangles are from the previous study of a nonirradiated κ-Cl crystal.[23]

Chapter 6

Conclusion

6.1 Determination of the hyperfine tensor in κ-$(ET)_2X$ (X=Cu[N(CN)$_2$]Br, Cu(NCS)$_2$) on central ^{13}C sites

The angle dependences of NMR spectra were measured to determine their hyperfine coupling tensors. Comparisons of the tensors of κ-Br, NCS and β'-ICl_2 showed the inappropriateness of using the same tensors for different crystal systems, even for the same based systems, because hyperfine coupling tensors include the contributions of both off- and on-site dimers. Analysis of previous results using the hyperfine coupling tensors resulted in determinations of the Korringa factors of κ-NCS and κ-Br in Fermi liquid state. We found that the antiferromagnetic correlation almost disappeared at the pressure at which $m^* = m_e$. These tensors, which are basic parameters of detailed NMR spectroscopy, should contribute to analyses of NMR spectra of κ-Cl and κ-I salts, including the determination of their FFLO states and novel physical properties.

6.2 Site-specific ^{13}C NMR study on locally distorted triangular lattice of organic conductor κ-$(ET)_2Cu_2(CN)_3$

The conductivity and the magnetic properties of $(CN)_3$ salt were investigated by artificially distorting its triangular lattice by substitution of STF, which introduces disorder by modifying the transfer integrals among the STF molecules. Temperature dependence of conductivity of a sample with impurity fraction $x = 0.05$ does not much changed above 200 K, indicating that the substitution enhances conductivity and leads to a crossover temperature $T_{\rm cross}$ that is greater than that of a pure sample. At low temperature, the $x = 0.05$ sample exhibits VRH-like conductivity, suggesting that no intrinsic gap opens and that the sample is not a Mott insulator like the pure sample [17]. The NMR spectra reveal no magnetic ordering, and the spin susceptibility approaches to the chemical shift below 3 K in both samples. From 60 to 15 K, the NMR linewidth of the $x = 0.05$ sample becomes broader than that of the pure sample, indicating the STF substitution enhances disorder. The temperature dependence of $(T_1T)^{-1}$ for both samples is quantitatively similar. Moreover, the temperature dependence of $(T_1T)^{-1}$ for the impurity site where Mott insulating picture breaks is similar to that of the bulk site, suggesting that the characteristics of $(T_1T)^{-1}$ are not due to geometrical frustration. NMR spectra from the impurity site suggest a decrease in local spin susceptibility and that no staggered moments are induced. Thus, the results indicate that the static and dynamic susceptibility do not change, even at temperatures two orders of magnitude less than the exchange interaction $J \simeq 250$ K. These results are in stark contrast to the expected effect of the substitution on conductivity. Thus, we suggest that the electronic state of $(CN)_3$ salt is not only due to the ideal geometrical frustration but also due to the disorder.

6.3 ^{13}C NMR study of insulating phase in λ-D_2GaCl_4 (D= ET and STF)

^{13}C NMR and magnetic susceptibility measurements were performed to investigate the magnetic nature of the insulating ground state of λ-D_2GaCl_4

(D= ET and STF). NMR spectrum splitting and the divergence of $1/T_1$ were observed at 13 K in λ-ET salt, which indicate that an AF ordering occurs. This is the evidence that the magnetic ground state of λ-$(ET)_2GaCl_4$ is the AF ordered state. From the discrete NMR peak splitting below T_N, we revealed that the AF structure is commensurate. The commensurate AF ordering could be understood by the dimer-Mott insulating picture suggested by the band calculation. From the temperature dependence of the magnetic susceptibility, the exchange interaction (J/k_B) is estimated to be approximately 98 K, which is in good agreement with that estimated from $1/T_1$. On the other hand, temperature dependence of $1/T_1$ of λ-STF salt is similar to that of λ-ET salt above 20 K, however, $1/T_1$ increases down to 1.63 K and no magnetic ordering occurs. Linewidth also increases below 20 K, suggesting inhomogeneous electron localization due to STF molecule and the inhomogeneity may suppress the AF ordering. Development of AF spin fluctuation can be understood in terms of dimer-Mott insulating picture. These results suggest that AF spin correlation interacts in the insulating phase adjacent to the SC phase in λ-type salts. Although the absense of AF ordering in STF salt seems to be due to the inohomogeneity, it is intersting if AF ordering in λ-ET salt really remains under pressure which corresponds to the pressure of λ-STF salt.

Acknowledgment

I would like to thank Prof. Dr. Atsushi Kawamoto, Prof. Dr. Noriaki Matsunaga, Prof. Dr. Migaku Oda, and Prof. Dr. Tomobumi Mishina for reviewing my doctoral thesis.

I would like to thank collaborators Prof. Dr. Martin Dressel, Dr. Andrej Pustgow, Dr. Anja Löhle, and, Miriam sons Alonso in Univeristy of Stuttgart for the optical measurements, and Prof. Dr. kazunari Nomura, Prof. Dr. Noriaki Matsunaga, and Dr. Takaaki Minamidate for assistance fo the resistivity measurements for κ-$[(ET)_{1-x}(STF)_x]_2Cu_2(CN)_3$. I also would like to thank Miharu Uchiyama for NMR experiment of κ-$[(STF)_2Cu_2(CN)_3$, and Prof. Dr. Hatsumi Mori in the University of Tokyo for providing ^{12}C λ-$(ET)_2GaCl_4$.

Furthermore, I would like to thank Low Temperature Physics Group members Dr. Yoshihiko Ihara, Dr. Shuhei Fukuoka, Takuya Kobayashi, Akihiro Ohnuma, Kazuto Moribe, Kohei Tsuji, Masashi Sawada, Daisuke Saegusa, Hiroki Arashima, and Takako Ishikawa for continuous support.

At the end, a special thanks to my family.

Bibliography

[1] S. Kagoshima, T. Sanbongi, H. Nagasawa, and T. Takahashi, *Low-dimensional conductors* (Shokabo, 2000).

[2] D. Jérome, A. Mazaud, M. Ribault, and K. Bechgaard, J. Phys. Lettres **41**, 95 (1980).

[3] K. Oshima *et al.*, Phys. Rev. B **38**, 938 (1988).

[4] Y. Kuwata, M. Itaya, and A. Kawamoto, Phys. Rev. B **83**, 144505 (2011).

[5] K. Kanoda, Phys. C Supercond. **282-287**, 299 (1997).

[6] R. Lortz *et al.*, Phys. Rev. Lett. **99**, 1 (2007).

[7] T. Komatsu, N. Matsukawa, T. Inoue, and G. Saito, J. Phys. Soc. Jpn. **65**, 1340 (1996).

[8] M. Itaya, Y. Eto, A. Kawamoto, and H. Taniguchi, Phys. Rev. Lett. **102**, 1 (2009).

[9] J. Caulfield *et al.*, J. Phys. Condens. Matter **6**, 2911 (1994).

[10] A. Kawamoto, K. Miyagawa, Y. Nakazawa, and K. Kanoda, Phys. Rev. B **52**, 15522 (1995).

[11] Y. Shimizu, K. Miyagawa, K. Kanoda, M. Maesato, and G. Saito, Phys. Rev. Lett. **91**, 107001 (2003).

[12] R. H. McKenzie, Comments Condens. Matter Phys. **18**, 17 (1998), arXiv:9802198.

[13] S. Elsässer, D. Wu, M. Dressel, and J. A. Schlueter, Phys. Rev. B **86**, 155150 (2012).

[14] M. Abdel-Jawad *et al.*, Phys. Rev. B **82**, 125119 (2010).

[15] A. Kawamoto, Y. Honma, and K. K.-i. Kumagai, Phys. Rev. B **70**, 060510 (2004).

[16] K. Yakushi, Toyota Res. Rep. (2014).

[17] M. Pinterić *et al.*, Phys. Rev. B **90**, 195139 (2014).

[18] A. Kawamoto, Y. Honma, K. Kumagai, N. Matsunaga, and K. Nomura, Phys. Rev. B **74**, 212508 (2006).

[19] K. Byczuk, W. Hofstetter, and D. Vollhardt, Phys. Rev. Lett. **94**, 056404 (2005).

[20] M. Aguiar, V. Dobrosavljević, E. Abrahams, and G. Kotliar, Phys. Rev. Lett. **102**, 156402 (2009).

[21] H. Shinaoka and M. Imada, J. Phys. Soc. Jpn. **78**, 094708 (2009).

[22] T. Sasaki, Crystals **2**, 374 (2012).

[23] T. Furukawa *et al.*, Phys. Rev. Lett. **115**, 077001 (2015).

[24] H. Kobayashi, H. Cui, and A. Kobayashi, Chem. Rev. **104**, 5265 (2004).

[25] H. Kobayashi *et al.*, Chem. Lett. **22**, 1559 (1993).

[26] S. Imajo *et al.*, J. Phys. Soc. Jpn. **85**, 043705 (2016).

[27] W. A. Coniglio *et al.*, Phys. Rev. B **83**, 224507 (2011).

[28] S. Uji *et al.*, Phys. Rev. Lett. **97**, 157001 (2006).

[29] S. Uji *et al.*, Phys. Rev. B **85**, 174530 (2012).

[30] H. Mori *et al.*, Phys. C Supercond. **357-360**, 103 (2001).

[31] H. Tanaka, A. Kobayashi, A. Sato, H. Akutsu, and H. Kobayashi, J. Am. Chem. Soc. **121**, 760 (1999).

[32] T. Minamidate *et al.*, J. Phys. Soc. Jpn. **84**, 063704 (2015).

[33] J. Schmalian, Phys. Rev. Lett. **81**, 4232 (1998).

[34] J. Merino and R. H. McKenzie, Phys. Rev. Lett. **87**, 237002 (2001).

[35] S. Hirose and A. Kawamoto, Phys. Rev. B **80**, 165103 (2009).

[36] H. Mayaffre, P. Wzietek, D. Jérome, C. Lenoir, and P. Batail, Phys. Rev. Lett. **75**, 4122 (1995).

[37] S. M. De Soto *et al.*, Phys. Rev. B **52**, 10364 (1995).

[38] G. E. Pake, J. Chem. Phys. **16**, 327 (1948).

[39] H. H. Wang *et al.*, Chem. Mater. **2**, 482 (1990).

[40] H. Urayama *et al.*, Chem. Lett. **17**, 55 (1988).

[41] U. Geiser *et al.*, Inorg. Chem. **30**, 2586 (1991).

[42] T. Naito, H. Kobayashi, and A. Kobayashi, Bull. Chem. Soc. Jpn. **70**, 107 (1997).

[43] S. Hirose, M. Misawa, and A. Kawamoto, Crystals **2**, 1034 (2012).

[44] A. M. Kini *et al.*, Inorg. Chem. **29**, 2555 (1990).

[45] H. Urayama, H. Yamochi, G. Saito, and S. Sato, Chem. Lett. , 463 (1988).

[46] S. M. De Soto *et al.*, Phys. Rev. B **54**, 16101 (1996).

[47] Y. Shimizu, K. Miyagawa, K. Kanoda, M. Maesato, and G. Saito, Phys. Rev. B **73**, 140407 (2006).

[48] T. Kawai and A. Kawamoto, J. Phys. Soc. Jpn. **78**, 074711 (2009).

[49] A. Kawamoto, K. Miyagawa, Y. Nakazawa, and K. Kanoda, Phys. Rev. B **52**, 15522 (1995).

[50] M. E. Lines, J. Phys. Chem. Solids **31**, 101 (1970).

[51] Y. Eto and A. Kawamoto, Phys. Rev. B **81**, 020512 (2010).

[52] N. Toyota, T. Sasaki, H. Sato, and Y. Watanabe, Phys. C Supercond. **178**, 339 (1991).

[53] D. F. Smith, C. P. Slichter, J. a. Schlueter, A. M. Kini, and R. G. Daugherty, Phys. Rev. Lett. **93**, 167002 (2004).

[54] Y. Eto and A. Kawamoto, Phys. Rev. B **81**, 020512 (2010).

[55] J. A. Wright *et al.*, Phys. Rev. Lett. **107**, 087002 (2011).

[56] H. Mayaffre *et al.*, Nat. Phys. **10**, 928 (2014).

[57] H. Wang *et al.*, Synth. Met. **42**, 1983 (1991).

[58] P. Lunkenheimer *et al.*, Nat. Mater. **11**, 755 (2012).

[59] M. A. Tanatar *et al.*, Phys. Rev. B **62**, 15561 (2000).

[60] M. A. Tanatar, T. Ishiguro, S. Kagoshima, N. D. Kushch, and E. B. Yagubskii, Phys. Rev. B **65**, 064516 (2002).

[61] M. Inokuchi *et al.*, Bull. Chem. Soc. Jpn. **68**, 547 (1995).

[62] S. Nakajima *et al.*, J. Phys. Soc. Jpn. **81**, 063706 (2012).

[63] M. Takigawa, N. Motoyama, H. Eisaki, and S. Uchida, Phys. Rev. B **55**, 14129 (1997).

[64] N. Fujiwara, H. Yasuoka, Y. Fujishiro, M. Azuma, and M. Takano, Phys. Rev. Lett. **80**, 604 (1998).

[65] K. Watanabe, H. Kawamura, H. Nakano, and T. Sakai, J. Phys. Soc. Jpn. **83**, 034714 (2014), arXiv:1309.6309.

[66] Y. Saito and A. Kawamoto, Solid State Nucl. Magn. Reson. **73**, 22 (2016).

[67] H. Kobayashi *et al.*, J. Am. Chem. Soc. **118**, 368 (1996).

[68] H. Seo and H. Fukuyama, J. Phys. Soc. Jpn. **66**, 3352 (1997).

[69] T. Moriya, Prog. Theor. Phys. **16**, 23 (1956).

[70] T. Otsuka *et al.*, J. Solid State Chem. **159**, 407 (2001).

[71] S. Fukuoka *et al.*, Phys. Rev. B **93**, 245136 (2016).

[72] H. Akiba, K. Shimada, N. Tajima, K. Kajita, and Y. Nishio, Crystals **2**, 984 (2012).

[73] H. Mori *et al.*, J. Solid State Chem. **168**, 626 (2002).

[74] Y. Kurosaki, A. Furuta, H. Taniguchi, K. Miyagawa, and K. Kanoda, Phys. B Condens. Matter **404**, 3138 (2009).

[75] F. Kagawa, Y. Kurosaki, K. Miyagawa, and K. Kanoda, Phys. Rev. B **78**, 184402 (2008).